Università degli Studi di Napoli Federico II

Ph.D. Program in Industrial Products and Processes Engineering

XXXVII Cycle

THESIS FOR THE DEGREE OF DOCTOR IN PHILOSOPHY

Eco-sustainable design of hybrid redox-active materials for the removal of microplastics from water

SCUOLA POLITECNICA E DELLE SCIENZE DI BASE

DIPARTIMENTO DI INGEGNERIA CHIMICA, DEI MATERIALI E DELLA PRODUZIONE INDUSTRIALE

Supervisor:

Prof. Antonio Aronne

Ph.D. Candidate:

Paola Amato

DR996123

La borsa di dottorato è stata cofinanziata con risorse del
Programma Operativo Nazionale Ricerca e Innovazione 2014-2020, risorse FSE REACT-EU
Azione IV.4 “Dottorati e contratti di ricerca su tematiche dell’innovazione”
e Azione IV.5 “Dottorati su tematiche Green”

Abstract

Microplastics pollution has become one of the main environmental problems, and the issue of plastic wastes accumulation is a severe threat to whole ecosystem.

This study is focused on the design and synthesis of hybrid materials, constituted by a semiconducting metal oxide (ZnO or TiO_2) conjugated to a biowaste material (humic substances or rosin), that play an active role in the photodegradation of common widely used polymers, such as linear low-density polyethylene (LLDPE), polylactic acid (PLA) and polyethylene terephthalate (PET).

Hybrid ZnO- and TiO_2-humic substance nanoparticles were synthesized through solvothermal methods, and their ability in the photodegradation of LLDPE and PLA under UVA/solar illumination was explored.

The development of innovative chemical approach for the treatment of microplastics, based on an oxidative process that does not require any direct energy source (irradiation or heat) is one of the main results of this research activity. It is based on a new hybrid TiO_2-based material (T-*Abi*), that was synthesized through a simple sol-gel synthesis procedure, in which titanium is conjugated with a bio-waste, rosin, mainly constituted by abietic acid. The ligand-to-metal charge transfer complexes formed between rosin and Ti^{4+} allow the generation of reactive oxygen species without UV irradiation for its activation. In agreement with theorical calculations, superoxide radical ions are stabilized at ambient conditions on the surface of T-*Abi* allowing to obtain an impressive degradation of LLDPE after 1 month exposure in a batch configuration under indirect daylight illumination. Likewise, preliminary results concerning the chemical degradation of PET in the same conditions were also obtained.

Furthermore, the chemical surface degradation of polytetrafluoroethylene (PTFE) magnetic stir bars was revealed for the first time, due to the effect produced by the oxidative activity of T-*Abi* under indirect daylight conditions.

The innovative and sustainable approach developed in this PhD research activity represents a promising cost-effective strategy for the oxidative degradation of

microplastics, without producing any toxic by-products. The findings unlock the potential of T-*Abi* in advancing environmental remediation and promoting a circular bioeconomy.

Abstract

L'inquinamento da microplastiche è diventato uno dei principali problemi ambientali, e l'accumulo di rifiuti plastici rappresenta una minaccia grave per l'intero ecosistema.

Questo studio è incentrato sulla progettazione e sintesi di materiali ibridi, costituiti da un ossido metallico semiconduttore (ZnO o TiO_2) coniugato con un bio-scarto (sostanze umiche o colofonia), che esplicano un ruolo determinante nei processi di fotodegradazione di polimeri di uso comune, quali il polietilene lineare a bassa densità (LLDPE), l'acido polilattico (PLA) e il polietilene tereftalato (PET).

In primo luogo, sono state sintetizzate nanoparticelle ibride a base di ZnO e/o TiO_2 e sostanze umiche per via solvotermale, ed è stata esplorata la loro capacità di fotodegradare LLDPE e PLA con l'impiego della radiazione UVA/solare.

Tuttavia, lo sviluppo di un approccio chimico innovativo per il trattamento delle microplastiche, basato su un processo ossidativo che non richiede alcuna fonte di energia diretta (irraggiamento o calore), è uno dei principali risultati di questa attività di ricerca. Questo approccio si basa su un nuovo materiale ibrido a base di TiO_2 ("T-*Abi*"), sintetizzato via sol-gel, in cui il titanio è coniugato con un bio-scarto, la colofonia, costituita principalmente da acido abietico. I complessi di trasferimento di carica formati tra la resina e gli ioni Ti^{4+} portano alla generazione delle specie reattive dell'ossigeno (ROS) senza la necessità di irraggiamento UV. In accordo con gli studi computazionali DFT eseguiti, gli anioni radicali superossido sono stabilizzati sulla superficie del materiale ibrido T-*Abi* in condizioni ordinarie di illuminazione (ciclo giorno-notte) e di temperatura, consentendo così di ottenere una notevole degradazione di tipo chimico del LLDPE dopo un mese di trattamento in queste condizioni, adoperando una configurazione di tipo batch. Analogamente, sono stati ottenuti importanti risultati preliminari riguardanti la degradazione chimica del PET nelle stesse condizioni.

Inoltre, come ulteriore conferma della straordinaria attività ossidativa di cui è dotata il materiale ibrido T-*Abi*, si è dimostrato, per la prima volta, che questo materiale è in grado di degradare chimicamente la superfice delle ancorette magnetiche rivestite in

politetrafluoroetilene (PTFE), comunemente ritenuto un polimero con eccezionale stabilità chimica, in condizioni ordinarie di illuminazione e temperatura.

L'approccio innovativo ed eco-sostenibile sviluppato in questa attività di ricerca rappresenta una strategia promettente per la degradazione ossidativa delle microplastiche senza produrre sottoprodotti tossici. I risultati ottenuti fanno emergere il potenziale di T-*Abi* nel promuovere la bonifica ambientale e nel favorire un'economia bio-circolare.

Table of Contents

List of abbreviations

AFM	Atomic Force Microscopy
AOP	Advanced Oxidation Process
ATR	Attenuated Total Reflection
BET	Brunauer-Emmett-Teller
BPA	Bisphenol A
CB	Conduction Band
CI	Carbonyl Index
DDT	Dichlorodiphenyltrichloroethane
DFT	Density Functional Theory
DM	Dynamic Membrane
DMPO	5,5-Dimethyl-1-pyrroline N-oxide
DRUV	Diffuse-Reflectance UV-Visible
DSC	Differential Scanning Calorimetry
DTA	Differential Thermal Analysis
EDC	Endocrine Disrupting Compound
EDS	Energy Dispersive Spectroscopy
EG	Ethylene Glycol
EGA	Evolved Gas Analysis
EPR	Electron Paramagnetic Resonance
FTIR	Fourier-Transform Infrared
GC-MS	Gas Chromatography-Mass Spectrometry
GPC	Gel Permeation Chromatography
HA	Humic Acid
HASS	Humic Acid Sodium Salt
HDPE	High-Density Polyethylene
HER	H_2 evolution reaction
HS	Humic Substance
LDPE	Low-Density Polyethylene
LLDPE	Linear Low-Density Polyethylene

LMCT	Ligand-to-Metal Charge Transfer
MBR	Membrane Bioreactor
MF	Microfiltration
MPs	Microplastics
NMR	Nuclear Magnetic Resonance
OER	O_2 Evolution Reaction
PBDEs	Polybrominated Diphenyl Ethers
PBSA	Poly(butylene succinate-co-adipate)
PC	Polycarbonate
PCBs	Polychlorinated Biphenyls
PCL	Polycaprolactone
PE	Polyethylene
PET	Polyethylene Terephthalate
PGA	Poly(glycolic acid)
PHA	Poly(hydroxyalkanoates)
PHB	Poly(hydroxybutyrate)
PLA	Polylactic Acid
PLE	Excitation-resolved Photoluminescence
PMMA	Poly(methyl methacrylate)
PMS	Peroxymonosulfate
POPs	Persistent Organic Pollutants
PP	Polypropylene
PS	Polystyrene
PTFE	Polytetrafluoroethylene
PVC	Polyvinyl Chloride
RO	Reverse Osmosis
ROS	Reactive Oxygen Species
SEM	Scanning Electron Microscopy
SERS	Surface-Enhanced Raman scattering
TEA	Triethylamine
TEM	Transmission Electron Microscopy
TFE	Tetrafluoroethylene

TGA	Thermogravimetric Analysis
TOC	Total Organic Carbon
TPA	Terephthalic Acid
TPS	Thermoplastic Starch
UF	Ultrafiltration
VB	Valence Band
VI	Vinyl Index
WWTPs	Waste Water Treatment Plants
XPS	X-ray Photoelectron Spectroscopy
XRD	X-Ray Diffraction

1.INTRODUCTION

The environmental impact of plastic pollution, particularly microplastics, has emerged as one of the most pressing challenges of the 21st century [1]. Microplastics (MPs), defined as plastic materials smaller than 5 mm, are pervasive in ecosystems worldwide, posing serious threats to biodiversity, human health, and environmental sustainability [2]. The persistence of these materials in nature and their potential bioaccumulation in the food chain underline the urgency of developing effective methods for their degradation and removal [3].

In response to these challenges, an increasing interest is focusing on developing chemical and biological methods for the degradation of MPs [4]. Among these, photocatalysis has shown great promise as a potential solution [5]. Photocatalytic materials, such as titanium dioxide (TiO_2) and zinc oxide (ZnO), can degrade organic pollutants under the influence of light, typically UV radiation [6]. However, UV light requires high energy and specific wavelengths, which are not always available in natural environments, especially during cloudy days or at night. In contrast, visible-light responsive photocatalysts offer a more practical and energy-efficient solution, as visible light is more abundant and can be harnessed from natural sources like sunlight. This shift reduces energy demands and enhances the applicability of photocatalysis in real-world conditions.

This PhD work is addressed to design and synthesize innovative photo responsive hybrid materials for the chemical degradation of MPs by means of both the typical photocatalytic methods and a new advanced oxidation process (AOP) working in indirect daylight conditions.

Adopting a "waste-to-wealth" strategy, ZnO and TiO_2 were combined with diverse biowastes, such as humic substance and resin acid, to obtain new materials by solvothermal and sol gel routes. The aim is not only to face the problem of MPs pollution

but also to offer a suitable pathway for transforming low-value waste-derived materials into high-performance ones.

In this study, Linear Low-Density Polyethylene (LLDPE), Polyethylene Terephthalate (PET) and Polylactic Acid (PLA) were selected as target model MPs because they are widely used for a large variety of applications. LLDPE is commonly used in packaging films and plastic bags, PET is widely used in bottles, textiles, and packaging materials, and PLA is used in biodegradable packaging and medical products. PLA is a bio-based polymer deriving from renewable resources like corn starch or sugarcane, while LLDPE and PET are petroleum-based and non-biodegradable, persisting in the environment for hundreds of years [7,8].

This PhD research activity has been conducted at the Department of Chemical, Materials and Production Engineering of the University of Naples Federico II. Moreover, for specific characterizations and testing of the synthesized materials, different collaborations with other institutions, i.e. the Departments of Chemical Sciences and Agricultural Sciences at the University of Naples Federico II, the University of Cagliari (Department of Chemical and Geological Sciences), and the University of Salerno (Department of Industrial Engineering) have been activated, making this PhD project both comprehensive and impactful.

This PhD thesis is structured into five chapters, whose content is briefly described as follows. In the Chapter 2, an overview of the main polymeric materials is reported together with a review of MPs degradation techniques and the challenges faced in developing of efficient and sustainable methods. Chapter 3 illustrates the synthetic approaches and the physicochemical characterization of the hybrid materials, as well as the degradation tests of target polymers, focusing on the degradation efficiency and the consequent changes in the chemical structure and surface morphology.
Chapter 4 outlines the main findings and achievements of this PhD project. It highlights the successful synthesis of a hybrid TiO_2-based material on the basis of which an innovative chemical approach for the treatment of microplastics is proposed, based on an oxidative process that does not require any direct energy source (irradiation or heat).
Chapter 5 summarizes the experimental techniques used to characterize the synthesized hybrid materials, the polymeric samples treated and the reaction environment. It provides

an in-depth discussion of each technique, including its relevance and contribution to understanding the materials' physicochemical properties and performance in MPs degradation.

2. STATE OF THE ART

2.1 Plastics: The pillars of modern society

The word “plastic” is derived from the Ancient Greek *plastikos* and the Latin *plasticus*, meaning “fit for moulding or being capable of being moulded into various forms”. This refers to the material’s malleability or plasticity during manufacture, which allows it to be cast, pressed, or extruded into various shapes, such as pipes, bottles, boxes, cartons, and films [9].

Plastic products have become significant part of our daily life, primarily due to their relatively low cost and light weight, besides the easiness of their processability, resilience, recyclability, and versatility. They are ideal for a wide range of consumer and industrial applications, including automotive, construction, packaging, consumer goods, healthcare and renewable energy.

During the last century, the development and the acceptance of plastics have raised the comfort and standard of living. In absence of plastic products, today’s life would be unimaginable. It is not surprising, then, that the world plastics production reached about 400.3 million tons in 2022 [10].

Plastics are technical materials based on polymers (or macromolecular substances), where a polymer is a chemical compound made up of small molecules (monomers) that are arranged in simple repeating structure to form a large molecule or a chain. Hundreds and thousands of monomers are chemically bonded together by covalent bonds to form a polymer [9].

“Polymers” and “plastics”, could be considered as referring to two different worlds.

In the world of polymers, the properties of chain molecules are in the focus of attention and are the object of thorough theoretical studies.

In the world of plastics, the end-use performance of the technically used materials is mainly considered, with special attention to the behaviour in the various processing operations in which they are transformed into finished articles.
Nevertheless, these two worlds are closely related to each other. The typical behaviour of plastic materials, strongly deviating from other materials, can be understood only on the basis of the properties of the polymeric matrix of which they are composed [7].

Based on their source of origin, polymers can be classified into the following:

- **Natural polymers**: polymers that widely occur in nature or are extracted from plants or animals. They include proteins and nucleic acid that occur in human body, cellulose, natural rubber, silk, and wool. Starch is a natural polymer that is made up of hundreds of glucose molecules, similarly natural rubber is a polymer obtained from the latex of a rubber tree [9,11].
- **Semisynthetic/regenerated polymers**: polymers that are obtained by the simple chemical or physical treatment of natural polymers to improve their physical properties such as the tensile strength. Some of the common examples are vulcanized rubber, cellulose acetate, and rayon [11].
- **Synthetic polymers**: polymers that are synthesized in laboratories from low-molecular-weight compounds (monomers). Examples of such polymers are polyethylene (PE), polystyrene (PS), polyvinyl chloride (PVC), polytetrafluoroethylene (PTFE, Teflon), polyamides, such as nylon 6,6, synthetic rubber, epoxy resins, and others. They are developed by polymerization of monomers and combined with other chemicals. Depending on the type of manufacturing or production process of plastics, different specific chemicals are used as additives, like fillers, plasticizers, pigments, foaming agents, processing aids, lubricants, heat stabilizers, acid scavengers, antioxidants, UV stabilizers, flame retardants, antistatic agents. They were added in different quantities to control different functions and improve properties, such as the easiness of the processing, the increase of durability, the enhance of performance and appearance [1].

Morphology in polymers describes the way in which molecular chains are arranged in a solid structure.

The molecular chain arrangement in polymers can be crystalline (highly organized and regular) or amorphous (random arrangements) [9]. The arrangement of molecular chains within a polymer plays an important role in determining the overall properties of the product.

Crystalline materials have highly defined and repeatable arrangements of molecular chains. These materials melt in a narrow temperature range giving well defined melting temperatures. The crystallinity is a measure of the degree of order in the arrangement of the polymer chains, where the crystals represent the regular, ordered arrangements of molecules, and produce a distinctive geometric pattern within the material [12]. The degree of crystallinity has a significant influence on material properties such as hardness, density, melting point, transparency, and diffusion. There are no polymers that are 100% crystalline as there is always an appreciable amount of amorphous content in polymers morphology.

For this reason, based on the organization of their molecular structure, polymers can be classified as amorphous or semi-crystalline:

- **Amorphous polymers**: these polymers do not have a defined geometrical shape or regularity in the arrangement of molecular chains that are, generally, tangled giving a brittle and stiff network. These materials melt in a wide temperature range and soften gradually on heating above the glass transition temperature (T_g), that is the temperature at which an amorphous polymer undergoes a transition from a glassy to a rubbery state.

  Amorphous polymers are generally transparent, have low softening points, demonstrate high impact resistance, and show uniform properties in all directions. Some amorphous polymers are PVC, PS, poly(methyl methacrylate) (PMMA), and polycarbonate (PC) [9].
- **Semi-crystalline polymers**: these polymers are partially crystalline (organized in definite and regular order) and partially amorphous (disordered, random). They contain crystalline regions with a high degree of order, formed by folding and

stacking of the polymer chains, and amorphous or glass-like regions showing no long-range order, where the chains are entangled as illustrated in Figure 2.1.

On heating above T_g, semi-crystalline polymers melt in a narrow temperature range due to their ordered arrangement of the molecular structure associated with the crystalline regions giving a distinct melting transition (T_m). Properties such as hardness, strength, chemical resistance, stiffness, optical transparency, and melting point are influenced by the amount of crystalline phase in the polymer, whose amount should at least exceed 30%-35% in order to consider a polymer as semi-crystalline. Some of the common examples are PE, polypropylene (PP), Teflon and polyamide 6,6 [9].

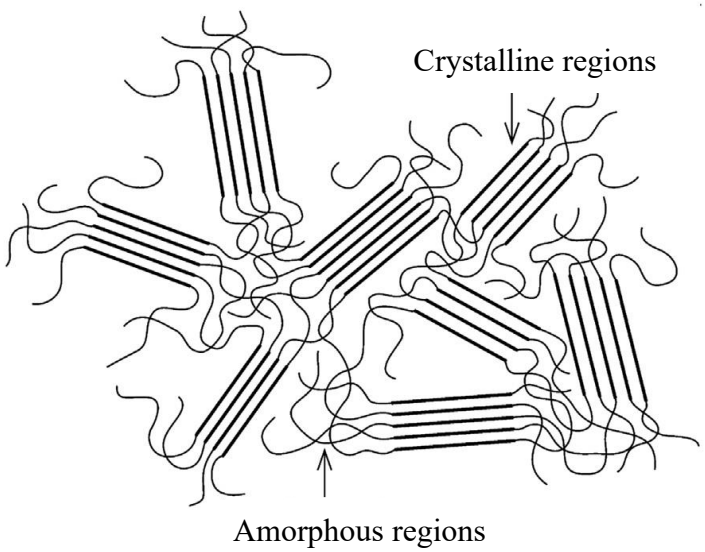

Figure 2.1. Schematic representation of crystalline and amorphous regions in semi-crystalline polymers.

Some distinctive properties of semi-crystalline\amorphous polymers are listed in Table 2.1:

Table 2.1. Characteristic properties of semi-crystalline\amorphous polymers.

Semi-crystalline polymers	**Amorphous polymers**
Distinct and sharp melting point	Soften over a wide range of temperature
Opaque or translucent	Transparent
High chemical resistance	Low chemical resistance
High tensile strength and tensile modulus	High ductility
Good fatigue resistance	Good toughness
High density	Low density
Good creep resistance	
High mould shrinkage	Low mould shrinkage

Broadly, polymers can be categorized as “fossil-based” or “bio-based”.

2.1.1 Fossil-based polymers

Fossil-based polymers (commonly thought of as traditional plastics) are polymers derived from petrochemicals. Natural gas, coal, and crude oil are the precursors for preparing synthetic polymer. Production of synthetic polymer begins in an oil refinery by distilling crude oil. In this distillation step heavy crude oil is separated into its lighter constituents, that are named segments. Naphtha is one such segment from which monomers, like ethylene, propylene, and styrene are produced and then are transformed into a polymer through polymerization reactions releasing greenhouse gases and other toxic pollutants into the environment.

The molecular weight of a polymer determines many physical properties and affects the polymer's toughness, tensile strength, impact strength, adherence, and resistance.

The tensile strength of a polymer indicates the load or stress that the material can bear before permanent deformation, and the increase in molecular weight increases the tensile and impact strength [13]. Based on the thermal properties, a polymer falls in one of the two categories as thermoplastics or thermosets [13], as discussed in the following sections and summarized in Figure 2.9.

2.1.1.1 Thermoplastics

Thermoplastic polymers are brittle and glossy in appearance and can soften when heated over the T_g, while they undergo melting when heated over the T_m. Due to these peculiar properties, products based on thermoplastic polymers can be reprocessed and reshaped by extrusion. This is mainly due to the weak intermolecular forces of attraction between the linear chains forming the polymeric network. Polyolefins are a family of thermoplastics that include PE and PP:

- **Polyethylene (PE)**

  PE is one of the most diffused commercial polymers in packaging field, due to its good mechanical properties (i.e., high strength, elongation), biochemical resistance (barrier properties against water-borne organism responsible for food spoilage), and easy processing.

Polyethylene is obtained through the addition polymerization reaction of ethylene monomer and the chemical structure of the repeating unit of PE is depicted in Figure 2.2.

It is tough, chemically inert, a bad conductor of electricity and possesses low moisture adsorption. It is used to manufacture electric wires and cables, pipes, medical devices, and automotive and space applications [9].

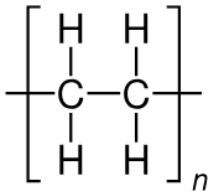

Figure 2.2. Chemical structure of the repeating unit of the polyethylene.

Depending on polyethylene density and degree of branching, it is possible to distinguish different types of PE (Figure 2.3):

a) **LDPE (Low-density polyethylene)**:
   LDPE is produced by the free-radical addition polymerization at high-pressure, typically 1000-3000 bar, and at temperatures between 80-300 °C [14]. It contains many long-chain branches along the polymer backbone, as shown in Figure 2.3a. The branched polymer does not align and pack well, resulting in low crystallinity and hence low density (0.910-0.925 g/cm^3). LDPE is ductile, flexible, tough, and transparent and it is used in preparing containers, plastic films, and plastic bags [15].
b) **HDPE (High-density polyethylene)**:
   HDPE is produced through a process known as catalytic polymerization of ethylene gas, often using either the Ziegler-Natta or metallocene catalysts. This process typically occurs at low temperatures (20-80°C) and low pressures (10-80 bar) [14]. It is characterized by linear polymer chains with few short chain branches along the polymer backbone, as displayed in Figure 2.3b. The presence of a few and short side chains allows the efficient alignment and packing of the chains of polymer backbone

forming a crystalline, high-density polymer (0.941-0.959 g/cm^3). Because of its high crystallinity, HDPE has high stiffness and hardness, high temperature resistance, and excellent chemical resistance. The melting point and the tensile strength of HDPE are higher than those of LDPE. HDPE is an opaque material ant it is used to manufacture packaging, such as milk jugs, water pipes, and detergent bottles [15].

c) **LLDPE (Linear low-density polyethylene)**:

The high capital costs of the high-pressure manufacturing method of LDPE have caused the development of a technique based on both Ziegler-Natta and inorganic catalysts to produce LLDPE, a linear polymer with a significant number of short chain branches (Figure 2.3c). LLDPE has higher tensile strength and resistance to impact than LDPE. LLDPE can have densities between 0.916 and 0.930 g/cm^3. It is used to make thin films, toys, flexible pipes, and containers [15].

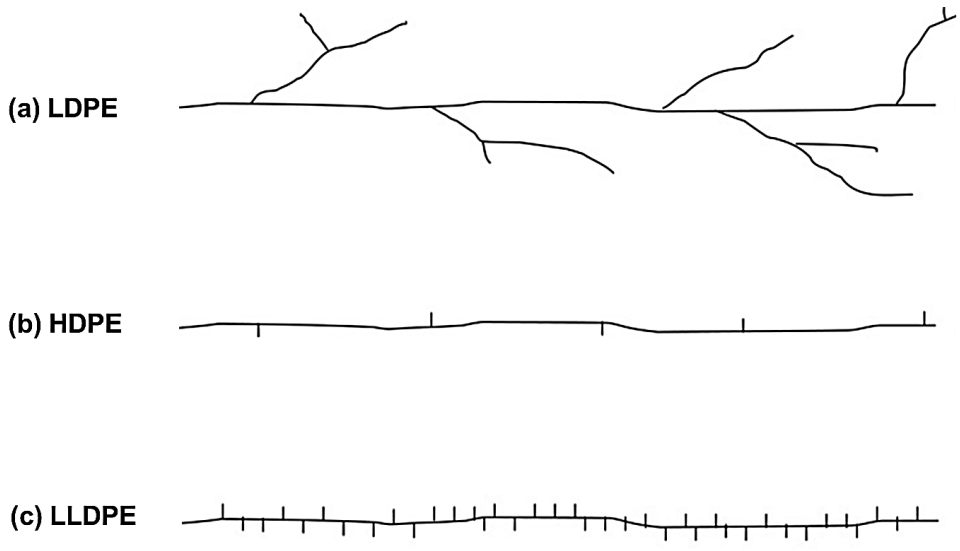

Figure 2.3. Schematic representation of the structures of several polyethylene types.

- **Polypropylene (PP)**

  PP is one of the most versatile thermoplastic polymers available commercially and it is obtained by addition polymerization of propylene gas in the presence of a Ziegler-Natta or metallocene catalyst. The chemical structure of the repeating unit of polypropylene is shown in Figure 2.4. PP possesses good mechanical properties and is highly available at a moderate cost. It is used in packaging, electronics, household appliance, battery cases, bottle tubes, filaments, and bags [13].

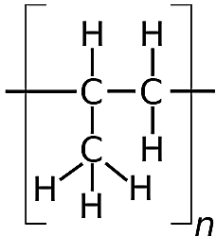

Figure 2.4. Chemical structure of the repeating unit of the polypropylene.

Other common thermoplastics are PS, PVC, and PTFE:

- **Polystyrene (PS)**

  PS is obtained by the addition polymerization of styrene monomer. The chemical structure of polystyrene is shown in Figure 2.5. It is a lightweight, brittle and stiff polymer with excellent optical properties. PS is used to produce furniture, glasses, and utensils [13].

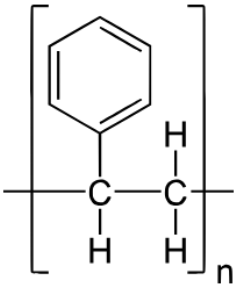

Figure 2.5. Chemical structure of the repeating unit of the polystyrene.

- **Polyvinyl Chloride (PVC)**

  PVC is obtained by the addition polymerization of vinyl chloride monomer. The chemical structure of polyvinyl chloride is shown in Figure 2.6. To enhance its properties and make it a soft, flexible and mouldable product, plasticizers can be added. PVC is used to prepare pipes and plumbing materials [13].

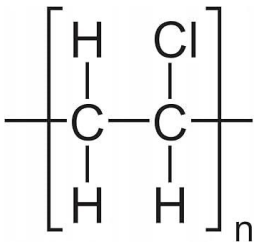

Figure 2.6. Chemical structure of the repeating unit of the polyvinyl chloride.

- **Polytetrafluoroethylene (PTFE)**

  PTFE is a fluoropolymer produced by free-radical addition polymerization mechanism of tetrafluoroethylene (TFE) monomer. The chemical structure of PTFE is represented in Figure 2.7. It has many interesting properties, for example, good chemical resistance, high thermal stability, low dielectric constant and electrical insulation. PTFE is also called Teflon and it is used to make cookware and waterproof coating [13].

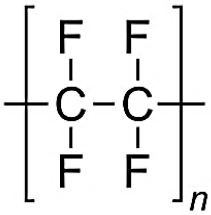

Figure 2.7. Chemical structure of the repeating unit of polytetrafluoroethylene.

.

PE, PP, PS, PVC, PTFE are addition thermoplastic polymers, while PET is a condensation thermoplastic polymer.

- **Polyethylene terephthalate (PET)**

  Polyethylene terephthalate (PET) is one of the most widely used polyesters today. It is used in packaging, fabric, engineering, electronics, and biomedical industries.

  PET is formed by polycondensation reaction of ethylene glycol (EG) and terephthalic acid (TPA) monomers, with water as a byproduct. The chemical structure of the repeating unit of PET is shown in Figure 2.8.

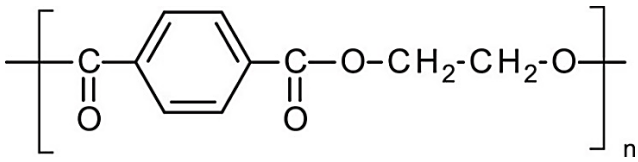

Figure 2.8. Chemical structure of the repeating unit of polytetrafluoroethylene.

2.1.1.2 Thermosets

Conversely to the thermoplastic polymers, thermosets are composed of polymer chains linked by covalent bonds forming the permanent cross-linked network. Unlike thermoplastics, thermosetting polymers cannot be remoulded or reshaped to form a new product by extrusion, as they undergo degradation over a specific temperature (decomposition temperature).

These polymers are generally robust, durable, and resistant to high temperatures. Some thermosets are phenolic (Bakelite, Novolac), polyurethanes and epoxy resins [13].

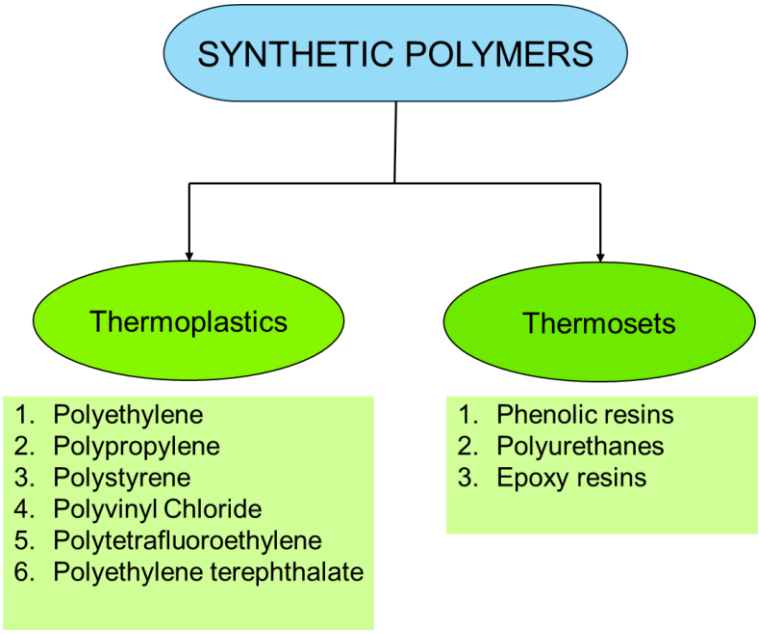

Figure 2.9. Classification of synthetic polymers based on thermal properties.

2.1.2 Bioplastics

Presently, the industrial sectors are exploring biomaterials as alternatives to petroleum-based traditional plastic materials. Biobased plastics consist of either entirely or partially natural resources such as vegetable oils and starches (plant-based products). Bioplastics have the potential to decrease environmental impacts, specifically reducing carbon footprint, and limiting greenhouse gas emissions associated with both polymer manufacturing and utilization. Therefore, the primary objective in the production of biobased plastics is to create an environmentally friendly product that show similar characteristics of those of conventional plastics [1].

Biobased plastics can be classified in biodegradable or non-biodegradable depending on their self-decomposition ability in the environment, i.e. biodegradable plastics decompose naturally, whereas non-biodegradable plastics remain unchanged for a long period of time [1]. The biodegradation is caused by biological activity, such as enzymatic action, which leads to a significant change in the plastic's chemical structure. The biodegradability is determined by estimating the actual metabolic conversion of the compostable material into carbon dioxide. This property is measured with a standard test method: EN 14046 (also published as ISO 14855: biodegradability under controlled composting conditions). According to this standard, the acceptance level is 90%, which must be reached in less than 6 months [8].

However, biodegradable bioplastics can be either bio-based or fossil-based.

According to European Bioplastics, plastic can be termed as a "bioplastic" if it is either biobased, biodegradable, or consists of both properties [8], as summarized in Figure 2.10 [16].

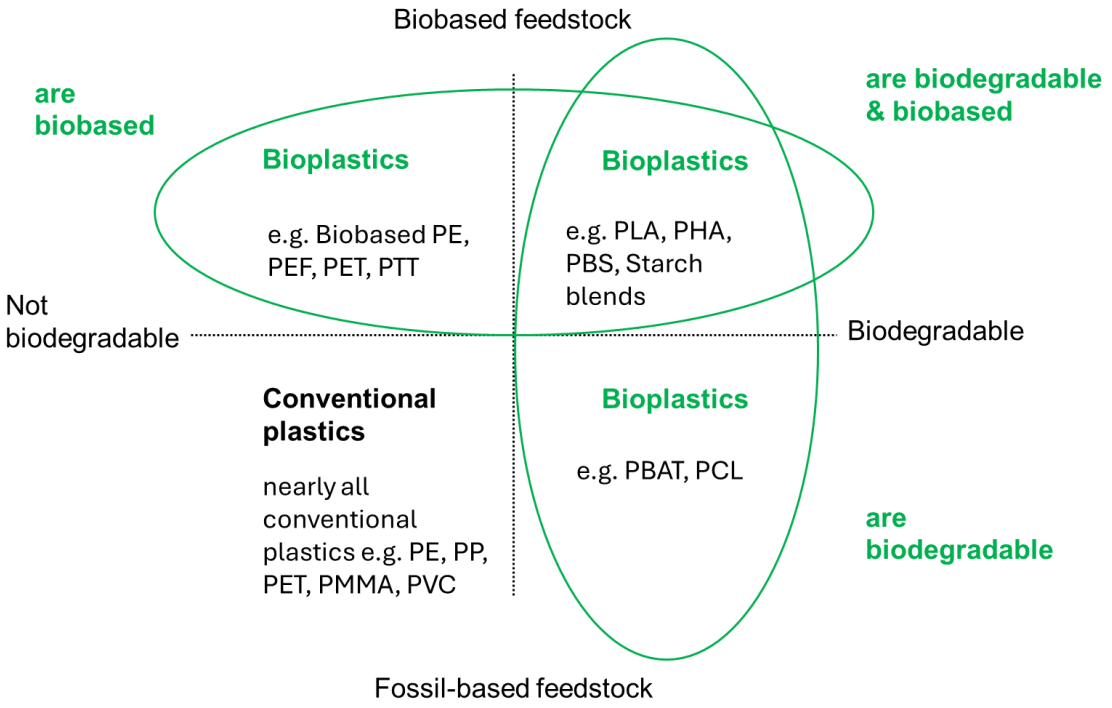

Figure 2.10. The bioplastics concept by European Bioplastics.

More specifically, biodegradable polymers may be classified into different types according to their synthesis processes and sources. They are directly obtained from biomass (proteins and polysaccharides), synthetic biopolymers from biomass (poly(lactic acid) (PLA)) or petrochemicals ((polycaprolactone) (PCL), poly(glycolic acid) (PGA), poly(butylene succinate-co-adipate) (PBSA)) or those obtained by microbial fermentation (poly(hydroxyalkanoates) (PHA), poly(hydroxybutyrate) (PHB)) [17]. The peculiarity of each polymer is detailed as follows.

- **Starch**

  Starch is one of the most abundant and renewable polysaccharides in plants. Native starch consists of amylose, a linear polymer formed by D-glucose units linked together by α-1,4 bonds, and the amylopectin, a branched polymer consisting of α-1,4 linked D-glucose units that are branched by α-1,6 bonds (see Figure 2.11).

  The brittleness and the hydrophilicity of native starch make difficult its use in the manufacturing of plastic bags and food packaging.

To enhance its flexibility and improve the easiness of either processing or plasticizing starch, various plasticizers (glycerol, glycol, sorbitol) are employed to convert the starch into thermoplastic starch (TPS) via the application of heat and shear during extrusion processes [17].

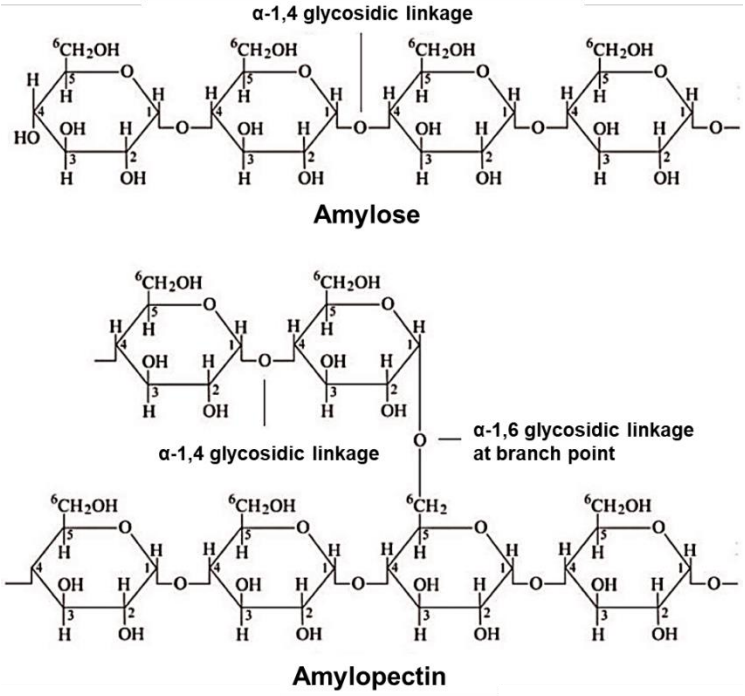

Figure 2.11. Chemical structure of amylose and amylopectin in starch.

- **Polylactic acid (PLA)**

  PLA is a biodegradable polyester obtained by lactic acid during the fermentation of renewable crops such as sugar beets and corn. Lactic acid is usually synthesized by either bacterial fermentation or petrochemicals. The PLA with low molecular weight is manufactured by the direct polycondensation of D- or L-lactic acid. On the other hand, high molecular weight PLA is produced from the ring-opening polymerization of lactide monomer from lactic acid, and it exhibits better mechanical properties. The chemical structure of PLA is displayed in Figure 2.12. PLA has been widely accepted as biodegradable polymer for packaging materials owing to its stiffness, transparency, processability and biocompatibility. However, PLA has a low resistance to oxygen permeation, and it is also brittle with less than

10% elongation at break. These properties limit its applications that require plastic deformation at higher stress levels. To address this challenge, blending PLA with highly exfoliated clay in conjunction with thermoplastic starch has proven to satisfactorily produce materials with improved mechanical strength. Moreover, when PLA was blended with PHB, there is an improved oxygen barrier, water resistant and mechanical properties of the polymer as compared with pure PLA. This demonstrated a valuable option for food packaging application [17].

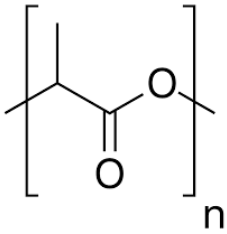

Figure 2.12. Chemical structure of the repeating unit of polylactic acid.

- **Polycaprolactone (PCL)**

  PCL is a thermoplastic biodegradable polyester with good thermal processability, low melting point and low viscosity. It is synthesized by the polymerization of ε-caprolactone. The chemical structure of PCL is shown in Figure 2.13.

  Because of the weak barrier properties and poor mechanical properties of PCL which are attributed to its low melting point, PCL application as a biodegradable polymer in the packaging industry is limited. To increase the scope of its applications, PCL is usually blended with other polymers (e.g., cellulose propionate, polylactic acid, and cellulose acetate butyrate) to improve stress crack resistance, dyeability and adhesion [17].

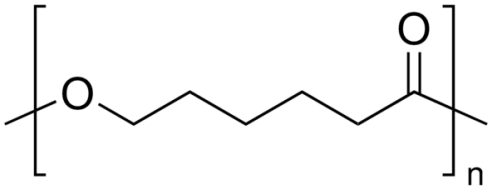

Figure 2.13. Chemical structure of the repeating unit of polycaprolactone.

- **Polyhydroxyalkanoates (PHAs)**

  Polyhydroxyalkanoates (PHAs) are a family of thermoplastic biopolyesters obtained by fermentation of a carbon substrate inside a microorganism. The PHAs production process begins by selecting specific bacteria, known as "PHAs producers". A substrate containing carbon, such as sugars (e.g. glucose, sucrose), vegetable oils or other organic compounds, is prepared to feed these PHAs-producing bacteria. These bacteria are grown in controlled environments such as bioreactors. As the bacteria grow, they use the substrate as a carbon and energy source. Once PHAs have accumulated in the bacterial cells, the bacterial culture is harvested, and the polymer is separated and sent to downstream operations. The chemical structure of PHAs is shown in Figure 2.14. Some advantageous properties of PHAs include their easy processing, insolubility in water, good resistance to UV rays, stiffness, biodegradability.

  PHAs play an important role in manufacturing everyday products such as bags, cutlery, utensils and cups [18].

  Polyhydroxybutyrate (PHB) is the most common representative of PHAs, and its chemical structure displayed in Figure 2.15. PHB is characterized by a high degree of crystallinity and a low permeability to molecules such as O_2, H_2O, and CO_2 (excellent gas barrier characteristics). PHB can be used in disposable packages, agricultural systems (for extensive release of fertilizers and agrochemicals), in medicine and medical devices and, systems of sustained drug delivery [19].

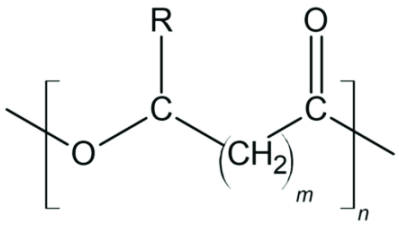

Figure 2.14. Chemical structure of the repeating unit of polyhydroxyalkanoates.

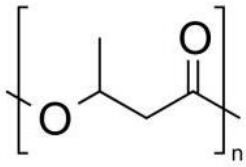

Figure 2.15. Chemical structure of the repeating unit of polyhydroxybutyrate.

2.2 What are Microplastics and why are they a problem?

The core of the present PhD project is the eco-sustainable design and synthesis of hybrid materials for the removal of microplastics from water. Let us explore what microplastics are.

The term “Microplastics (MPs)” indicates plastic materials, that can differ in size, shape, chemical composition and specific density, whose size is below 5mm [20] or specifically, ranges between 1μm and 5mm [21].
Different types of MPs, including fragments, beads, fibres, foams, pellets, and films [22–24], have been detected worldwide in marine and terrestrial ecosystems, including oceans, rivers, air, soil, drinking waters, and foods [25–29].
The average abundance of MPs in the environment changes greatly among different areas. In the European cities, the mean atmospheric MPs abundance from dry (though gravitational settling in absence of precipitation) and wet (with precipitation like rain, snow, etc) deposition has been found between 118 (Paris) and 275 (Hamburg) particles m^{-2} d^{-1} [30,31]. In the Midwest Pacific Ocean, the abundance of MPs ranged from 6028 to 95,335 pieces/km^2, with a mean concentration of 34,039 ± 25,101 pieces/km^2 [26]. Mulching soils contain on average larger amounts of MPs than non-mulching soils, with 571 pieces kg^{-1} and 263 pieces kg^{-1}, respectively [28].
It should be mentioned also that during the COVID-19 pandemic era there was a large usage and disposal of medical face masks (obtained from polymers), that produced a strong environmental pollution as these protective equipment are likely sources of MPs [2].
As expected, in recent years the production of MPs is significantly risen, with their concentrations detected on the coasts of some marine areas reaching thousands of particles per cubic meter. Without adequate measures, these numbers are expected to double in the next few years [32]. Moreover, the issue is further complicated by the lack of reliable and accurate sampling techniques, which means that the reported concentrations of microplastics in marine ecosystems may not reflect the actual amounts, leading to a potential underestimation of the problem [32].

According to their source, MPs can be divided in two main categories (Figure 2.16):

- **Primary MPs** are microplastics lying in a micro-size range contained in commercial products, such as cosmetics, detergents, paints, medications, nappies, and insecticides [32]. For example, the plastic microbeads are used as exfoliating agents in specific personal care products (body scrubs, hand cleaners, facial cleaners and toothpaste), in medical applications, in dentist tooth polish, and as carriers to deliver active pharmaceutical agents [2]. Their disposal in the environment can occur via wastewater [33].

- **Secondary MPs** are generated in the land and aquatic surroundings from the degradation (weathering, photolysis, abrasion or microbial degradation) of larger plastic materials (plastic bags, bottles and bucket) [2,32].
  The littering of plastic waste and the loss, during waste collection, from inappropriately managed landfill sites during waste collection are assumed to be the most important entry pathway of plastic materials into the environment.
  For example, the LDPE plastic mulching films, which are used in large volumes to protect agricultural crops, suppressing weeds, increasing the temperature and retaining the irrigation water in the soil, are a further relevant source of microplastics in the environment. If these thin plastic foils embrittle, the fragments can end up in the soil [33].
  Moreover, synthetic textiles are another important source of secondary microplastics, e.g. the fibres released in domestic washing machines [33].

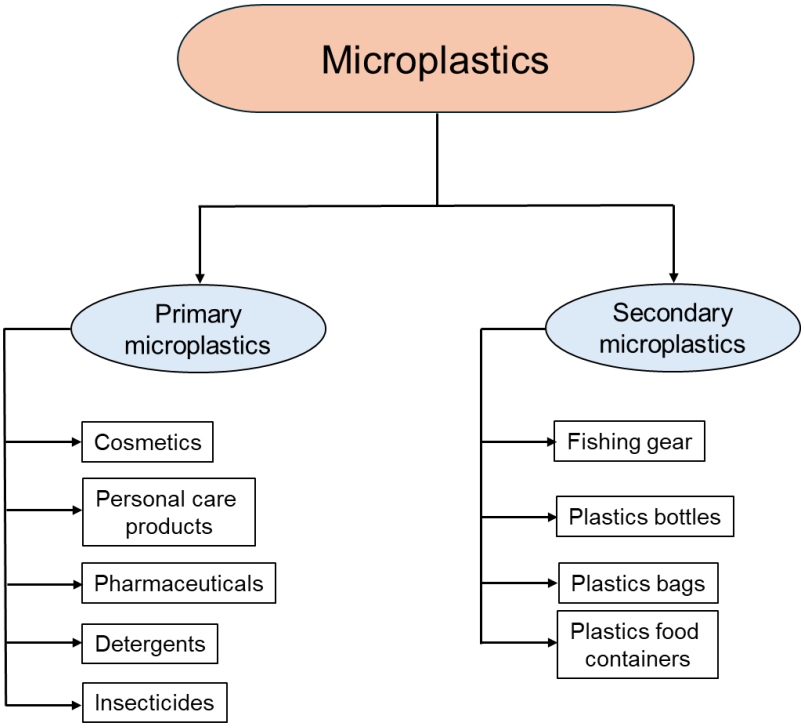

Figure 2.16. Different classifications of microplastics.

These tiny particles have a significant impact on the environment, particularly aquatic bodies, as they can accumulate and leach toxic organic and inorganic pollutants, such as persistent organic pollutants (POPs) and heavy metals. For instance, acetyl tri-n-butyl citrate is the predominant additive leaching from polyethylene MPs.

Plastics additives such as plasticizer, flame retardant, antioxidant, lubricants, anti-inflammatory agents, and UV stabilizers cause toxic effects on the environment. Bisphenol-A (BPA) used in the manufacturing of plastics is considered as an endocrine disrupting compound (EDC), exhibiting adverse effects both in humans and animals. Besides, phthalates, which are used as plasticizers for improving the flexibility of plastics, are quite dangerous since they are categorized as EDCs, leading to significant reproductive disorders [2].

Due to their hydrophobic nature, relatively large surface area/volume ratio and extraordinary vector capacity, MPs can also adsorb numerous toxic contaminants, like polychlorinated biphenyls (PCBs), polycyclic aromatic hydrocarbons (PAH), polybrominated diphenyl ethers (PBDEs), dichlorodiphenyltrichloroethane (DDT),

EDCs, various pharmaceuticals and heavy metals, further exacerbating the problem of microplastic pollution [2,32].

The chemical stability of MPs hinders their degradation allowing to persist in the environment for decades. Therefore, MPs can be considered as emerging contaminants due to their significant negative impacts on both human health and the environment.

The life cycle of MPs, which involves bioaccumulation, is shown in Figure 2.17.

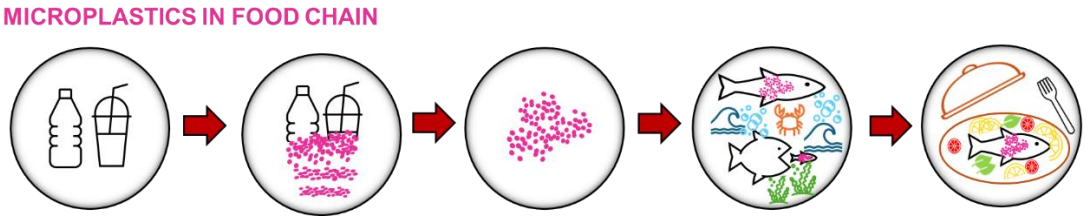

Figure 2.17. The new food chain: lifecycle of microplastics in the environment.

This cycle usually begins with the release of MPs into the ecosystems, followed by their transport into water systems. Consequently, MPs enter the food chain of aquatic organisms and undergo bioaccumulation in their tissues, following the trophic levels as zooplankton, small fish, larger fish, and other organisms that consume them. It has been shown that the swallowing of these pollutants has toxic effects on aquatic life, including fish, oysters, mussels, and sea turtles, compromising their immune and digestive systems and causing, potentially, their demise.

Moreover, MPs can directly affect the human health, as they can enter the human food chain through the consumption of contaminated fish or other aquatic organisms [32].

The MPs have been identified both in about 220 types of aquatic creatures, such as mussels, crabs, seabirds, and oysters, and in the digestive tracts of vertebrates and invertebrates: significant levels of bisphenols have been found in the liver and muscle of fish. The damages caused by the ingestion of MPs include growth problems, physical impairment, and histological variations in the intestines as well as changes in the lipid metabolism along with the behavioural fluctuations. Furthermore, endocrine disruption and neurotransmission dysfunction of marine species due to MPs has been reported due to their genotoxicity. The pollutants associated with MPs have a substantial effect on the

immune system of marine mussels, but their toxicity effects on humans have not yet been fully understood [2].

In the following the different technologies implemented to face this environmental emergency are discussed.

2.3 Current microplastics remediation technologies

2.3.1 Water Waste Treatment Plants

Due to the excessive use of plastic microbeads as additives in personal care products and the release of microfibers during laundry of synthetic textiles, municipal wastewaters contain a large amount of MPs. Before the disposal in the environment, wastewaters are treated in wastewater treatment plants (WWTPs). A typical wastewater treatment process in WWTPs comprises four stages: preliminary treatment, primary treatment, secondary treatment, and tertiary treatment (see Figure 2.18).

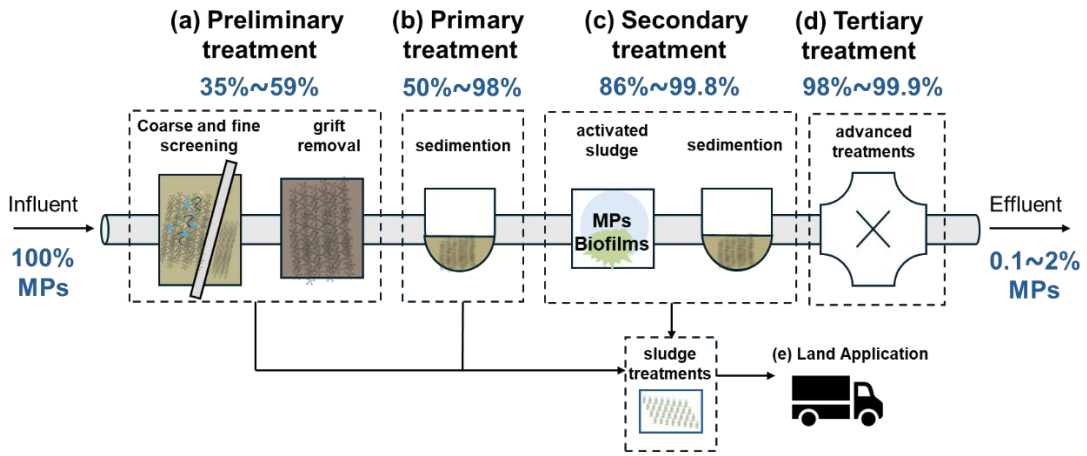

Figure 2.18. Removal of MPs at different WWTP steps: a) Preliminary treatment. b) Primary treatment. c) Secondary treatment. d) Tertiary treatment. e) Land application.

a) **Preliminary treatment**: At the first stage of the entire process (Figure 2.18a), rags, sticks, and other large items are trapped to avoid their damage to pumps and membranes in the subsequent purification processes. Typically, it consists in two steps: 1) coarse (6–150 mm) and fine (less than 6 mm) screening, and 2) grit removal, affording ~35–59% MPs removal efficiency at this stage.
b) **Primary treatment**: Subsequently, a portion of the remaining MPs are removed by gravity separation and surface skimming operations in primary clarifiers (Figure 2.18b), where the heavier MPs can settle down or trapped in sludge flocs, while the floating lighter MPs are trapped by the grease during surface skimming. As a result, about 50–98% of the MPs can normally be removed after primary treatment.
c) **Secondary treatment**: The next step of WWTPs is the secondary treatment, where the remaining suspended solids and organic pollutants dissolved in the water can be removed by the combined use of the activated sludge and the clarification tank (Figure 2.18c). The microorganisms in the activated sludge can enhance the MPs removal efficiency. Due to growth of biofilms on the surface of MPs, the relative densities of MPs are dramatically altered, which facilitates the sinking and subsequent separation of suspended MPs. It is known that there are a few bacteria, such as, *Bacillus*, *Rhodococcus*, and *Nocardia asteroides*, that are capable of degrading MPs. However, the low biodegradation rates and short contact times between activated sludge and MPs result in negligible effect on the degradation of MPs in secondary treatment. The overall MPs removal efficiency is 86–99.8% accompanied with decrease of the MPs' average size.
d) **Tertiary treatment**: The tertiary treatment, also called as "advanced treatment", is the final stage of the whole process, which is frequently adopted to produce high quality drinking water (Figure 2.18d). Typically, gravity filtration, sand filtration, disc filters, dissolved air flotation, biologically active filters, membrane bioreactors (MBRs), and other advanced treatments can be applied to decrease the concentration of suspended solid impurities, organic pollutants, heavy metals, and pathogens in water. Based on these separation techniques, it has been reported that a high MPs removal efficiency of 98–99.9% can be delivered.

Although WWTPs are regarded as reliable filters to trap pollutants existing in the municipal water, they are considered one of the main pathways of releasing MPs in natural environment and water systems. Moreover, MPs that are removed by wastewater treatment are mainly retained in the sludge, which is mostly directly landfilled or further processed as farmland fertilizer. Rational regulation of MPs in WWTPs is therefore of great importance to block MPs from further migration into the environment.

2.3.2 Physical Trapping Methods

Despite a large part of MPs is removed by WWTPs, the remaining are extremely difficult to be removed by using currently available technology. The development of more advanced techniques to reduce the amount of MPs in the effluent of WWTPs is urgent to avoid their further migration into the environment. The physical trapping methods are:

- **Coagulation**: It is one of the most frequently utilised techniques for wastewater treatment. It uses various chemical agents, such as iron-based and aluminium-based coagulants to destabilise the dissolved and suspended particles and enables their removal by sedimentation.

  It has several operational drawbacks, such as a high volume of resulting sludge that constitutes another environmental issue. This is problematic because the sludge generated from coagulation may contain more harmful substances than the original pollutants, leading to costly additional treatment and removal. The challenge of effectively treating multiple pollutants simultaneously has been identified as a major limitation of coagulation. The diversity in the composition of wastewater also contributes to the cost of the process, as various coagulants must be added, and extensive optimisation of process parameters is required to treat different types of contaminants [3,32].
- **Membrane-Based Filtration**: Due to the advantages of a high separation efficiency and compact plant size, filtration techniques such as, microfiltration (MF), ultrafiltration (UF), reverse osmosis (RO), dynamic membranes (DM), and membrane bioreactors (MBRs), have shown high efficiency to produce high quality water.

  By using the asymmetric membranes with micrometer or nanometer-sized pores, the impurities including bacteria, protozoa, viruses, and the suspended solids can be effectively removed.

  MBR is a heterogeneous reaction system composed by a biological reactor and a membrane system. First, the influent goes in the bioreactor and undergoes a biodegradation process. Here, biological-activated sludge with high biomass concentration and relative long solid retention time allows for an efficient removal of refractory organic pollutants. Subsequently, a semi-crossflow filtration system

is utilized to separate the mixed suspension, where the suspend solids are intercepted by membrane and concentrated in the so named “retentate”. With the synergy of the bio-reaction processes and porous membranes, the MBRs exhibited superior performance for treatment of MPs in contaminated wastewater [3].

- **Adsorption**: The efficacy of adsorption techniques in removing MPs from wastewater has been proved by using various adsorbents, including chitin and graphene oxide. Layered double hydroxides also exhibited significant adsorption efficiency, achieving up to 100% for microplastics and even nanoplastics. However, the non-selective characteristics of the adsorption pathway restrict the overall performance of this technique. Therefore, future research efforts should be addressed to enhance the selectivity of adsorbent materials for microplastics to achieve better removal efficiency [32].

Unfortunately, the strategies above mentioned, based mainly on simple physical separation, cannot permanently address the pollution of MPs due to the lack of treatments to eliminate or recycle the separated and collected MPs debris and particles. This evidence has led to the development of effective techniques to degrade and permanently remove MPs.

2.3.3 Microplastics degradation approaches

2.3.3.1 Biodegradation of microplastics

The degradation of MPs using microorganisms (bacteria, fungi) is named biodegradation [34]. In general, biodegradation of plastics occurs in four stages (schematized in Figure 2.19):

1. Biodeterioration: microorganisms adhere to the plastic surface by secreting extracellular polysaccharides to form a biofilm, which reduces the hydrophobicity of the plastic surface, and penetrates the plastic matrix. The formation of biofilms can cause the formation of holes and cracks in the plastic waste, weakening the physical properties of the plastic polymer (physical biodeterioration).

2. Biofragmentation: microorganisms colonize the surface of the plastic polymer and release extracellular enzymes (oxygenases, lipases, esterases, depolymerases, etc.) which alter the polymer structure, and then break down the plastic polymer into simpler and smaller parts. Therefore, the process of biofragmentation diminishes the molecular weight of the plastic, releasing oligomers and monomers.
3. Assimilation: monomers are absorbed into the cells of plastic-degrading microorganisms. Some monomers are recognized by transporters in the microbial cell membrane and thus actively enter the cell, where they are oxidized to produce energy through the microbial catabolic pathways. Eventually, the components that cannot be assimilated by microbial cell are released.
4. Mineralization: the monomers are fully oxidized and eventually mineralized into carbon dioxide, methane and water, which diffuse out of the cell.

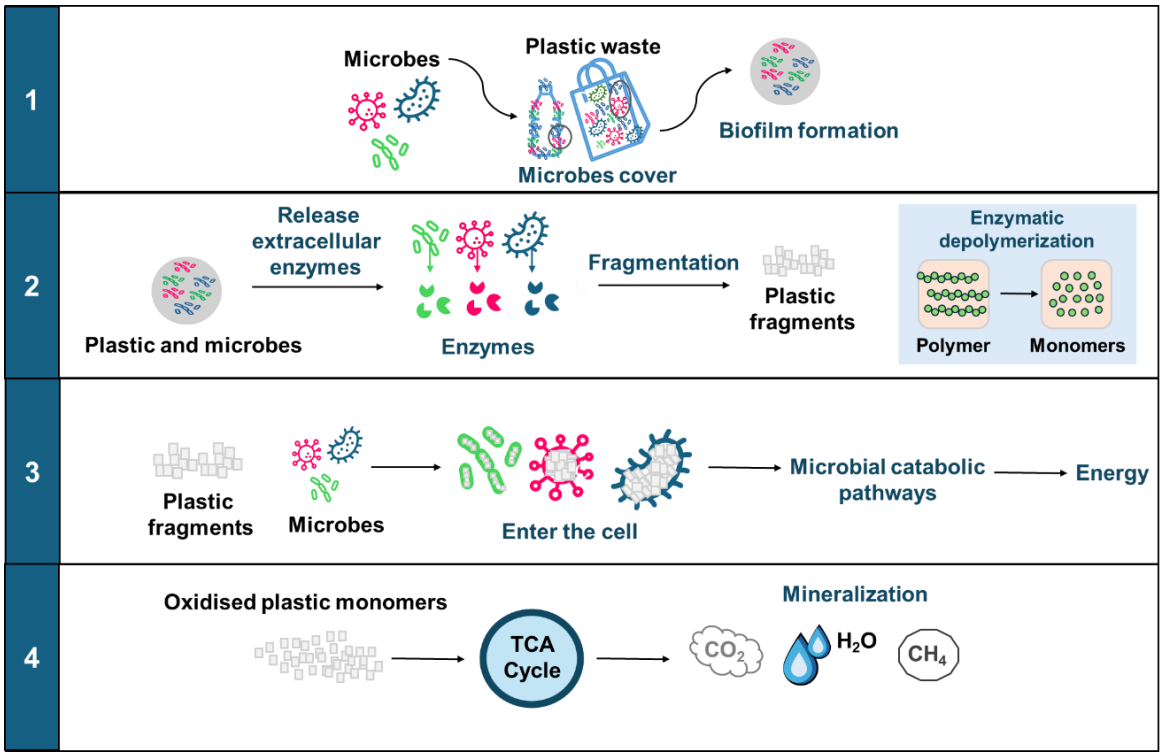

Figure 2.19. The mechanism of plastic biodegradation.

Due to its eco-friendliness, environmental affordability and minimal energy consumption, the biodegradation of MPs has gained wide acceptance [35].

Some studies have shown that certain bacteria and fungi like *Pseudomonas*, *Rhodococcus*, *Cephalosporium*, and *Mucormyces* can biodegrade PS, while species of *Aspergillus*, *Mucor*, and *Fusarium* fungi have been verified to degrade PE [34].

Currently, there are still significant challenges in plastic biodegradation, such as lack of high-performance degrading bacteria/enzymes, unclear mechanism of action, low yield of large-scale preparation of bacteria/enzymes, and insufficient bacteria/enzyme synergy. Therefore, strategies for enhancing the biodegradation process should be the focus of future research on plastic biodegradation [4].

2.3.3.2 Advanced oxidation processes (AOP)

Advanced oxidation processes (AOPs) include various chemical strategies in which organic pollutants are oxidated by means of species possessing high standard reduction potentials, such as Reactive Oxygen Species (ROS), which can non-selectively break the chemical bonds allowing to degrade and even mineralize pollutants [36–39].

ROS define a class of highly reactive oxygen-bearing molecules. They include the species formed upon incomplete reduction of molecular oxygen, namely superoxide radical anion ($O_2^{\bullet-}$), hydrogen peroxide (H_2O_2), hydroperoxyl radical ($HO_2^{\bullet}$) and hydroxyl radical ($OH^{\bullet}$), also known as reactive oxygen intermediates (ROI), ozone (O_3) and singlet oxygen ($^1O_2$). In addition to these fundamental species, peroxyl (ROO•), alkoxyl (RO•), carbonate ($CO_3^{\bullet-}$) radicals and organic hydroperoxides are encountered in the definition of ROS, and sometimes hypochlorous (HOCl), hypobromous (HOBr) and hypoiodous acids (HOI) are also mentioned [40].

Ground-state molecular oxygen is a paramagnetic biradical with two electrons occupying separate π* orbitals with parallel spins (triplet configuration, Figure 2.20). This causes a spin restriction for the reaction of O_2 with most organic molecules, which are diamagnetic, with electrons pairs with opposite spins, due to the unfavourable interaction of these pairs with the π* orbitals. Hence O_2 preferably accepts one electron at a time during redox reactions. It can react fast by single-electron transfer with radicals or other species bearing unpaired electrons, such as transition metals in some oxidation states. The

one-electron reduction of O_2 results in the formation of the superoxide radical anion. Subsequent redox conversions produce other ROS, as illustrated in Figure 2.21.

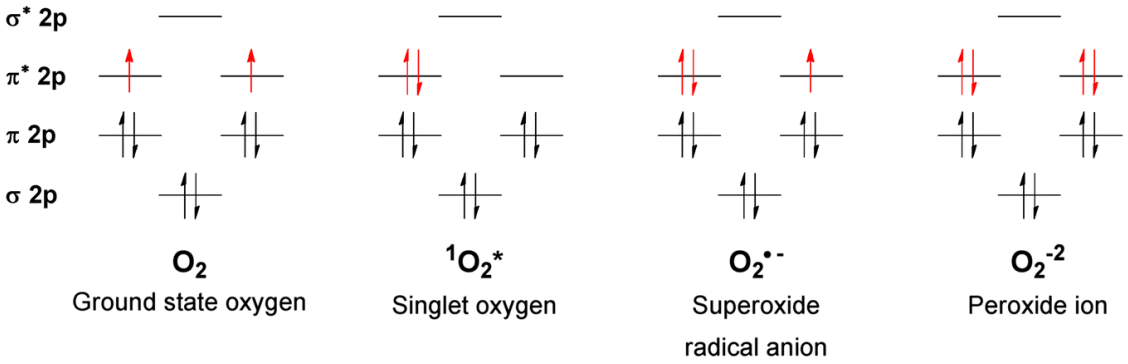

Figure 2.20. Molecular orbital diagrams for ground-state molecular oxygen and some ROS: singlet oxygen, superoxide anion and peroxide ion (deprotonated form of hydrogen peroxide) [40].

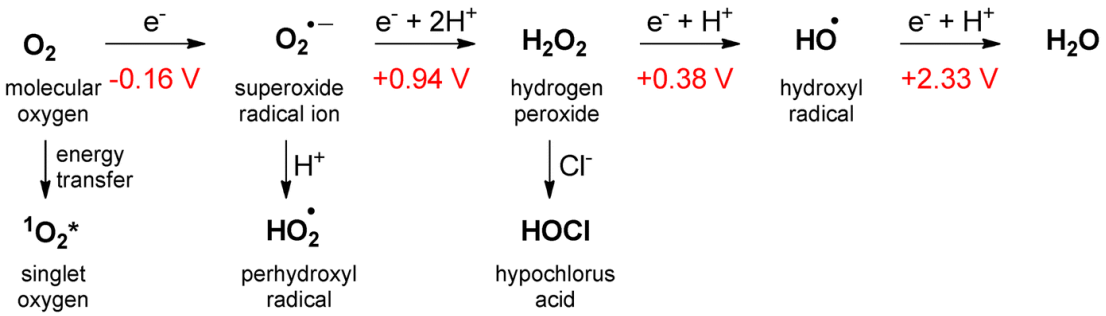

Figure 2.21. Formation of ROS through energy and electron transfer reactions. Standard redox potentials are reported (standard concentration of oxygen regarded as 1 M), adapted from reference [40].

The different kinds of AOPs and the main ROS involved in each AOPs are given in Figure 2.22 [38].

Figure 2.22. Classifications of AOP-based technologies and the ROS involved.

The most widely investigated AOPs occur both in the absence of light (Fenton and Fenton-like) and in the presence of light (photo-Fenton, photo-Fenton-like, UV/H_2O_2, O_3/UV, and the heterogeneous photocatalysis). Due to their strong oxidation capability, a large variety of pollutants including dyes, antibiotics, and persistent organic pollutants **(**POPs) have been effectively removed by these strategies [36,41–49]. MPs are obviously more challenging to be degraded due to their considerably higher molecular weights (MWs) compared to other low MW organic pollutants above mentioned.

Among AOPs, **Fenton oxidation** is an attractive treatment because of its low cost, the lack of toxicity of the reagents (i.e., Fe^{2+} ions and H_2O_2), the reactions occur at room temperature and atmospheric pressure, the absence of mass transfer limitation due to its

homogeneous catalytic nature and the simplicity of the technology. In addition, Fenton process has the shortest reaction time compared to other AOPs and can be implemented and integrated into existing water and wastewater treatments, such as coagulation, filtration, and biological oxidation [50–52]. However, Fenton oxidation has some disadvantages, including the required low pH of the reaction mixture. The optimum pH is ~2.8–3.0 where both Fe^{3+} and Fe^{2+} exist in solution.

A multitude of studies have been published concerning specific mechanisms within a Fenton reaction, with debate ongoing. The generally agreed upon mechanism of reactions is described by the Equations 2.1-2.2, in which Fe^{2+} and Fe^{3+} both react with peroxide, cycling to produce radicals, which promote organic degradation. Fe^{2+} acts as the primary catalyst, with regeneration of Fe^{3+} by peroxide. However, regeneration of Fe^{2+} from Fe^{3+} is very slow compared to the main Fe^{2+} reaction, by at least three orders of magnitude [51].

$$Fe^{2+} + H_2O_2 \rightarrow Fe^{3+} + OH^- + OH^{\bullet} \quad (2.1)$$

$$Fe^{3+} + H_2O_2 \rightarrow Fe^{2+} + HO_2^{\bullet} + H^+ \quad (2.2)$$

Recently, Fenton oxidation was employed as an accelerated ageing method for two of the most widespread MPs in watercourses: PS and PE. Subtle modifications in MPs were reported during this treatment, such as small weight losses and reduction of mean particle size [53].

The oxidative degradation of nylon 6 and PS MPs treated with peroxymonosulfate (PMS) and Fenton reagents was also investigated. Surface-enhanced Raman scattering (SERS) and gas chromatography-mass spectrometry (GC-MS) revealed some degradation products like alkanes, alcohols, aldehydes, carboxylic acid [54].

Important changes of five types of MPs (PET, PE, PVC, PP and PS) along intensified Fenton treatment were demonstrated [55]. The oxidation process starts on the particle surface, leading to its physical/morphological modification (wrinkles, voids, and holes) and chemical modifications giving the formation of oxygen functional groups, which consequently increase the hydrophilicity and acidity of the surface. Furthermore, MPs progressively reduced their size, which ultimately resulted in their complete oxidation to CO_2 [55].

The oxidation during Fenton process can be improved by applying UV or solar light irradiation, giving the "**photo-Fenton**". The resulting photo-Fenton process is the classical example of homogeneous photocatalysis.
A bio-photo-Fenton approach using glucose oxidase immobilized on titanium dioxide was also employed to degrade sulfonated polyethylene into small carboxylic acids [56].

2.3.3.3 Photocatalytic degradation of microplastics

Photocatalysis has been recognised by the international academic community as an efficient and safe environmental purification technology for the treatment of organic pollutants, including microplastics, in wastewater.
The photocatalytic degradation of microplastics involves multiple reactions. When exposed to ultraviolet or solar irradiation, MPs undergo a photo-ageing process. The polymer macromolecules can directly absorb photons and generate excited states, leading to chain scission, branching cross-linking and oxidation reactions. However, in the presence of a photocatalyst the degradation process of MPs is significantly accelerated [57].
A typical photocatalyst is a semiconductor, a material in which the valence band (VB), and the conduction band (CB), are separated by a limited gap of forbidden energy (bandgap, E_g).
In the presence of photocatalysts, the degradation of MPs can be attributed to the following steps: (i) energy harvesting from light to produce electron-hole pairs, (ii) charge migration from the bulk to the surface of the photocatalysts, and (iii) trigger for redox reactions with the actuation of charges at the interface between reactants and photocatalysts [58].
This kind of photocatalytic mechanism occurs in an oxygen-rich atmosphere, which is called the O_2 evolution reaction (OER).

Considering in detail the above steps the whole mechanism can be schematized as following reported.

1. When light of higher energy than the bandgap ($h\nu > E_g$) is absorbed by the semiconductor, electrons are excited from VB to CB, and subsequently holes are formed on the valence band, resulting in the formation of electron/hole pairs (charge separation):

$$\boldsymbol{Photocatalyst} + \boldsymbol{h\nu} \rightarrow \boldsymbol{h^{+}_{(VB)}} + \boldsymbol{e^{-}_{(CB)}} \tag{2.3}$$

2. When oxygen and the $\boldsymbol{e^{-}_{(CB)}}$ interact, a superoxide anion radical is created in the conduction band:

$$\boldsymbol{O_2} + \boldsymbol{e^{-}_{(CB)}} \rightarrow \boldsymbol{O_2^{\bullet -}} \tag{2.4}$$

3. Simultaneously, the photogenerated holes in the valence band migrate to the surface and react with H_2O to form hydroxyl radicals, $OH^{\bullet}$:

$$\boldsymbol{h^{+}_{(VB)}} + \boldsymbol{H_2O} \rightarrow \boldsymbol{OH^{\bullet}} + \boldsymbol{H^{+}} \tag{2.5}$$

4. Superoxide radicals, $O_2^{\bullet -}$, and hydroxyl radicals, $OH^{\bullet}$ are among the most active photocatalytic oxidants, which can efficiently oxidize organic compounds:

$$\boldsymbol{Organic\ (R)} + \boldsymbol{OH^{\bullet}} + \boldsymbol{O_2^{\bullet -}} \rightarrow \boldsymbol{CO_2} + \boldsymbol{H_2O} + \boldsymbol{other\ products} \tag{2.6}$$

The $O_2^{\bullet -}$ and $OH^{\bullet}$ radicals play important roles in the photocatalytic degradation of microplastics. They initiate the degradation of microplastics by attacking the adjacent polymer chains. The degradation process is spatially extended into the polymer matrix by ROS diffusion [58–60].

The basic principles of the photocatalytic degradation of MPs are shown in Figure 2.23.

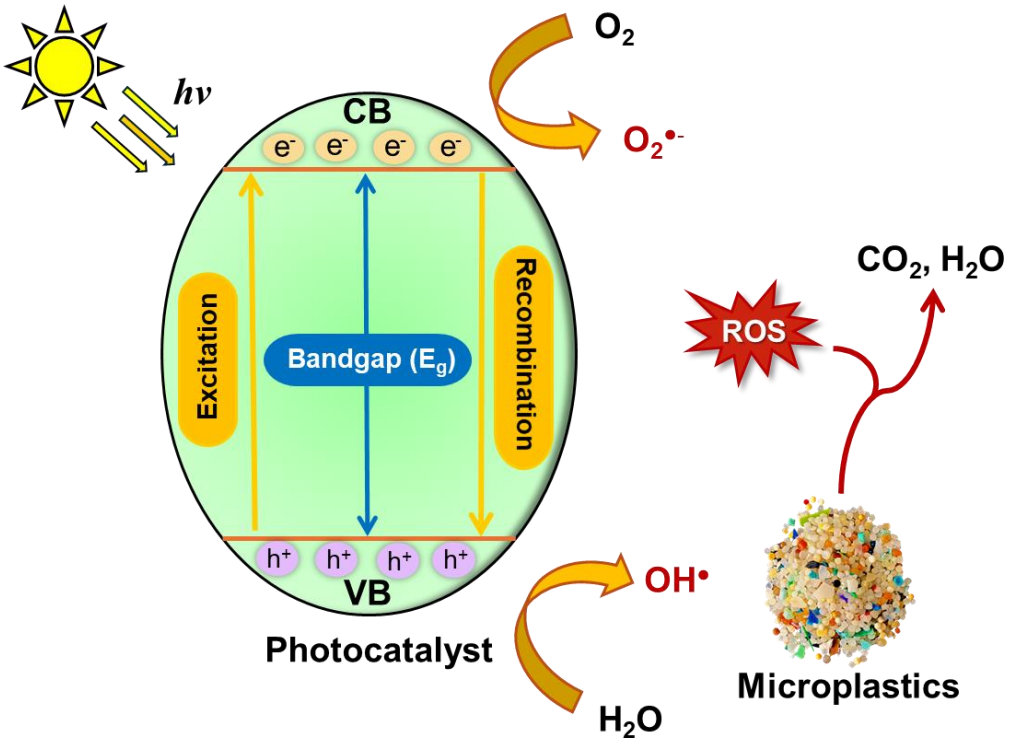

Figure 2.23. Schematic picture for MPs photocatalytic degradation mechanism.

The bandgap of semiconductor, determining the minimum energy required for the formation of the electron/hole pair, greatly affects the photocatalytic process. Recently, numerous studies have been conducted regarding the photocatalytic degradation of different types of MPs under the irradiation of light with different wavelengths. Several representative semiconductor with different photocatalytic performances have been prepared [61–63], among them TiO_2 and ZnO are commonly used.

Titanium dioxide (TiO_2) is recognized as a highly efficient photocatalyst in view of several beneficial properties including high reactivity, good photostability, non-toxicity, and moderate cost.

TiO_2 plays an effective role in photocatalytic degradation reactions of different pollutants, such as persistent contaminants, azo dyes, and emerging contaminants, like MPs [64]. However, TiO_2 has a wide bandgap (3.2 eV for anatase and 3.0 eV for rutile) allowing to absorb ultraviolet (UV) light that accounts only for less than 5% of solar light radiation. Therefore, a great deal of interest has been devoted to extending the optical response of

titanium oxide in the visible region. An effective approach to tackle this challenge is to dope TiO_2 with nonmetal elements, such as C, N, S, and I [65].

Recently, concerning MPs, carbon and nitrogen-doped titanium dioxide (C, N-TiO_2) photocatalyst was employed for the photocatalytic degradation of HDPE extracted from a commercial facial scrub. During the process, the effect of the process parameters, such as pH and temperature, were also studied. The photocatalytic tests were performed in a closed reaction chamber equipped with a 50 W LED lamp with emission in the visible spectrum (400 nm – 800 nm) for 50 h. Through the evaluation of weight loss, carbonyl index (CI) and microscope observations, it was concluded that the highest MPs degradation was achieved at pH = 3 (acidic condition) and 0 °C [6].

Nabi *et al.* investigated the photocatalytic degradation of PS microspheres over different TiO_2 nanoparticle films under UV light irradiation, achieving complete mineralization (98.40%) in 12 h [66].

Zinc oxide (ZnO) has been also widely studied because of its excellent properties, including low cost, high redox potential, nontoxicity, and environmentally friendly features. Although ZnO yields a wide bandgap (3.37 eV) and a high exciton binding energy (60 meV), this compound exhibits a greater photocatalytic performance than TiO_2 in the photodegradation of organic pollutants because the electron mobility (200-300 cm^2 V^{-1} s^{-1}) of ZnO is much higher than that of TiO_2 (0.1-4.0 cm^2 V^{-1} s^{-1}), determining high quantum efficiency. Likewise TiO_2, ZnO has been modified to extend its visible-light response by applying various methods, such as doping metals/nonmetals, depositing noble metals, constructing heterojunctions, and coupling carbon materials [67].

Concerning MPs, the photocatalytic degradation of LDPE film was carried out for 175 h in a petri dish containing the ZnO nanorods and deionized water with a 50 W dichroic halogen lamp for visible light illumination. The photocatalytic degradation of LDPE films was estimated evaluating the change of carbonyl (CI) and vinyl (VI) indexes, that was of about 30% [68].

Then Uheida *et al.*, studied the photocatalytic degradation of PP MPs suspended in water by visible light irradiation of ZnO nanorods immobilized onto glass fibers substrates [69]. After two weeks a reduction of 65% of the average particle volume of PP MPs was found.

Photodegradation by-products were identified using GC-MS and, mostly, nontoxic molecules were found[69].

During photocatalytic degradation, photogenerated ROS can cause both physical and chemical transformations of MPs.
Some key parameters used for evaluating MPs photocatalytic degradation efficiency are listed below [60].

- **Mass change**
  The photocatalytic degradation may produce a progressive reduction of MPs mass due to their decomposition. Using a microelectronic balance, it is possible to quantify this mass change evaluating the degradation efficiency as described in Equation (2.7):

$$Mass\ loss\ (\%) = \frac{M_0 - M}{M_0} * 100 \tag{2.7}$$

  Where M_0 denotes the starting mass of MPs, and M denotes their final mass at time "t" after photodegradation.
- **Particle size and surface characteristics**
  During photocatalytic degradation, MPs can undergo size reduction and develop a rougher surface texture. Several microscopic techniques, including scanning electron microscopy (SEM), transmission electron microscopy (TEM), and atomic force microscopy (AFM), are used to examine the morphology, particle size, and surface roughness of MPs collected from the reaction. The variation in the surface elemental composition of MPs can be determined by combining SEM or TEM with additional techniques like energy dispersive spectroscopy (EDS) analysis.
- **Chemical structure**
  Photocatalytic degradation can lead to changes in the crystallinity, molecular mass, and chemical composition of MPs, that can be confirmed by Fourier transform infrared spectroscopy (FTIR), Raman spectroscopy, gel permeation chromatography (GPC), and nuclear magnetic resonance spectroscopy (NMR). GPC enables the measurement of fluctuations in molecular weight during

degradation, while NMR can provide insights into molecular structures by detecting the chemical shifts of suitable probes, such as ^{1}H and ^{13}C.

FTIR is largely used to track the development of oxygen-containing functional groups on the surface of oxidized MPs, such as carbonyl and ester. In MPs research, diverse indices assess their chemical attributes and potential environmental consequences, i.e. Carbonyl Index (CI) and Vinyl Index (VI). CI and VI give a semi-quantitative estimation of the photo-oxidation degree and are determined as ratio between the absorbance of carbonyl (1710 cm^{-1}) and vinyl (880 cm^{-1}) groups, respectively, to the absorbance of a stable reference peak.

- **Crystallinity**

  During the degradation of MPs, chain scissions can occur, preferably, in the amorphous state, leading to secondary crystallization. The crystallinity of MPs can be evaluated using three fundamental techniques: X-Ray Diffraction (XRD), differential scanning calorimetry (DSC), and FTIR. XRD is commonly employed to assess the degree of crystallinity in MPs.

- **Surface composition and middle stages of formation**

  Specific technologies can monitor the evolution of MP degradation by observing changes in surface composition and the formation of intermediates. The measurement of total organic carbon (TOC) can provide an estimation of the overall amount of organic material generated during the degradation of MPs. Gas chromatography mass spectrometry (GC-MS) can be employed to identify degradation products, such as CO_2, which serves as an indicator of the effectiveness of mineralization [60].

The photocatalytic degradation can be also connected with the formation of useful chemical substances, and it is called photoreforming [70]. This photocatalytic reaction is carried out in inert atmosphere, usually in N_2 or Ar, and it is also referred to as the H_2 evolution reaction (HER).

In this case, microplastic wastes act as hydrocarbon resources, favouring the production of value-added products and H_2 [71].

Different from photodegradation with O_2, the photoinduced electrons react with protons to form H_2 (Equation (2.8)) and the holes photogenerated drive the transformation of MPs to produce relatively highly selective value-added chemicals (Equation (2.9)).

$$2H^+ + 2e^-_{(CB)} \rightarrow H_2 \quad (2.8)$$

$$h^+_{(VB)} \text{ or } OH^{\bullet} + MPs \rightarrow Selective\ valuable\ organic\ products \quad (2.9)$$

The overall photocatalytic reaction process of microplastics of the two different strategies is illustrated in Figure 2.24.

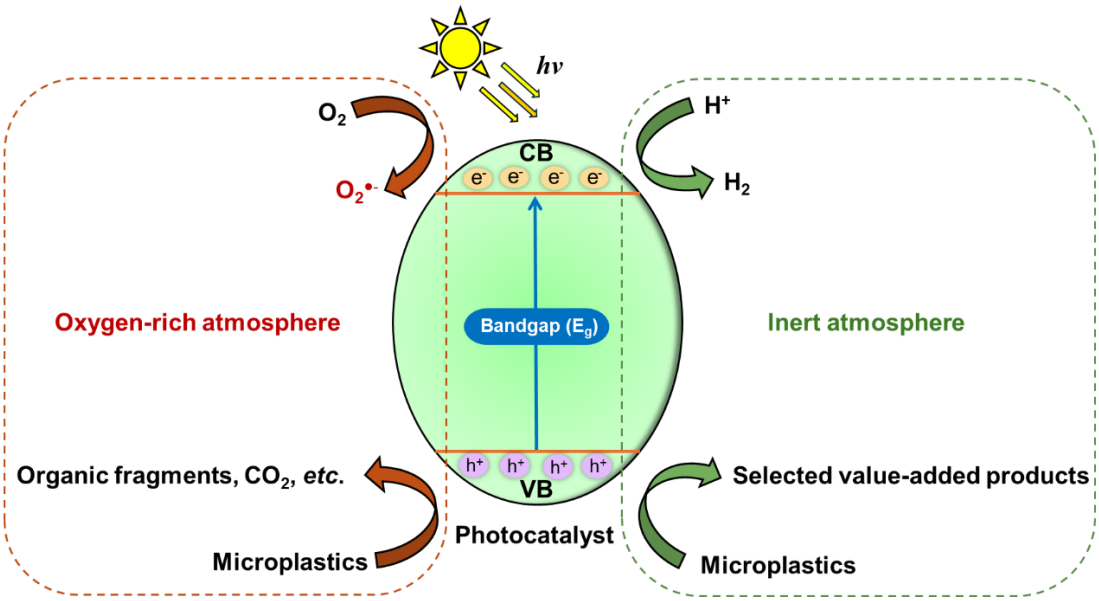

Figure 2.24. Schematic diagram of photocatalytic reactions of MPs in different environments.

However, the long periods of irradiation, whether under visible or UV light, required to produce measurable physical and/or chemical changes in MPs and the generation of toxic intermediate degradation byproducts are the main drawbacks of photocatalysis [72].
To date, there is no well-developed single technology for MPs degradation; therefore, the possibility of using combined technologies for MPs removal should be considered.

2.4 Recycling protocols of plastic wastes to eliminate microplastics

The development of rational strategies for plastics recycling is meaningful to avoid the mismanaged plastic wastes releasing secondary MPs into nature environment. Recycling not only reduces the increasing volume of plastic wastes, but also provides secondary raw materials for the generation of new value-added products. In addition, it allows to preserve raw petrochemical products. The recycling of waste plastics generally can be categorized into three main methods, namely primary, secondary (mechanical), and tertiary (chemical), as illustrated in Figure 2.25 [73].

- **Primary recycling** can be defined as second-hand use, as the wastes are directly reused without any reprocessing [74]. This method, known as "closed-loop recycling", requires clean and high-quality waste materials, such as process scraps or post-consumer items with a known origin. An example of primary recycling is the production of plastic bottles made from a mixture of recycled PET and virgin PET [75].
- **Secondary recycling** (mechanical recycling) transforms the material into a secondary raw material for the manufacturing of new products. This recycling methodology usually involves several steps, namely separation/sorting, washing, grinding, and reprocessing [74].
- **Tertiary recycling** (chemical recycling) converts polymers back to their building blocks (oligomers or even individual monomers) by thermal or solvent-assisted depolymerization. The tertiary recycling can also involve advanced thermochemical recycling processes namely pyrolysis, or energy recovery from waste through thermal process [74,76].

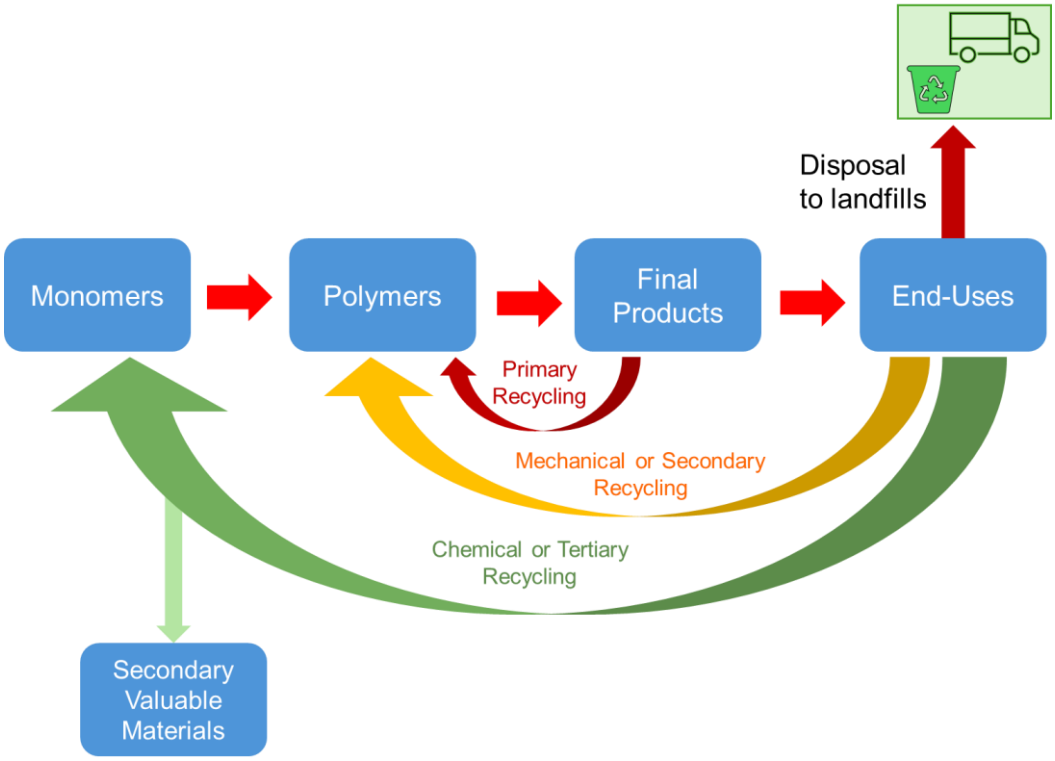

Figure 2.25. Polymer recycling approaches.

3. RESULTS AND DISCUSSION

The core of this PhD research activity is the design and the synthesis of hybrid materials, by a waste-to-wealth approach, for the degradation of polymeric samples chosen as models of microplastics.

This PhD thesis work consists of two main parts:

- First, Humic Acids-doped Zinc Oxide (HAs-doped/ZnO), Humic Substance/Zinc Oxide (HS/ZnO) and Humic substance/Titanium oxide (HS/TiO_2) hybrid nanoparticles were synthesized through solvothermal route for the photocatalytic degradation of LLDPE and PLA under UVA/solar radiation.
- Then, through sol-gel synthesis, a new hybrid material formed by titanium oxide and a bio-waste, rosin, mainly constituted by abietic acid, was obtained. The synthesized TiO_2-Abietic acid material, named T-*Abi*, was able to promote the oxidative degradation of LLDPE and PET at room temperature and under indirect daylight conditions. Here, for the first time, an innovative chemical approach for the treatment of MPs, based on an oxidative process that does not require any direct energy source (irradiation or heat), is proposed.

In the following, for each approach, the synthesis procedure adopted, and the experimental set-up of the degradation test will be described.

3.1 Photocatalytic degradation of LLDPE and PLA under UVA/solar radiation

Photocatalysis, based on the action of Reactive Oxygen Species (ROS) generated by semiconductor materials, can be viewed as a potential eco-friendly, low-cost and efficient strategy for the treatment of organic pollutants, such as plastics and MPs.
The synthesis strategy to produce hybrid organo-inorganic nanoparticles with an advanced ability in generating ROS, whereby a metal oxide semiconductor is combined at a molecular scale with bioderived organic components. Among them, humic substances (HS) are the alkali-soluble fraction of natural organic matter, usually found in water, soil and sediments [77–79]. They are rich in functional groups (quinones, phenols, carboxyl and hydroxylic species) conferring them many functional properties, including metal ions chelation, organic pollutants absorption and, above all, regenerable redox behavior in terms of ROS generation and/or scavenging.

Here, the eco-inspired design of hybrid ZnO- and TiO_2-based nanoparticles as efficient photocatalysts for the photodegradation of LLDPE and PLA slices and MPs, under UVA and solar irradiation [80,81], is described.

3.1.1 Solvothermal synthesis

Solvothermal synthesis is a versatile technique for tailoring the morphology and properties of nanostructured materials. It is typically performed in sealed containers, where the temperature can exceed the boiling point of the solvents (water or organic liquids) by the increase of the autogenous pressures. The increase of temperature and pressure promotes the solubility and the reactivity of the reagents, leading to the formation of nanostructures with controlled size, shape, and composition by tuning the key steps of the whole process: nucleation and crystal growth.
During nucleation, tiny particles or "nuclei" are formed, that in the subsequent stage grow forming larger nanostructures. The equilibrium reactions, kinetics, and products could be significantly affected by interactions between solvents and reactants, intermediates, and

products, as well as, by the change of solvent properties with the temperature, such as, viscosity and dielectric constant.

3.1.2 Synthesis of HAs-doped/ZnO and HS/ZnO and HS/TiO_2 nanoparticles

3.1.2.1 Materials

Ethanol (EtOH, purity ≥ 99.8%), triethylamine (TEA purity ≥ 99.8%), zinc acetate (ZnAc purity ≥ 99.8%), titanium isopropoxide (TTIP purity ≥ 99.7%), isopropanol (i-PrOH purity ≥ 99.8%), acetic acid (AcOH purity ≥ 99%) and sodium hydroxide (NaOH purity ≥ 97%) were purchased by Sigma (Milan, Italy).

Humic Acid Sodium Salt (HASS, purity ≥ 99.8%, CAS number: 68131-04-4) and commercial Humic Acid (HA, purity ≥ 99.8%, CAS number: 1415-93-6) were purchased from Sigma-Aldrich (Milan, Italy). The average molecular weight (MWa) of the purified HASS and HA are 226.14 g/mol and 227.17 g/mol, respectively.

The humic substance (HS) was extracted by agri-food compost furnished by the company Verde Vita S.r.l (Alghero, Sardinia, Italy).

Flexirene FG 20 F, a commercial linear low-density polyethylene (LLDPE), manufactured as 150 μm thick films, was supplied by Blu Plast s.r.l.

Polylactic acid (PLA) (Ingeo 4032D; <2 mol% of D stereoisomer) was purchased from Nature Works (Plymouth, Minnesota, USA); before the use, it was dried under vacuum for 24 h at 40 °C to avoid hydrolysis of the polymer during melting. After drying, 300 μm thick PLA films were prepared by compression moulding performed at 175 °C, with a pressure of 200 bar and quenched to room temperature by means of water-circulating cooling plates.

3.1.2.2 Synthesis procedure of HAs-doped/ZnO nanoparticles

ZnO and Humic Acids-doped/ZnO nanoparticles (HAs-doped/ZnO) were prepared through a bottom-up synthetic strategy under solvothermal conditions using two HAs (i.e., HASS and HA).

ZnO nanoparticles were obtained starting from a solution obtained dissolving a specific amount of Zinc Acetate (ZnAc, 2.64 g) in a mixture of ethanol (72 mL) and TEA (1.68 mL) (sonication for about 15 minutes). Doped nanoparticles were synthesised by mixing the above solution with a solution containing Humic Acid (3.3 mg of HASS or HA in 8 mL of bi-distilled water) to achieve a suspension with a mmol Humic Acid/mol ZnAc ratio equal to 1. The solvothermal treatment was carried out pouring the above mixtures within Teflon mini reactors, in which the liquid volume corresponded to 75% of the total one and placing the vessels into a circulating oven at 120 °C for 2 hours. The final aqueous suspensions of bare ZnO and hybrid HAs-doped/ZnO nanoparticles, named HASS-doped/ZnO and HA-doped/ZnO NPs respectively, were obtained by centrifugation at 12500 rpm for 15 min, after washing 3 times with bi-distilled water. The main steps of the synthesis procedure are shown in Figure 3.1.

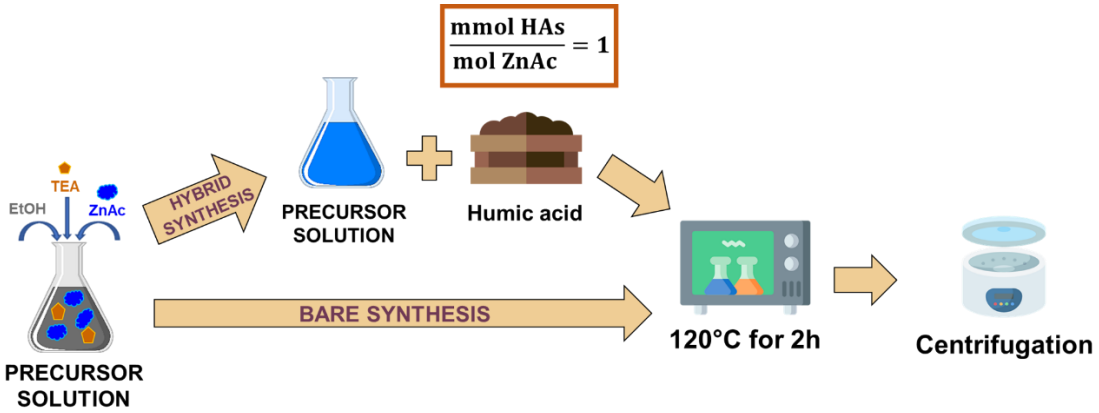

Figure 3.1. Schematic representation of the synthesis of HAs-doped/ZnO nanoparticles.

3.1.2.3 Synthesis procedure of hybrid HS/ZnO and HS/TiO_2 nanoparticles

Hybrid HS/ZnO nanoparticles were synthesized by a similar procedure to that described in Section 3.1.2.2, except for the relative amount of HS with respect to ZnO, realizing in the final suspension the HS/ZnAc weight ratio of 0.041. The solvothermal treatment was carried out at 120 °C for 2 h.

Bare TiO_2 and hybrid HS/TiO_2 nanoparticles were synthetized through solvothermal route as described in the following.
Two different solutions were prepared:

- Solution 1: 12 ml of isopropanol with 12 ml of Titanium isopropoxide (TTIP).
- Solution 2: 62.6 ml of bi-distilled water with 62.6 ml of acetic acid (final pH=1.5).

Solution 1 was added to solution 2 drop by drop and then the mixture was kept under stirring for 24 hours, and a TiO_2 colloidal suspension was obtained.
Hybrid HS/TiO_2 nanoparticles were obtained by adding 150 mg of HS to the colloidal TiO_2 suspension to have a HS/TTIP weight ratio equal to 0.013.
Then TEA was added drop by drop, under stirring, until the pH reached the value of 7. Finally, a solvothermal treatment at 120 °C for 24h was carried out. The suspensions obtained were centrifugated at 11500 rpm for 10 min, washed three times with distilled water and in the end the precipitated product was re-suspended with bi-distilled water. These suspensions were dried in an oven at 80°C and then the nanoparticles were collected. The main steps of the synthesis procedure are shown in Figure 3.2.

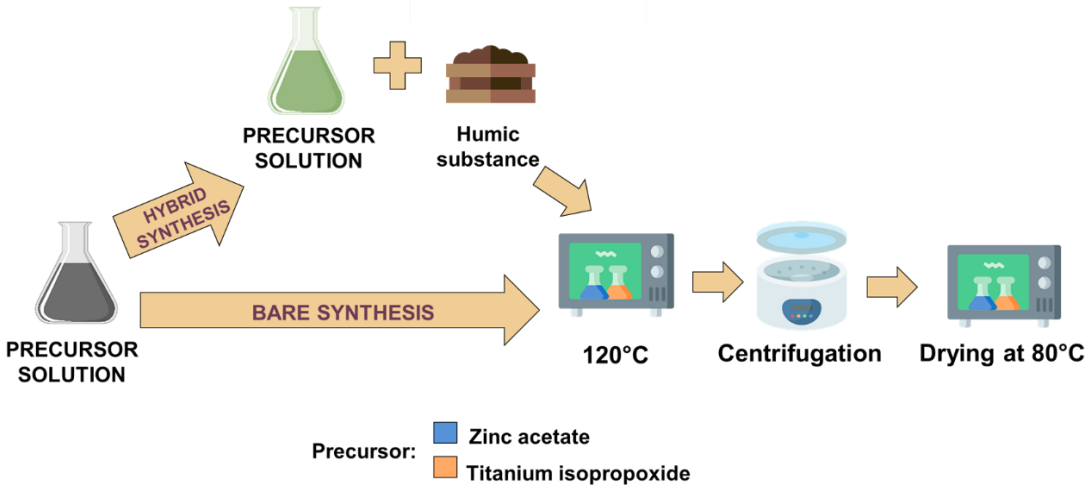

Figure 3.2. Schematic representation of the synthesis of HS/ZnO and HS/TiO_2 nanoparticles.

3.1.3 Physicochemical characterization of photocatalysts

Before the use, a physicochemical analysis of bare, doped and hybrid ZnO and TiO_2 nanoparticles was carried out to analyse morphological, structural, chemical, and optical properties.

3.1.3.1 Physicochemical features of HAs-doped/ZnO nanoparticles

Transmission Electron Microscopy (TEM) micrographs of the bare and doped ZnO nanoparticles are shown in Figure 4.3. Bare ZnO and HAs-doped/ZnO nanoparticles are characterised by a similar average dimension: 152 ± 39 nm for ZnO nanoparticles, 148 ± 46 nm for HASS-doped/ZnO and 140 ± 42 nm for HA-doped/ZnO.

ZnO and HA-doped/ZnO nanoparticles (Figures 3.3a-c and 3.3g-i) form aggregates larger than those observed in HASS-doped/ZnO nanoparticles (Figure 3.3d-f), indicating that HASS affects the nanoparticles formation process, favouring a reduction of the aggregation phenomena, improving the dispersion, which is crucial in determining the final properties [82].

The surface area of all nanostructured materials was evaluated by Brunauer-Emmett-Teller (BET) analysis giving the following values: 16 ± 1 m^2/g (bare ZnO), 10 ± 1 m^2/g (HASS-doped/ZnO) and 14 ± 1 m^2/g (HA-doped/ZnO).

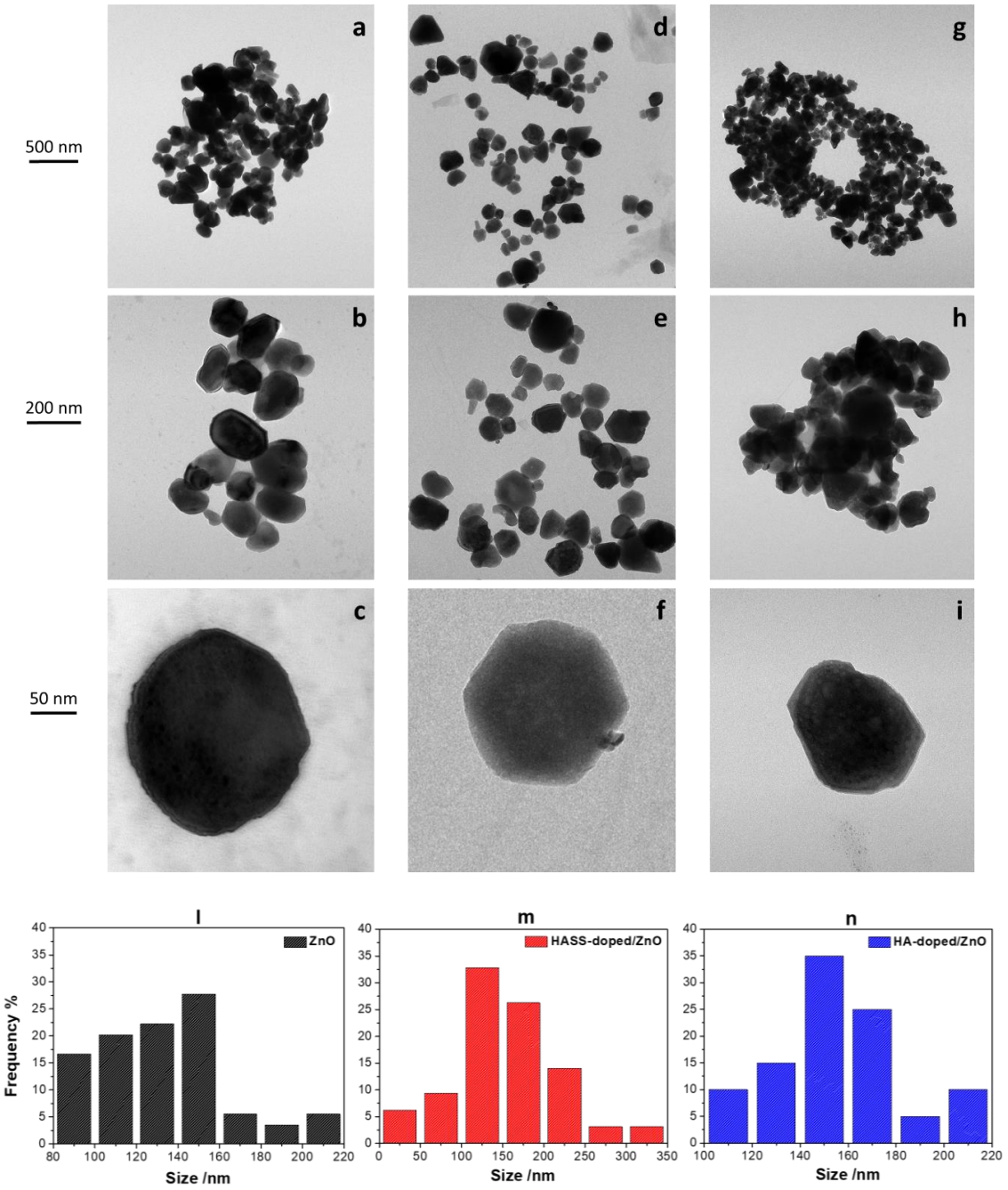

Figure 3.3. TEM micrographs of bare ZnO (a-c), HASS-doped/ZnO (d-f) and HA-doped/ZnO (g-i) nanoparticles. The relative size histograms are displayed in (l), (m) and (n), respectively.

The X-Ray Diffraction (XRD) patterns of bare humic acids (Figure 3.4a) show a few weak diffraction peaks on the amorphous background related to the presence of some inorganic materials, typical of clay soil, while ZnO and ZnO doped nanoparticles (Figure 3.4b) are characterised by a crystalline structure corresponding to wurtzite, which is the typical hexagonal crystal structure of zinc oxide [83–85]. This result indicates that the presence of HAs did not hinder the crystallization of wurtzite during the solvothermal treatment. The mean crystallite sizes were determined by Scherrer's equation (see Section 5) giving ~70 nm for bare ZnO, ~80 nm for HASS-doped/ZnO and ~60 nm for HA-doped/ZnO.

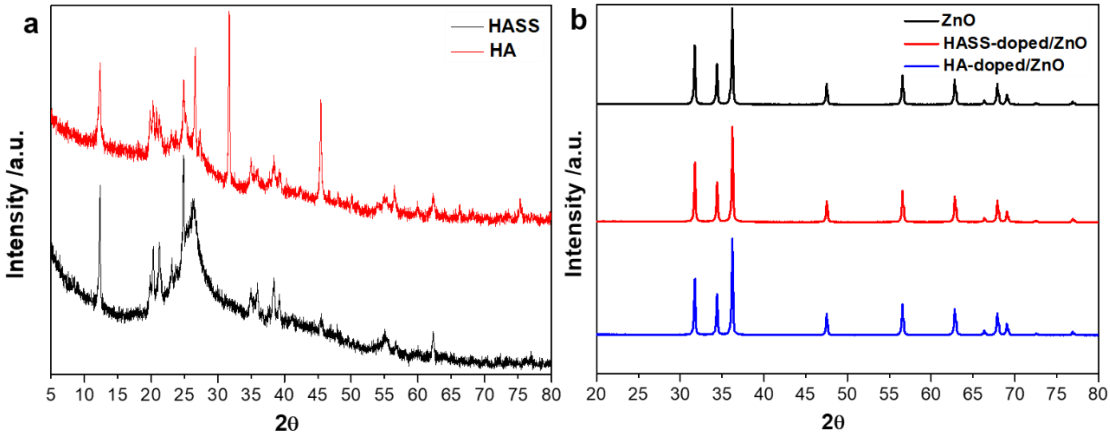

Figure 3.4. XRD profiles of (a) HASS and HA powders and (b) bare ZnO, HASS-doped/ZnO and HA-doped/ZnO nanoparticles.

Thermogravimetric (TG) curves of ZnO, HASS-doped/ZnO and HA-doped/ZnO samples, recorded in N_2 atmosphere, are displayed in Figure 3.5.

They show two marked weight losses between ~100°C and ~500°C, and between ~500°C and ~1000°C, related to the main decomposition of humic acids. According to the proximate analysis procedure described elsewhere [80], the fraction of humic acids within HASS-doped/ZnO and HA-doped/ZnO nanoparticles was estimated to be ~1.6 and ~1.0 w/w%, respectively. This difference could be due to a diverse chemical behaviour of humic acid precursors. The dispersion in the synthesis mixture of the HASS seems favoured compared to HA, in agreement with TEM results, leading to a homogeneous

conjugation with ZnO nanocolloids, that is mainly driven by the presence of aromatic moieties in humic acids acting as ligands for Zn^{2+} ions [86].

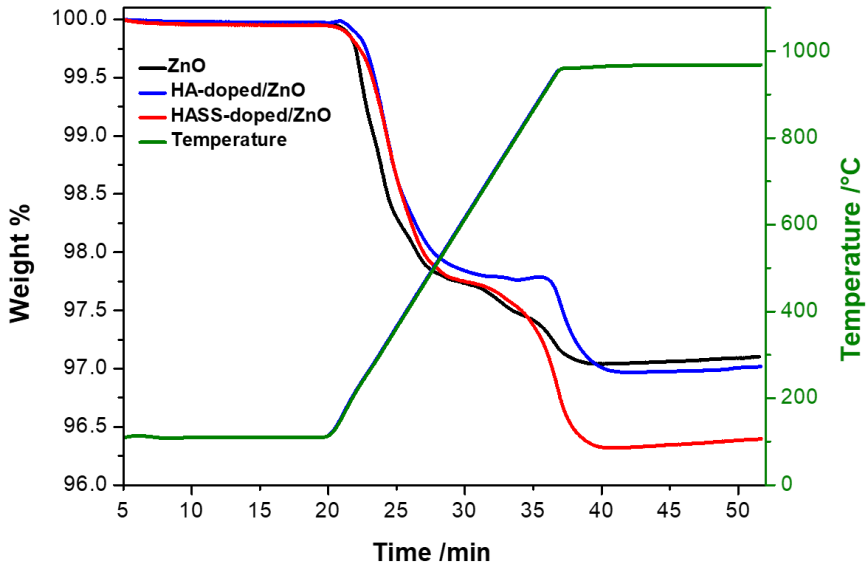

Figure 3.5. TG curves of bare ZnO, HASS-doped/ZnO and HA-doped/ZnO nanoparticles.

The nature of the paramagnetic centres and the supramolecular organization of the organic moiety within the nanomaterials was investigated by Electronic Paramagnetic Resonance (EPR) spectroscopy.

EPR spectrum of bare ZnO nanoparticles (Figure 3.6a) shows the typical large and not-intense signal centered at g-factor value of 1.9565 ± 0.0003, which correspond to bulk Zn^{2+} specie, typical of crystalline zinc oxide nano-powders [87,88]. Besides this characteristic signal of the inorganic component, EPR spectra of HASS-doped/ZnO and HA-doped/ZnO nanoparticles (Figure 3.6b) show a second single and roughly symmetric signal centered at a g-factor value of 2.0033 ± 0.0003, due to the presence of paramagnetic species belonging to HAs moiety, as confirmed by EPR spectra of bare HASS and HA powders (Figure 3.6b). As shown in Figure 3.6b, each signal can be ascribable to the single peak typical of carbon-centered radicals found in humic substances and/or similar polyphenol-like molecules [89–92].

However, some differences in the line shapes were detected. First, the peak corresponding to HASS-doped/ZnO sample appears more symmetric and broader than that of pure HASS, while the peak corresponding to HA-doped/ZnO results more asymmetric and narrower than that of pure HA. This evidence indicates that some chemical and structural changes were induced in the organic component as a consequence of the conjugation with the inorganic one, giving peculiar properties to the hybrid nanoparticles.

These findings were also confirmed by the quantitative determination of the signal amplitude, ΔB, which is related to the line-width of EPR peak, and directly detectable by the experimental spectra (Figure 3.6b). Being the signal line-width dependent on the relaxation time of spinning electrons and mainly affected by the interaction between unpaired electrons with the neighbouring-atoms, this ΔB parameter is usually considered a qualitative indication of the distance between the radical centres and the chemical heterogeneity of the radical species. The lower ΔB value observed for HASS-doped/ZnO ($\Delta B = 4.7 \pm 0.2$) than that of HA-doped/ZnO ($\Delta B = 5.6 \pm 0.3$) indicates that the radical centres of HASS-doped/ZnO are further away than HA-doped/ZnO. This evidence indirectly confirms that the distribution and structural organization of the two humic acids within the ZnO doped nanoparticles were different, thus tuning their growth. The estimated values of ΔB are reported in Table 3.1.

This behaviour was also confirmed by EPR spectra recorded increasing the incident microwave power and by the trends of the corresponding power saturation curves, which were built by plotting the normalized peak amplitude (A/A_0) as function of the square root of the normalized microwave power (P/P_0), as displayed in Figure 3.6c.

The different relative intensity of the EPR peak detected for the two doped samples indicates a greater amount of radical centres in HASS-doped/ZnO than HA-doped/ZnO, also suggesting a higher content of organic phase in the HASS-doped/ZnO than in HA-doped/ZnO, in agreement with TG results.

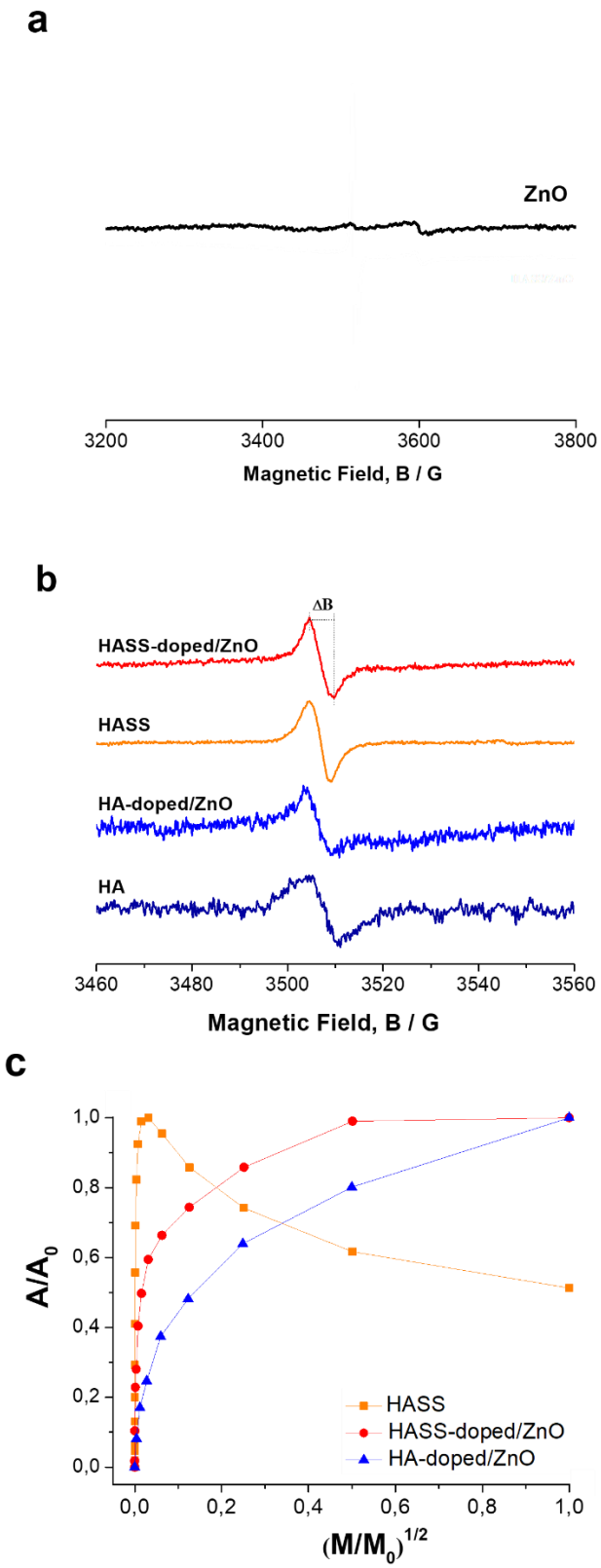

Figure 3.6. EPR spectra of (a) bare ZnO nanoparticles, (b) HASS-doped/ZnO and HA-doped/ZnO nanoparticles compared to pure HASS and HA powders; (c) Power saturation curves of pure HASS and HASS-doped/ZnO and HA-doped/ZnO nanoparticles.

The generation of ROS in aqueous environment under UVA irradiation by means of HAs-doped/ZnO was demonstrated by EPR spin-trapping method (Figure 3.7). This approach allows to reveal the formation of extremely unstable radical species with too short lifespan, such as ROS, through a direct reaction with a specific amount of 5,5-Dimethyl-1-pyrroline N-oxide (DMPO) spin-trap, obtaining longer-living spin-adducts more easily detectable by EPR spectroscopy at room temperature. Firstly, the lack of any interfering signal due to DMPO was preventively checked. Then, after UVA irradiation, the appearance of an EPR signal, formed by a quartet with a 1:2:2:1 intensity ratio, was detected for the supernatants of bare and ZnO doped suspensions (Figure 3.7). This corresponds to the typical signal of DMPO-OH adduct formed from the trapping of •OH radicals by DMPO molecule, as confirmed by the values of the hyperfine coupling constants for the nitroxide nitrogen and for the β-proton, $a_N = a^{\beta}_H = 14.8 \pm 0.2$ G. These values agree with those reported in the literature for DMPO-OH adduct, thus confirming the generation of •OH species after UVA irradiation. Interestingly, the DMPO-OH spectra corresponding to both HAs-doped/ZnO nanoparticles show a greater relative intensity than that of bare ZnO, thus indicating an enhanced ROS-generating ability in aqueous medium after UVA irradiation. This effect should be ascribable to the doping of ZnO with the organic moieties already stabilizing carbon-localized free-electrons which, thanks to the fine combination at molecular scale with the semiconductor material, could improve the photocatalytic activity.

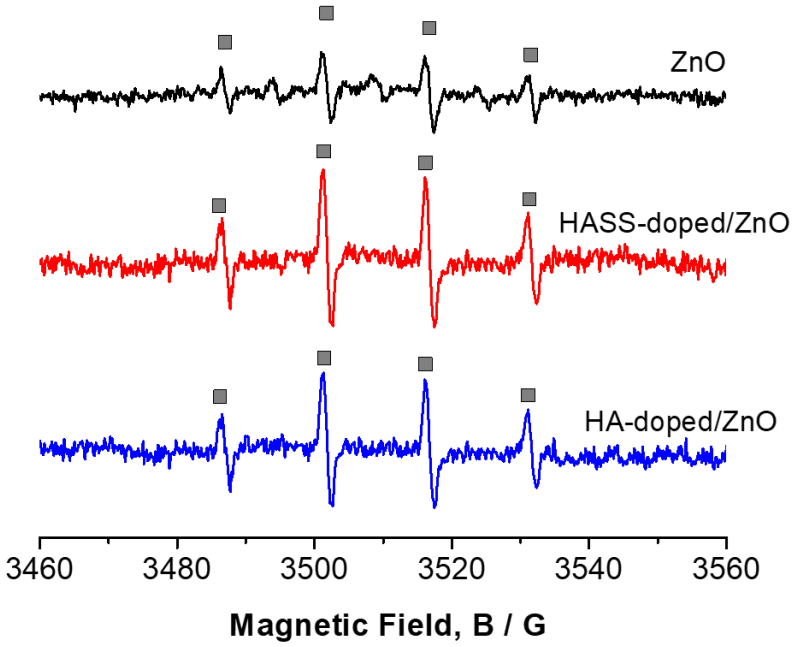

Figure 3.7. DMPO spin-adducts formed in aqueous medium in the presence of ZnO, HASS-doped/ZnO and HA-doped/ZnO nanoparticles after UVA irradiation.

Diffuse-Reflectance UV-vis (DRUV) spectra of bare ZnO and ZnO-doped nanoparticles show an absorption peak at around 360 nm, which is typical of ZnO (Figure 3.8a). No differences were observed between bare and doped nanoparticles. The Kubelka-Munk function allowed to determine the energy bandgap values of ZnO, HASS-doped/ZnO and HA-doped/ZnO nanoparticles (Figure 3.8b). The optical bandgap were calculated by Tauc plot linearization of $(F(R)h\nu)^2$ against photon energy and result to be equal to 3.3 eV, in agreement with the literature [93]. These findings suggest that the optical properties of ZnO were not modified by the presence of HAs, considering the low amount of organic content used in the synthesis of hybrid catalysts.

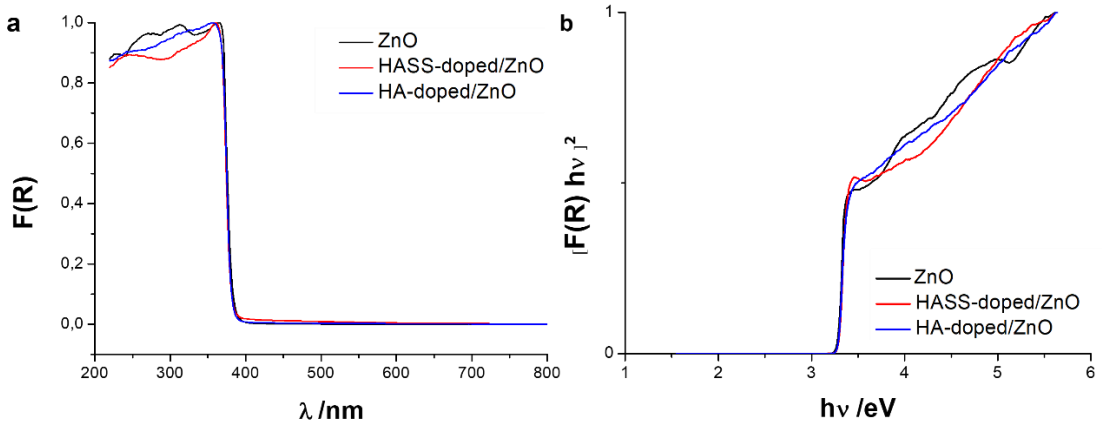

Figure 3.8. DRUV spectra (a) and Tauc-Plot linearization (b) of bare ZnO, and HASS-doped/ZnO and HA-doped/ZnO nanoparticles.

The main physicochemical features of HASS-doped/ZnO and HA-doped/ZnO nanoparticles are compared with respect to those of bare ZnO, HASS and HA samples in Table 3.1.

Table 3.1. Main physicochemical properties of HASS-doped/ZnO and HA-doped/ZnO nanoparticles compared to those of bare ZnO, HASS and HA samples.

Sample	Organic amount (w/w %)	Crystallites mean size (diameter, nm)	Surface area (m^2/g)	ΔB (G)
ZnO	-	152 ± 39	16 ± 1	-
HASS-doped/ZnO	1.6	148 ± 46	10 ± 1	4.7 ± 0.2
HA-doped/ZnO	1.0	140 ± 42	14 ± 1	5.6 ± 0.3
HASS	100	-	-	4.2 ± 0.2
HA	100	-	-	6.9 ± 0.3

3.1.3.2 Physicochemical features of hybrid HS/ZnO and HS/TiO_2 nanoparticles

The morphology of HS/TiO_2 and HS/ZnO nanoparticles was assessed by TEM images (Figure 3.9). HS/TiO_2 nanoparticles show a rod-like morphology of ~15 nm for the longest side (Figure 3.9A) and form irregular nanoclusters, that are smaller than those of bare TiO_2 nanoparticles (~30-35 nm) (Figure 3.9C) [86], indicating that HS tuned the nanoparticles growth clustering during the solvothermal process.

For HS/ZnO nanoparticles a marked morphological arrangement was seen with the formation of uniform pseudo-spherical clusters (~250 nm, diameter) (Figure 3.9B), due to the double role played by the organic component that acts both as templating agent for the growth of the hybrid nanoparticles [80], and as a modulating agent of their self-assembly. TiO_2-based nanoparticles exhibit mesoporous character with a constrained cavity distribution, i.e. pores arrange to create cavities or spaces of limited size and shape, thus affecting the adsorption properties and restricting the mobility of the molecules and/or atoms within them. ZnO-based nanoparticles do not show any porosity, thus presenting a lower surface area than TiO_2-based ones.

As reported in Table 3.2, hybrid nanoparticles show a slightly increased specific surface area compared to the bare ones, thus confirming the key role of HS in tuning the surface properties of the hybrid nanomaterials.

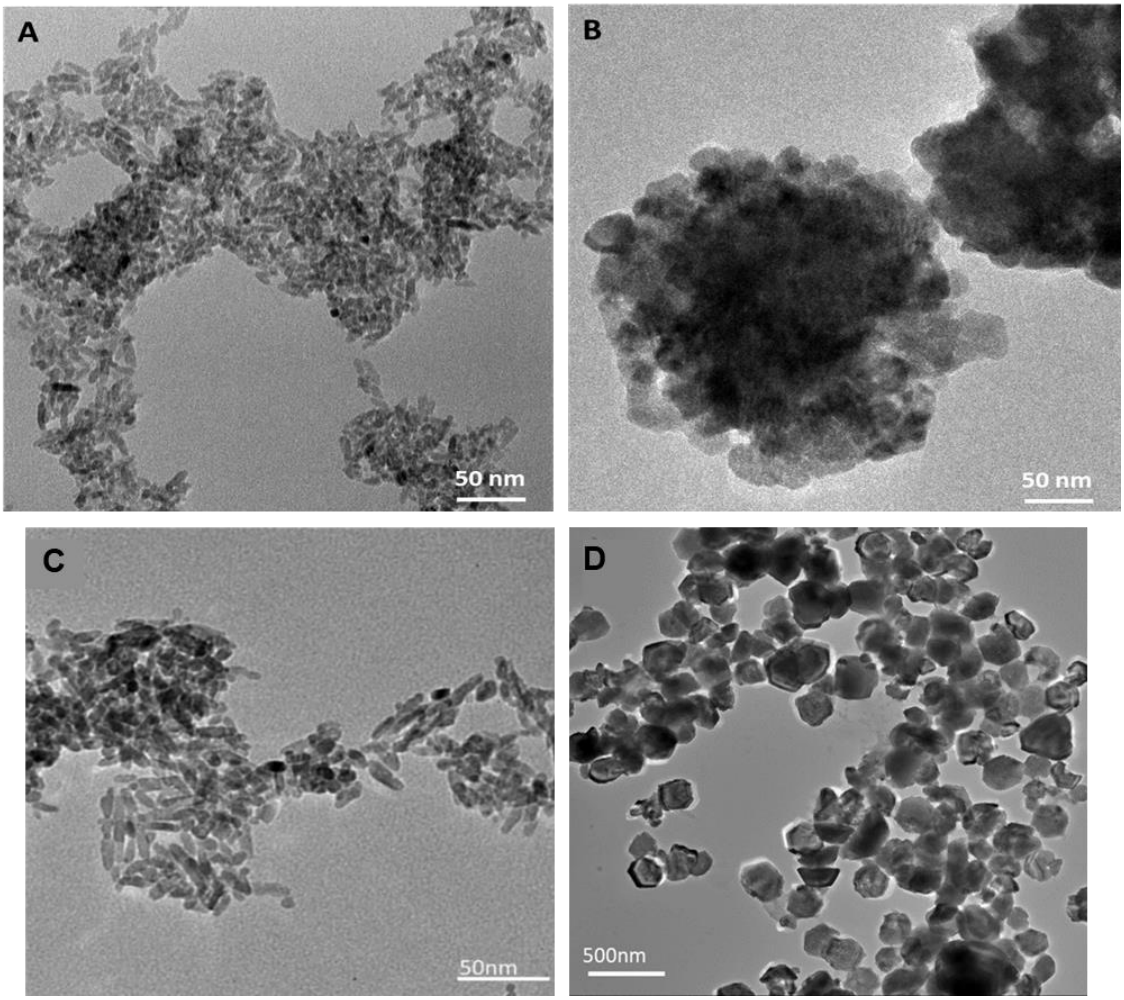

Figure 3.9. TEM images of hybrid HS/TiO_2 (A) and HS/ZnO (B) nanoparticles; bare TiO_2 (C) and ZnO (D) nanoparticles.

XRD patterns of HS, TiO_2, HS/TiO_2, ZnO and HS/ZnO are displayed in Figures 3.10A-C. HS shows an amorphous structure, while HS/TiO_2 and HS/ZnO nanoparticles exhibit a typical crystalline structure. Their profiles are related to TiO_2 anatase [94] and ZnO wurtzite structure [80,84,85], respectively. It should be noted in the pattern of HS/ZnO the partial splitting of the two most intense diffraction peaks took place, indicating that the presence of HS promotes the formation of two different crystal populations (insight of Figure 3.10C). This feature might be due to the adsorption of HS moieties on the ZnO crystallite surface and to the intimate conjugation with Zn^{2+} sites, thus inducing some structural changes of the crystalline organization. The values of crystallite size calculated by Scherrer equation (see Section 5) are reported in Table 3.2.

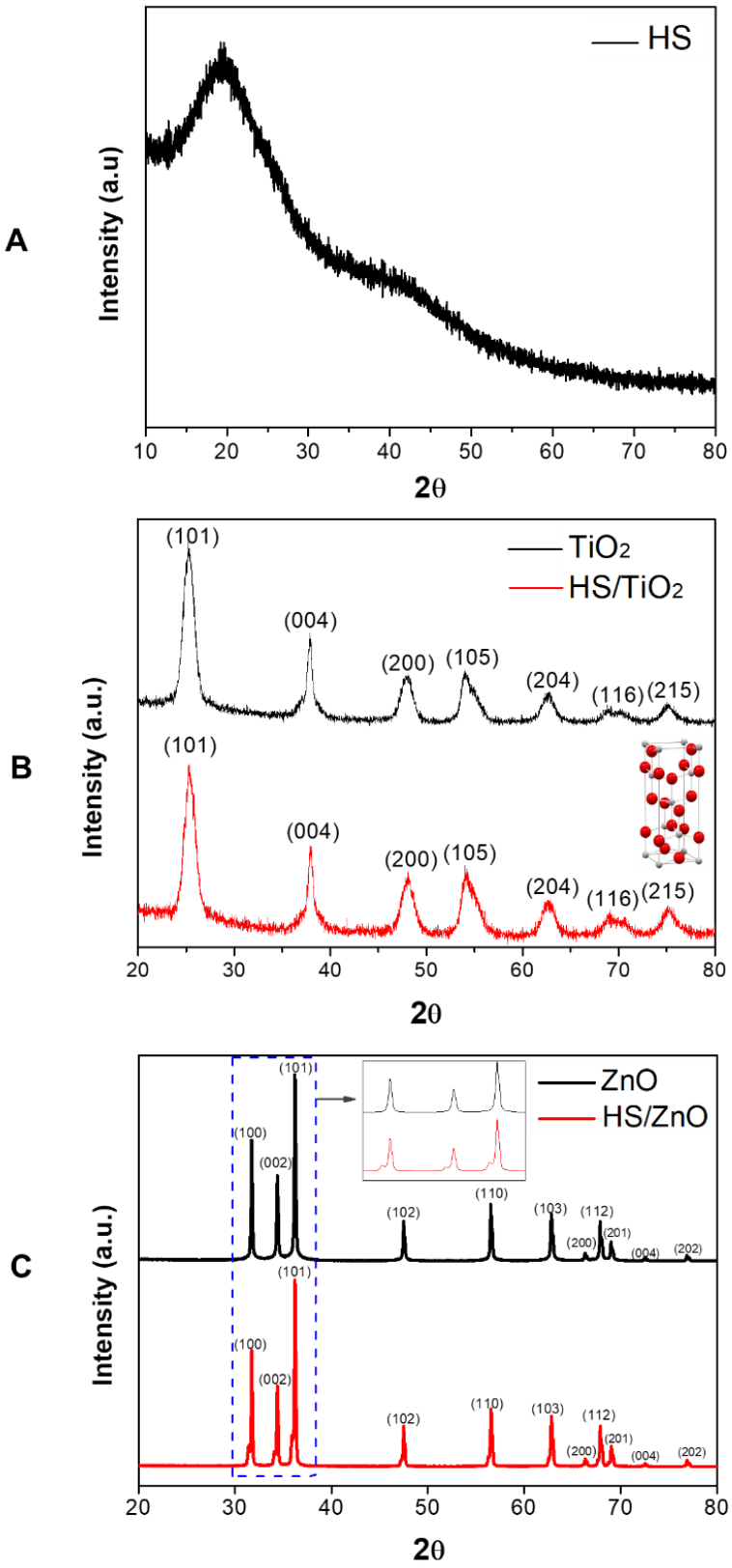

Figure 3.10. XRD patterns of HS (A), bare TiO_2 and HS/TiO_2 nanoparticles (B), and bare ZnO and HS/ZnO nanoparticles (C).

The chemical conjugation of HS with the inorganic component was also confirmed by Fourier Transform Infrared (FTIR) analysis (Figures 3.11 and 3.12).

The comparison of the spectra of HS/TiO_2 that of bare TiO_2 show that the main changes concern the appearance of bands at 1400 cm^{-1} ((δ_{O-H}), (δ_{COO^-}), (δ_{C-H}) bending vibrations), the increase of the intensity of the bands at 3445 cm^{-1} (ν_{O-H}) and 1630 cm^{-1} (($\nu_{C=C}$), (δ_{HOH})) and the slight shift of the band related to vibrational modes of Ti-O bonds towards higher wavenumbers. This suggests that HS moieties act as ligands for Ti^{4+} ions, causing a covalent complexation between HS and Ti^{4+} ions.

Likewise, the appearance of a new band at 1033 cm^{-1} corresponding to stretching vibration of phenolic C-O (ν_{C-O}), as well as the slight shift of the band related to Zn-O stretching confirms that HS was successfully conjugated with the inorganic matrix and that its aromatic moieties served as ligands for Zn^{2+} ions (Figure 3.12).

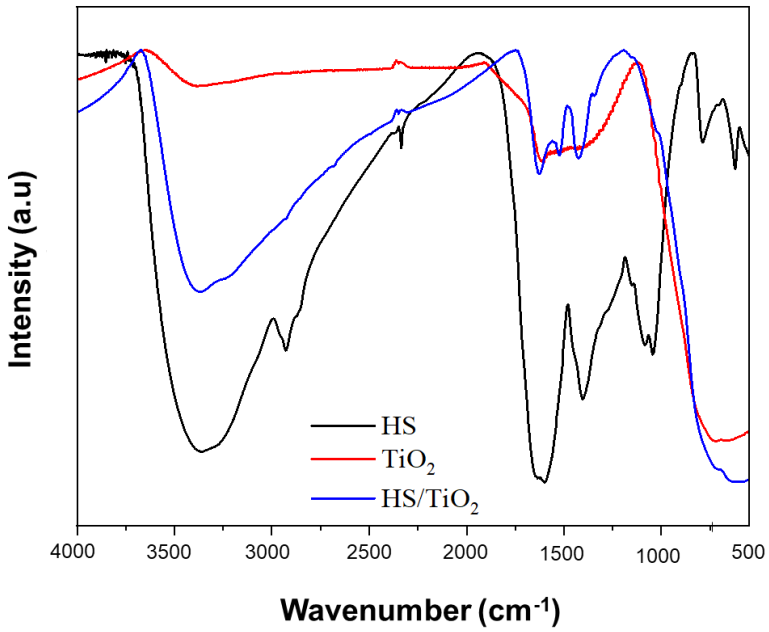

Figure 3.11. FTIR spectra of bare HS, bare TiO_2 and HS/TiO_2 nanoparticles.

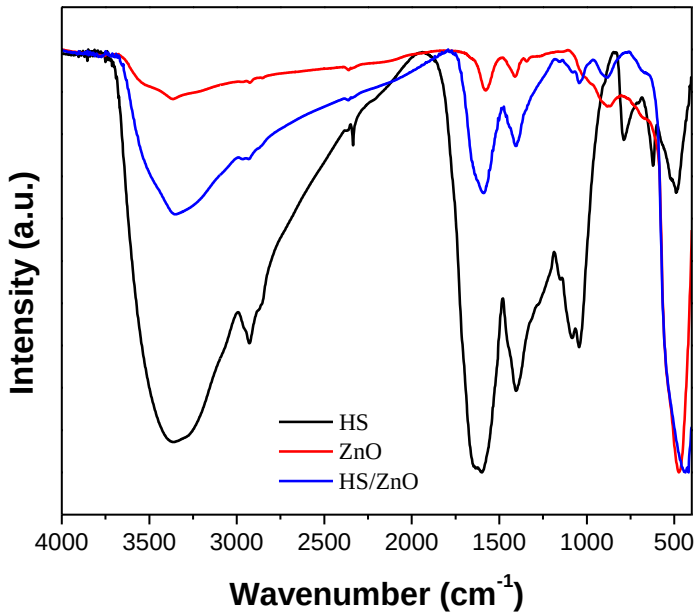

Figure 3.12. FTIR spectra of bare HS, bare ZnO and HS/ZnO nanoparticles.

ζ-potential titration (Figure 3.13) shows that HS consistently displays negative values across the entire pH range, whereas both TiO_2 and ZnO nanoparticles exhibit pH_{zpc} values at approximately 6.6 and 8.0, respectively. Since the synthesis was conducted at pH = 7.0, TiO_2 exhibited a slight negative charge likewise HS, on the contrary ZnO was positively charged. This observation pointed to a potential difference in the type of interaction of HS with TiO_2 compared to ZnO, favoring a higher adsorption of organic molecules on ZnO. The HS adsorption on the metal oxide surface was favored by electrostatic attraction contribute depending on the surface charge of nanoparticles and the pH of the matrix in which the complexation occurred [95,96].

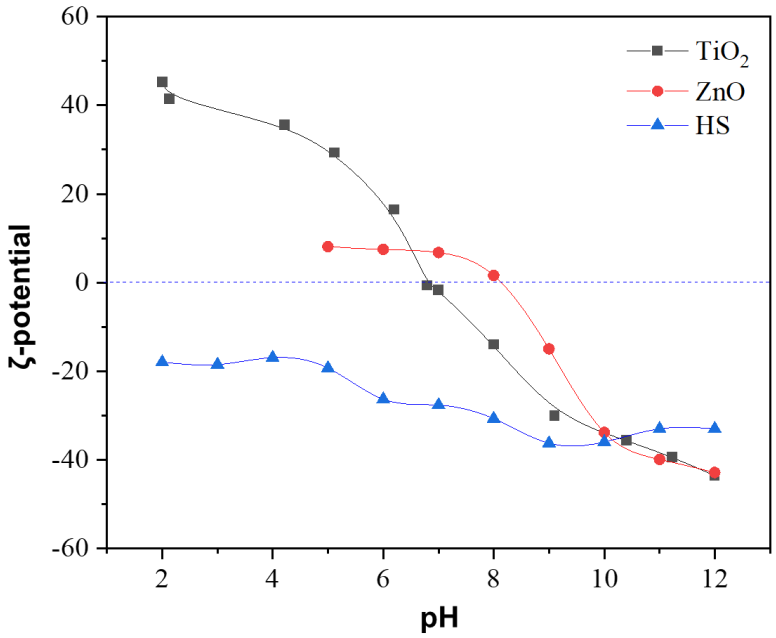

Figure 3.13. ζ potential trends of TiO_2, ZnO and HS.

The TG curves of hybrid ZnO and TiO_2 nanoparticles recorded in N_2 atmosphere confirms that a greater amount of HS was entrapped into HS/ZnO than in HS/TiO_2 nanoparticles (Figures 3.14 A,B).

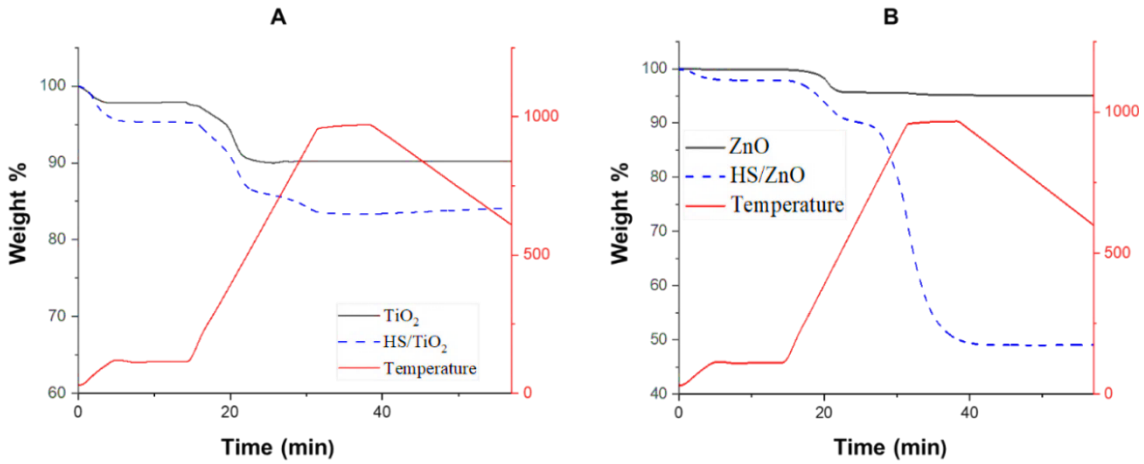

Figure 3.14. Weight loss percentage of TiO_2 and hybrid HS/TiO_2 (A), ZnO and hybrid HS/ZnO (B) nanoparticles evaluated by proximate analysis.

This evidence was further confirmed by Folin-Ciocâlteu assay results which indicated the larger presence of phenolic groups in HS/ZnO ($mg_{equivalent\ gallic\ acid} \cdot g_{sample}^{-1}$ = 43.6) than in HS/TiO_2 nanoparticles ($mg_{equivalent\ gallic\ acid} \cdot g_{sample}^{-1}$= 6.6), as also summarized in Table 3.2.

The HS presence into hybrid nanoparticles was also confirmed by EPR spectroscopy, describing the nature of organic paramagnetic centres. In fact, both HS/TiO_2 and HS/ZnO EPR spectra (Figure 3.15) show the presence of a single peak centered at a g-factor value of 2.0035 ± 0.0003, which is typical of carbon-centered radicals found in HS and ascribed to the presence of mobile free-electrons stabilized onto aromatic moieties. The comparison of the spectra of both hybrid nanoparticles shows some differences in the line shape of EPR peaks. The signal related to HS/ZnO nanoparticles appears more asymmetric and broader than that of pure HS, indicating that some chemical and structural changes were induced in the organic component due to the conjugation with the inorganic one. In contrast, the signal corresponding to HS/TiO_2 sample do not show any significant change [86,91]. This finding was quantitatively confirmed by the estimation of the signal amplitude parameter, ΔB, which is related to the linewidth of the EPR peak, as directly detectable by the spectra (Figure 3.15**),** and an index of the chemical and spatial distribution of the radical centres. As reported in Table 3.2, $\Delta B_{HS/ZnO}$ is higher than $\Delta B_{HS/TiO_2}$, indicating that radical centres are located much closer in HS/ZnO than in HS/TiO_2 nanoparticles. This effect could be a consequence of the higher amount of HS conjugated with ZnO than TiO_2, as indicated by TGA analysis [89], and of the greater value of the spin-density of HS/ZnO than that of HS/TiO_2 (Table 3.2).

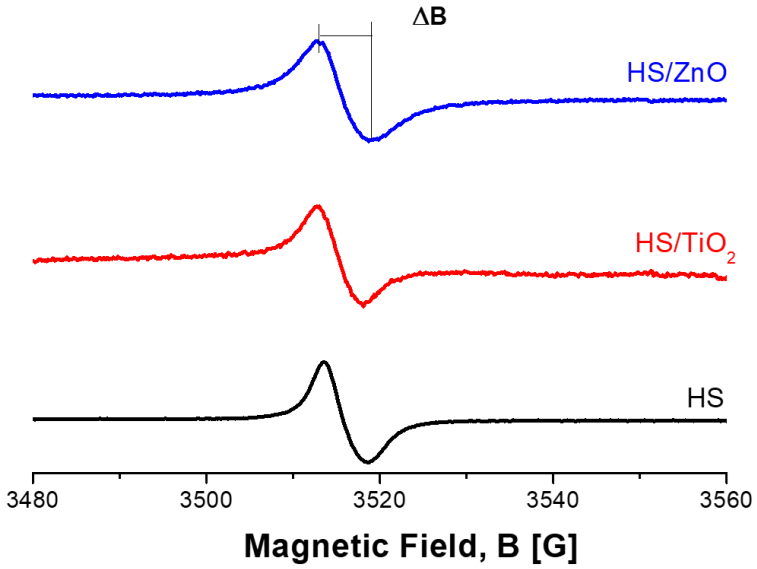

Figure 3.15. EPR spectra of bare HS, hybrid HS/TiO_2 and HS/ZnO nanoparticles.

DRUV spectra of HS/TiO_2 nanoparticles reveal, beside the typical absorption band of TiO_2 in the range 200-400 nm [97], a significant increase in the absorption band in the visible range ($\lambda >$ 400 nm), which could be ascribable to HS widespread adsorption in the visible region (Figure 3.16A).

For hybrid HS/ZnO nanoparticles, a broad absorption below 400 nm typical of zinc oxide [98] was detected (Figure 3.16B**)**, and only a slight increase in the absorption band in the visible range is observed, due to the conjugation with HS [99].

The broad absorbance in the visible region can be ascribable to the presence of different types of electron acceptors and donors present in HS. This absorbance was probably induced by the near proximity of the electron donors "D" (i.e., polyhydroxylated aromatic and phenol) and the electron acceptors "A" (i.e., quinone). Indeed, if D and A centres interacted in the ground state to form D-A charge-transfer complexes, optical charge-transfer bands could arise. Novel absorption bands could be seen in D-A complexes that neither D nor A molecules alone display. These bands might be generated when photon absorption promoted an electron transfer from D to A completely or partially [100].

The values of the energy bandgap for all nanoparticles were calculated using the Kubelka-Munk function (Figure 3.17). The conjugation of the metal oxide with HS did not induce a significant change in the energy bandgap of nanoparticles (Table 3.2), which could be explained as a direct consequence of the two-fold behaviour of HS acting as both electron acceptor and donor.

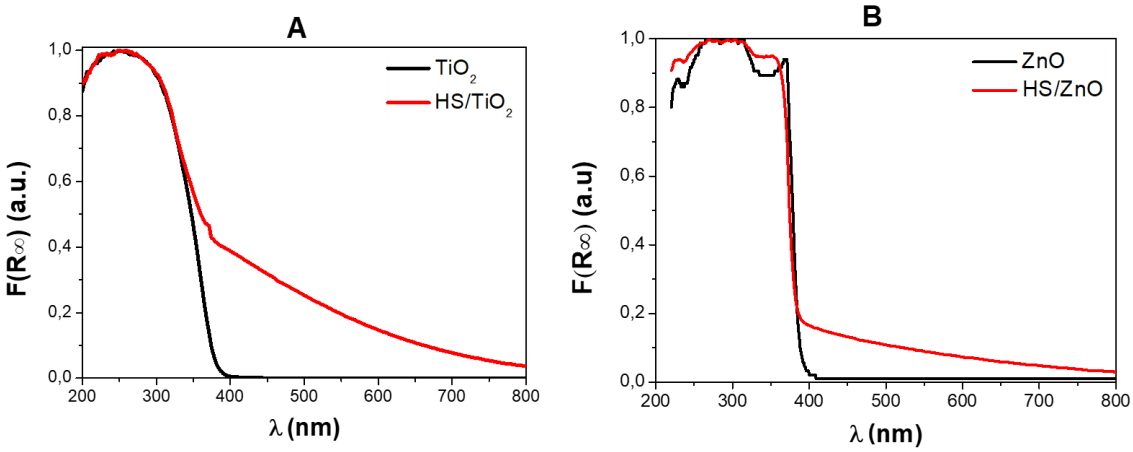

Figure 3.16. Absorption spectra of TiO_2 and hybrid HS/TiO_2 nanoparticles (A), ZnO and hybrid HS/ZnO nanoparticles (B).

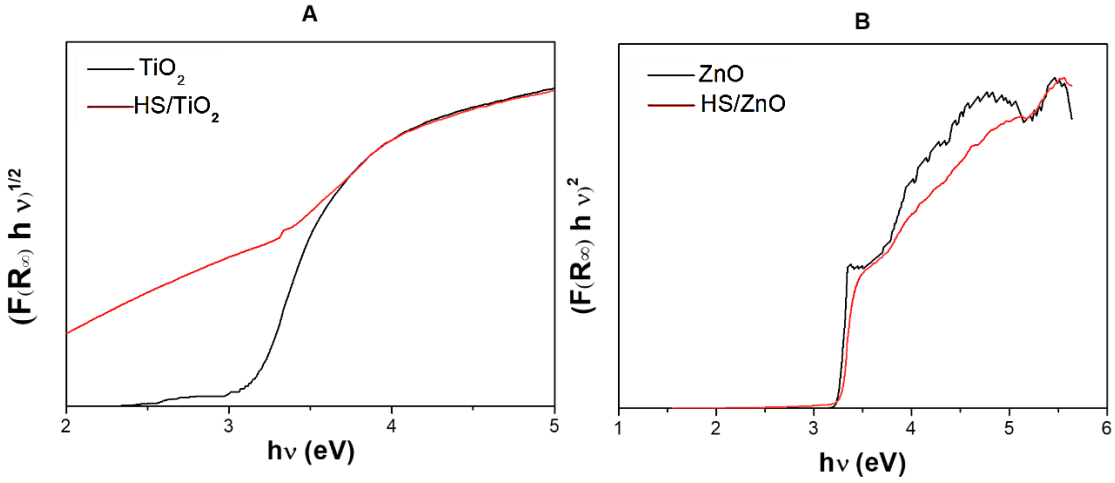

Figure 3.17. Tauc Plot of TiO_2 and hybrid HS/TiO_2 (A)**,** Tauc plot of ZnO and hybrid HS/ZnO (B).

The results of excitation-resolved photoluminescence (PLE) analysis on bare and hybrid HS/ZnO and HS/TiO_2 nanoparticles as dry powders are reported in Figure 3.18A-F.
Notably, the measurements performed on neat HS did not yield any significant PL signal. On the other hand, the conjugation of HS with metal-oxide nanoparticles resulted in a noticeable alteration of PL intensity in all cases. However, the spectral features, i.e. peak position, spectral widths, and overall distribution of excitation/emission intensity (as represented by the PLE maps) remained unchanged. This observation, coupled with the negligible PL signal of HS samples, suggests that the presence of HS in nanoparticles, rather than creating new recombination channels or causing noticeable shifts in PL spectra, affected the population of charge carriers involved in radiative recombination processes. The conjugation with HS affected the PL intensity of the two oxides in the opposite manner: it led to a PL increase in the case of TiO_2 and to a PL decrease in the case of ZnO. Such a difference is likely to be explained by the electronic coupling of HS with the two oxides, i.e., by different tendencies of HS to transfer mobile charge carriers into the metal oxide semiconductor.
PL emission of anatase TiO_2 arises from the radiative recombination of free electrons with trapped holes, as strongly suggested by several works showing that exposure to electron scavenging O_2 causes a quenching of the PL intensity [101–103]. These radiative recombination processes are mostly responsible for the green component of the PL spectra [104,105] and, interestingly, the comparison between Figures 3.18A and 3.18C highlight that the enhanced PL of HS/TiO_2 was slightly shifted towards the green region (lower wavelengths) with respect to the PL of bare TiO_2. It can be thus hypothesized that HS injected mobile electrons into the conduction band of TiO_2, increasing the net number of radiative recombination processes and thus enhancing the PL activity.
A similar phenomenon can be hypothesized to occur in HS/ZnO nanoparticles, in which HS component tend to accept the free electrons from ZnO, thus increasing the charge separation and lowering the PL intensity.

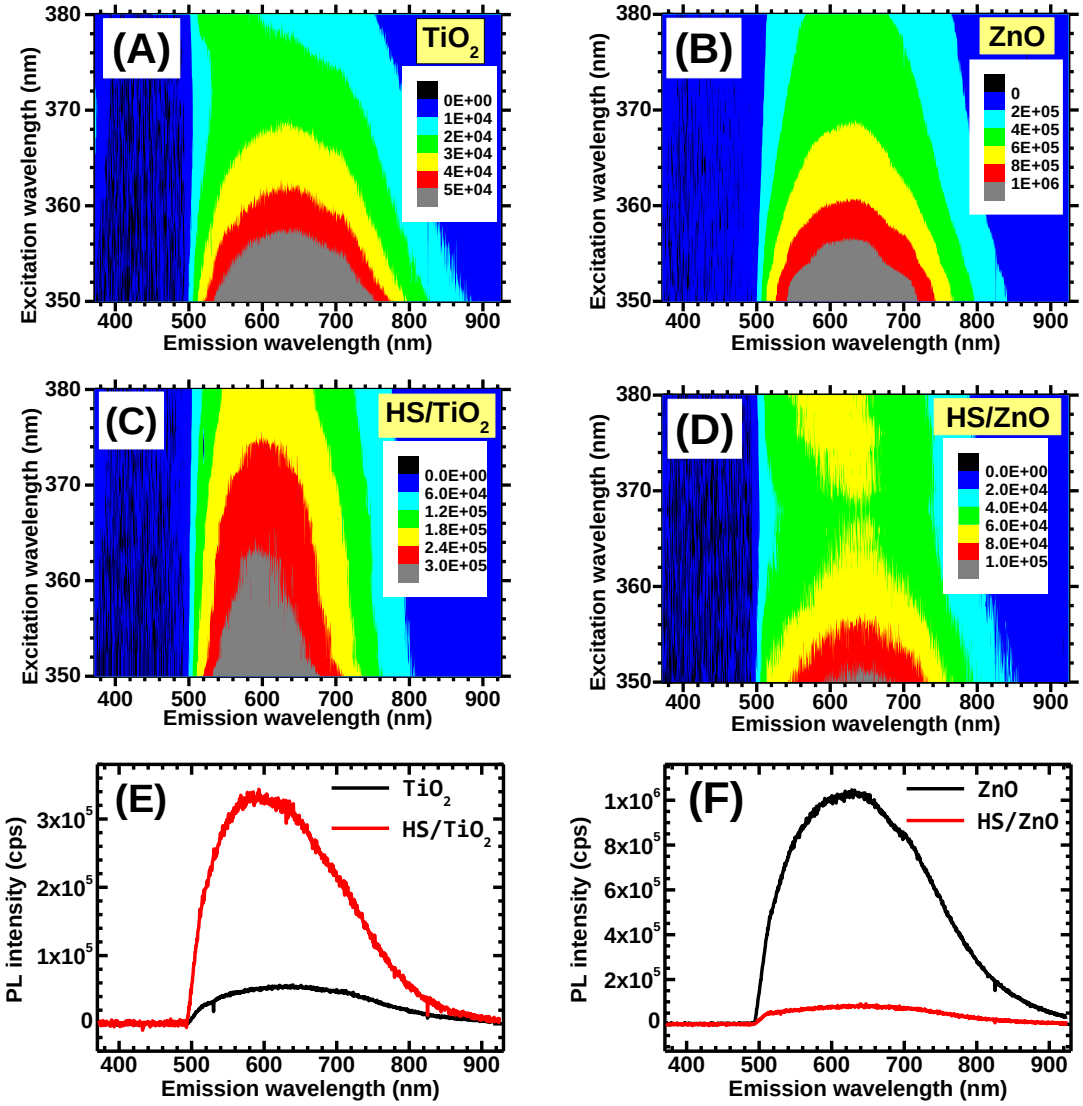

Figure 3.18. PLE intensity maps for TiO_2 nanoparticles (A), ZnO nanoparticles (B), hybrid HS/TiO_2 nanoparticles (C) and hybrid HS/ZnO nanoparticles (D). The comparison with the intensity scale shows that the PL intensities at all excitation wavelengths are in the case of TiO_2 enhanced as a consequence of the conjugation with the HS, while the opposite happens for ZnO. PL spectra (E and F) measured at the same excitation wavelength $\lambda_{exc} = 356\,nm$ for the pure metal oxide (black curves) and the hybrid composite (red curve). The intensity units are comparable in all the spectra and all measurements were acquired in inert ambient (N_2).

Table 3.2. Values of main physicochemical parameters of bare and hybrid ZnO and TiO_2 nanoparticles.

Physicochemical properties	**TiO_2**	**ZnO**	**HS/TiO_2**	**HS/ZnO**	**HS**
Average size (nm)	27 ± 6	220 ± 45	15 ± 4	243 ± 60	-
Crystallite average size (nm)	6.3 ± 1.7	35.1± 6.9	6.5 ± 2.1	34.2 ± 7.6	-
Surface area ($m^2 \cdot g^{-1}$) (err.≤7%)	222.1	16.1	231.7	17.8	-
Organic & HS content % (err.≤2%)	7	4	10	52	-
mg equivalent gallic acid $\cdot g_{sample}^{-1}$	-	-	6.6 ± 1.0	43.6 ± 3.5	-
g-factor (err. ±0.0003)	-	-	2.0038	2.0037	2.0035
ΔB (G)	-	-	5.4 ± 0.2	6.0 ± 0.2	5.6 ± 0.2
Spin x g^{-1} (err. ≤10%)	-	-	6.2×10^{16}	2.2×10^{17}	5.8×10^{17}
Band gap energy (eV) (err. ±0.02)	3.18	3.24	3.32	3.27	-

3.1.4 Photodegradation tests of polymer samples

The experimental tests were carried out using a high-pressure Hg vapour lamp (UV 12 F HeliosItalquartz) with a nominal output of 125 W. The lamp emits light at 305, 313 and 366 nm in the UV range and at 404.7 and 435.8 nm in the visible range. It was installed inside a quartz sleeve in which cooling water circulated at 25 °C and maintained at that temperature by using a thermostatic bath (Falc GTR 90). The effective powers emitted by the lamp are: $I_{305nm} = 6.08 \cdot 10^{-7}$ Ein·s^{-1}, $I_{313nm} = 2.05 \cdot 10^{-6}$ Ein·s^{-1}, $I_{366nm} = 1.19 \cdot 10^{-6}$ Ein· s^{-1}, in the UV spectrum; $I_{404.7nm} = 3.92 \cdot 10^{-6}\ Ein \cdot s^{-1}$, $I_{435.8nm} = 4.22 \cdot 10^{-6}\ Ein \cdot s^{-1}$ in the visible spectrum.

The photocatalytic experiments were also carried out by exploiting natural solar radiation.

3.1.4.1 Photodegradation tests of LLDPE and PLA slices under UVA irradiation

Nanostructured films were prepared by drop-casting method: 0.4 mL of each suspension of either bare ZnO or HASS-doped/ZnO and HA-doped/ZnO nanoparticles at a concentration 5 mg/mL were alternatively deposed on glass supports (4×2 cm). Then, these supports were placed in an oven for 30 minutes at 90 °C allowing the solvent removal and leading to dry films (Figure 3.19).

Figure 3.19. Glass supports with nanostructured films of ZnO, HASS-doped/ZnO and HA-doped/ZnO nanocatalysts.

Photodegradation tests were performed deposing on the above substrates LLDPE and PLA slices. For each ZnO-based photocatalytic material four sets of slices of LLDPE and PLA (4×2 cm) were used and dipped in a bath containing water and then exposed to UVA irradiation for 75 h and 225 h (see Figure 3.20). The presence of water was provided to favour the ROS re-generation by photocatalysts.

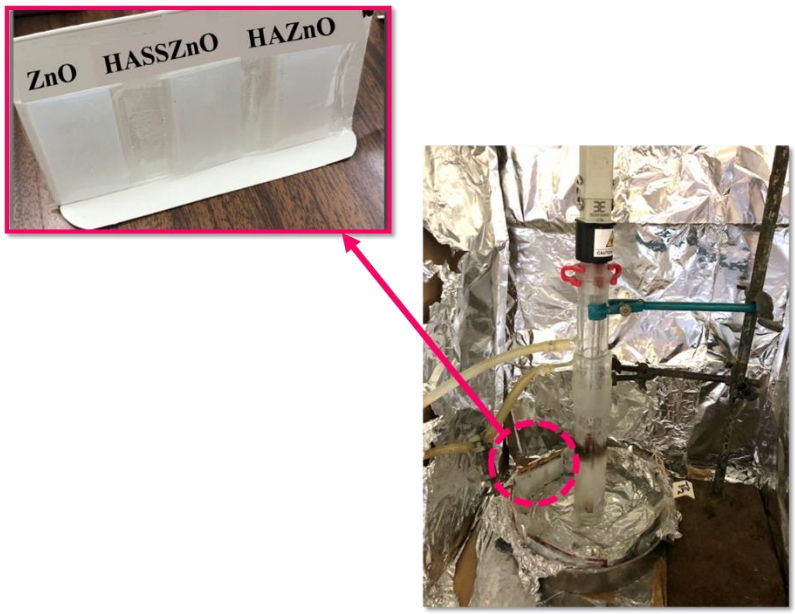

Figure 3.20. Photodegradation tests of LLDPE and PLA slices deposed on glass supports in a bath containing water and exposed to UVA lamp.

Blank tests of LLDPE and PLA slices in the absence of the catalyst but under irradiation were also performed under the following experimental conditions:

i) without UVA light and water exposure (bare);
ii) without UVA light exposure but in presence of water (wet dark);
iii) under UVA light exposure but without water (dry photolysis);
iv) with both UVA and water exposure (wet photolysis).

3.1.4.2 Photodegradation tests of PLA MPs under UVA and solar irradiation

Photodegradation tests on PLA samples were also performed adopting a different configuration, in which small PLA slices (5mm×5mm) where directly dipped in bi-distilled aqueous suspensions formed by 20 mg of ZnO and TiO_2 hybrid nanoparticles in 20 mL of water. These tests were carried out under both UVA and natural solar irradiation.

The experimental approach is schematized in Figure 3.21.

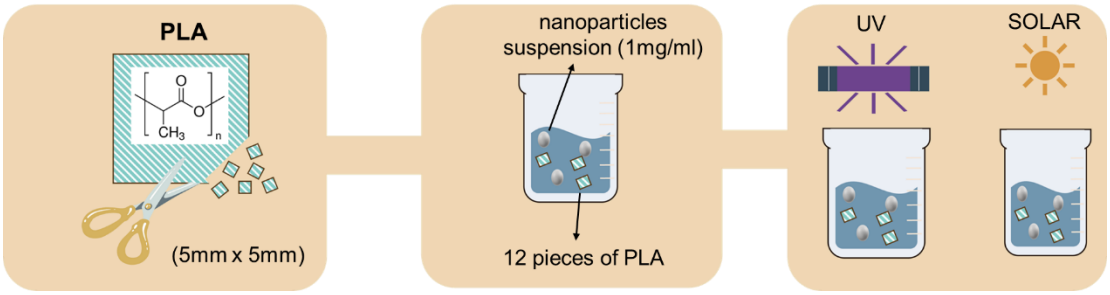

Figure 3.21. Schematic representation of PLA MPs photodegradation tests in presence of ZnO- and TiO_2-based nanoparticles.

To obtain easily comparable results, PLA photodegradation trend was analysed considering both time and accumulated energy per unit volume Q_{UV} [106]:

$$Q_{UV,n} = Q_{UV,n-1} + I * \frac{A}{V} * \Delta t \; ; \; \Delta t = t_n - t_{n-1} \tag{3.1}$$

where I = Irradiance [J·(h·cm^2)$^{-1}$], A = Irradiated surface [cm^2], V = Volume of reactor (or solution) [cm^3], Δt=time interval [h] and Q_{UV} = accumulated energy per unit volume [J·cm^{-3}][107].

To calculate Q_{UV} for samples exposed to UVA radiation, lamp irradiance was calculated considering the contribution of 305 nm, 313 nm and 366 nm wavelengths, since the

smaller bandgap was 3.18 eV (corresponding to a wavelength of 396 nm), while 404 nm and 435 nm gave no photocatalytic effect.

To calculate Q_{UV} for samples exposed to solar radiation, the irradiances obtained from the NASA website (https://power.larc.nasa.gov/data-access-viewer/) were used. In this case, the spectrum considered ranges from 300 nm to 3000 nm. Hence, to obtain the I values for the UV component of the solar spectrum, only the 4% of the total irradiance was considered [108].

The UV light-assisted photodegradation of PLA MPs by ZnO and HS/ZnO nanoparticles was investigated after 100 h (8168 $J \cdot cm^{-3}$), 200 h (16762 $J \cdot cm^{-3}$), 300 h (25015 $J \cdot cm^{-3}$) and 500 h (42543 $J \cdot cm^{-3}$), while by TiO_2 and HS/TiO_2 nanoparticles it was investigated after 100 h (8508 $J \cdot cm^{-3}$), 225 h (19314 $J \cdot cm^{-3}$), 350 h (30120 $J \cdot cm^{-3}$) and 500 h (42543 $J \cdot cm^{-3}$).

The solar-assisted photodegradation trends for all considered samples were investigated after 120 h (817 $J \cdot cm^{-3}$), 250 h (1574 $J \cdot cm^{-3}$) and 340 h (2116 $J \cdot cm^{-3}$).

3.1.5 Physicochemical characterization of polymer samples before and after photocatalytic treatment

The morphological, chemical, and structural modifications as well as changes in the thermal properties of LLDPE and PLA occurring during the photocatalytic processes in the presence of the prepared photocatalysts were investigated by means of SEM, ATR-FTIR, XRD, DSC, TGA and (Evolved Gas Analysis) EGA analyses.

3.1.5.1 Physicochemical characterization of LLDPE and PLA slices treated with HAs-doped/ZnO nanoparticles

SEM micrographs allow to observe the effects of the photodegradation process on the surface morphology of LLDPE slices after photocatalytic tests in the presence of bare and doped nanoparticles (Figure 3.22b-d). No significant morphological changes were appreciated after 75 h (data not shown), while significant changes were observed after 225 h depending on the nature of nanoparticles photocatalysts.

It is possible to observe that the surface of LLDPE after 225 h of photocatalysis treated with ZnO nanoparticles appeared uniform and smooth with no relevant degradation morphological effects (Figure 3.22b) with a surface roughness close to that exhibited by neat LLDPE (Figure 3.22a). Otherwise, after 225 h of UVA light exposure with HASS-doped/ZnO nanoparticles, degradation phenomena were visible: some spots and cracks appeared on LLDPE slice surface (Figure 3.22c); at the same time, after 225 h of UVA light exposure with HA-doped/ZnO nanoparticles, small holes appeared on the surface of LLDPE (Figure 3.22d). These results suggest a much more efficient photodegradation induced by doped catalysts than by bare ZnO, due to the enhanced ROS-generating ability of HAs-doped nanoparticles, according to EPR spin-trapping results.

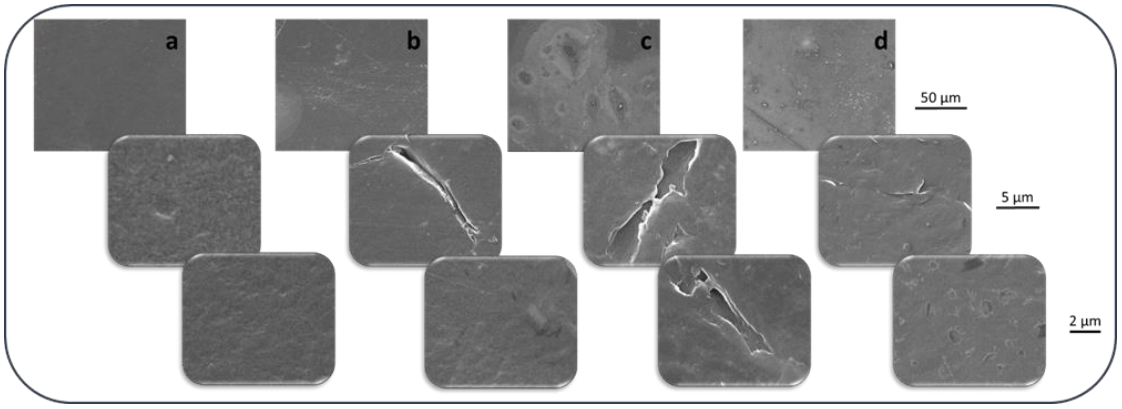

Figure 3.22. SEM micrographs of LLDPE before (a) and after irradiation for 225 h in the presence of ZnO (b); HASS-doped/ZnO (c); HA-doped/ZnO (d).

These species resulted very unstable and, going through the formation of hydrogen peroxide, can be finally changed into •OH radical species. In hybrid HAs-doped/ZnO nanoparticles, the conjugation of the inorganic component with the organic ones (already containing free-electrons) favoured the formation of •OH radical species that play a key role in the oxidation processes [109].

To monitor the chemical changes on LLDPE slice surfaces, ATR-FTIR spectra (Figures 3.23a,b) were recorded before and after UVA treatment.

Unexposed bare LLDPE slices show the following characteristics IR bands at: 2920-2850 cm^{-1} (ν_{C-H}), 1480-1430 cm^{-1} (δ_{CH2}) and (δ_{CH3}), and 710 cm^{-1} (ρ_{CH2}). The ATR-FTIR spectra of LLDPE under photolysis (Figure 3.24) do not show any significant change.

ATR-FTIR spectra of LLDPE slices after UVA treatment still show the above-described typical bands together with the appearance of new significant IR bands:
i) a broad band in the range 3550-3200 cm^{-1} (ν_{OH}), due to hydrogen-bonded products, such as hydroperoxides or alcohols; *ii)* a band in the range 1700-1500 cm^{-1} ($\nu_{C=O}$); *iii)* two bands in the ranges [1260-1240 cm^{-1}] and [1100-1040 cm^{-1}] (ν_{C-O}) related to ether-type linkages or alcohols or esters, and *iv)* a small band in the range 880-910 cm^{-1}, corresponding to vinyl group vibrations. The appearance of these new bands as well as the changes in their relative intensities can be considered a hallmark of LLDPE photo-oxidation [110–112].

After 75 h of irradiation, the relative intensity of the new bands is enhanced for both hybrid nanoparticles with respect to those observed in the case of bare ZnO (Figure 3.23a). On the contrary, after 225 h of irradiation, the relative intensity of the new bands of ZnO becomes similar to those of hybrid nanoparticles (Figure 3.23b).

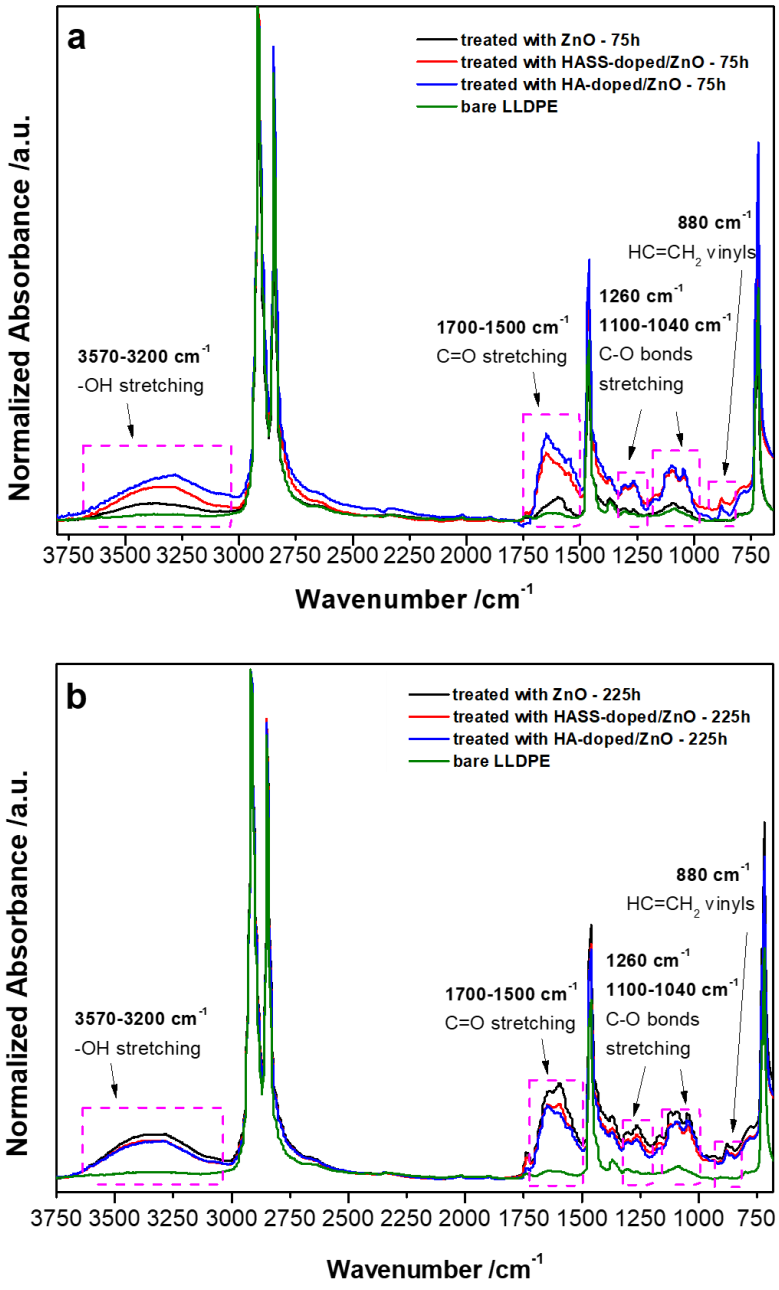

Figure 3.23. ATR-FTIR spectra of LLDPE slices treated with bare ZnO, HASS-doped/ZnO and HA-doped/ZnO nanoparticles after 75 h (a) and 225 h (b) of the exposure to UVA light irradiation.

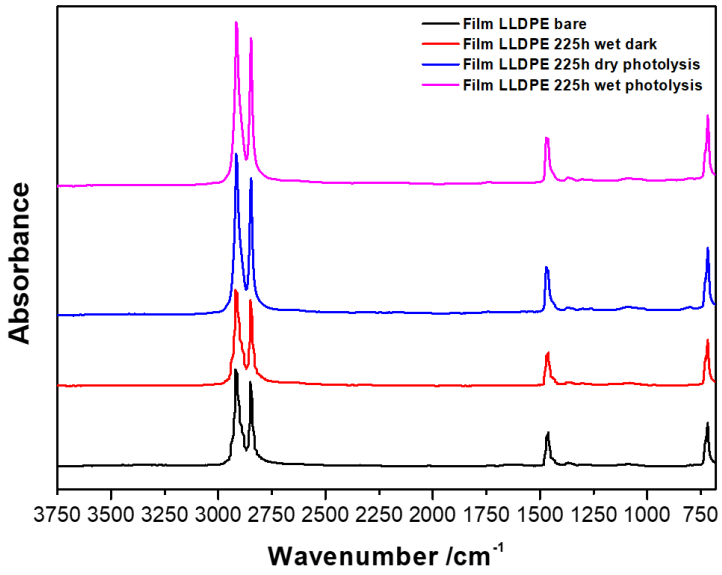

Figure 3.24. ATR spectra of LLDPE slices: bare, 225 h wet dark, 225 h dry photolysis and 225 h wet photolysis.

To estimate the degree of photo-oxidation in LLDPE slices, carbonyl and vinyl indexes (C.I. and V.I.) were determined (Table 3.3).

The C.I. and V.I. were calculated as ratio between the absorbance of carbonyl groups around 1710 cm^{-1} or, alternatively, of vinyl groups around 880 cm^{-1} and the absorbance of the internal reference peak of CH_2 at 1480 cm^{-1} [110]:

$$\text{Carbonyl Index (C.I.)} = \frac{\text{Abs1710}}{\text{Abs1480}} \tag{3.2}$$

$$\text{Vinyl Index (V.I.)} = \frac{\text{Abs880}}{\text{Abs1480}} \tag{3.3}$$

After 75 hours of irradiation, the C.I. value markedly increased in the presence of both doped nanoparticles with a similar rate (~0.25) compared to bare ZnO (~0.10). Then, after 225 h, only a slight increase of C.I. was observed in the presence of doped nanoparticles (~0.05), while a significant growth of C.I. (~0.14) was detected in the presence of bare ZnO, similarly to HAs-doped/ZnO photocatalysts, in agreement with the trend of the relative intensities previously observed.

Table 3.3. Values of carbonyl and vinyl indexes determined from ATR-FTIR spectra of LLDPE before and after UVA irradiation, in the presence of bare ZnO or HASS-doped/ZnO and HA-doped/ZnO nanoparticles.

Sample	Carbonyl Index, C.I. (± 0.03)		Vinyl Index, V.I. (± 0.03)	
	after 75h	***after 225h***	***after 75h***	***after 225h***
Bare LLDPE	0.04		0.01	
LLDPE treated with ZnO	0.14	0.28	0.02	0.12
LLDPE treated with HASS-doped/ZnO	0.28	0.35	0.09	0.13
LLDPE treated with HA-doped/ZnO	0.30	0.33	0.06	0.12

These results agree with the recent evidences on photodegradation of LLDPE [113] and PP films in the presence of ZnO nanoparticles [69], for which the formation of the initial oxidation products were described as preferentially due to Norrish type I mechanism [69,113,114]. The mechanism describes the homolytic cleavage of C-C bonds belonging to aldehydes and ketones (primarily formed through the ROS attack on the polymeric chain) into two free radical intermediates. This leads to chain scission and formation of unstable radicals, such as hydroxy peroxides, that might continue the photooxidation process, directly decomposing into various carbonyl/hydroxyl products [115].

Based on the above results, in the first stages of the photodegradation process (75 h) the surface modification of the external layer of LLDPE started to occur. In the subsequent stages (225 h) this phenomenon was enhanced giving the formation of grooves and cracks as observed in SEM images displayed in Figure 3.22.

XRD analysis was performed to detect the possible changes of the crystallinity degree of LLDPE occurred after the UVA treatment. The XRD profile of LLDPE was characterized by peaks at 21.5°, 23.8° and 36.3° of 2θ, corresponding to (110), (200) and (002) reflections of the orthorhombic form of polyethylene, respectively [116] (Figure 3.25). After 75 h irradiation (Figure 3.25a**)**, a shift at higher angles of the above peaks is seen, that was enhanced for HASS-doped/ZnO (2θ = 0.24°) and HA-doped/ZnO (2θ = 0.19°) nanoparticles than bare ZnO (2θ = 0.10°). According to [116], these results can be due to a change of the size of the crystalline cell, probably caused by the expulsion of the chain parts containing the side-groups. After 225 h irradiation (Figure 3.25b**)**, any significant changes were observed.

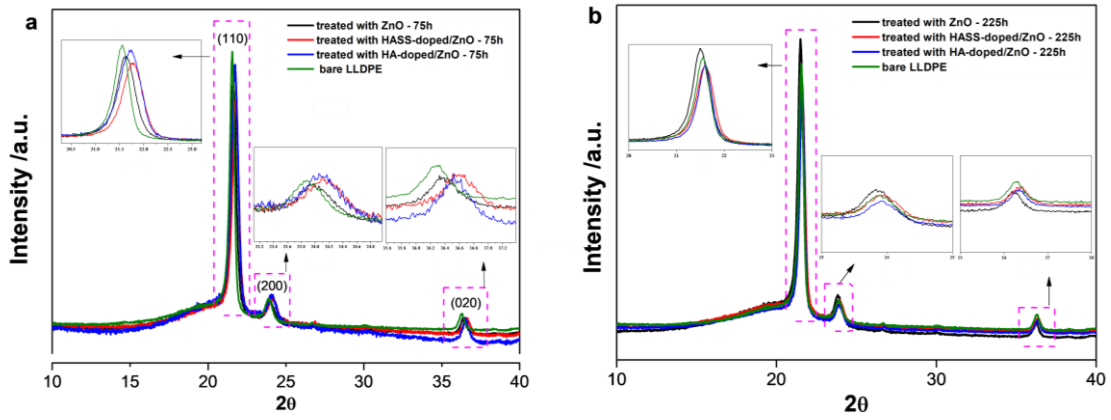

Figure 3.25. XRD spectra of LLDPE exposed to UVA light irradiation for 75 h (a) and 225 h (b) in the presence of bare ZnO, HASS-doped/ZnO and HA-doped/ZnO nanoparticles.

The changes induced by the photodegradation process in the presence of ZnO doped nanoparticles were confirmed by estimating the crystallinity index, X_c, from XRD patterns, as described in Section 5.

As reported in Table 3.4, a slight decrease (~2%) in the crystallinity degree of LLDPE slices was detected after the photocatalytic treatment in the presence of all catalysts. This trend does not agree with some previous evidences for PE films which proposed an X_c increase related to a local reorganization of the mobile small chain fragments formed by chain scission reaction induced by the photo-oxidation [110]. The small decrease of X_c

should be related to the presence of defects in the crystalline structure or chemical impurities within the polymer [117] due to the progress of the photo-oxidation process.

Table 3.4. Values of crystalline index, X_c, of LLDPE before and after UVA light irradiation, in the presence of bare ZnO or HASS-doped/ZnO and HA-doped/ZnO nanoparticles.

LLDPE samples	Crystallinity Index, X_c (err $\leq$ 2%)	
	75h	***225h***
bare	42.1 %	
treated with ZnO	41.5 %	42.4 %
treated with HASS-doped/ZnO	40.8 %	40.1 %
treated with HA-doped/ZnO	39.8 %	40.3 %

The effect of photocatalytic process on the thermal properties of LLDPE slices was also analysed. As shown in Figure 3.26, the weight loss of LLDPE occurs in one step, from 350 to about 550 °C, due to the degradation of C–C bonds in the main LLDPE backbone. The Gram-Schmidt plot, overlaid to the TG curve, confirms the occurrence of one degradation process at 482°C, corresponding to maximum weigh loss rate of LLDPE. FTIR spectrum of volatile substance released by LLDPE at this temperature was characterised by absorption bands due to symmetric C–H stretching vibration ($\nu_{C\text{-}H}$) of CH_2 (2885 – 2801 cm^{-1}) and CH_3 (2990 – 2945 cm^{-1}) [118]. After 225 h of photo-exposition in the presence of bare ZnO, the temperature of the maximum weigh loss rate of LLDPE was shifted to lower value (477 °C, corresponding to ΔT=5 °C), while TG profile was not significantly influenced by the exposure to HAs-doped/ZnO catalysts. No variation in the spectra of the degradation products at the temperature of the maximum weigh loss rate of samples was observed.

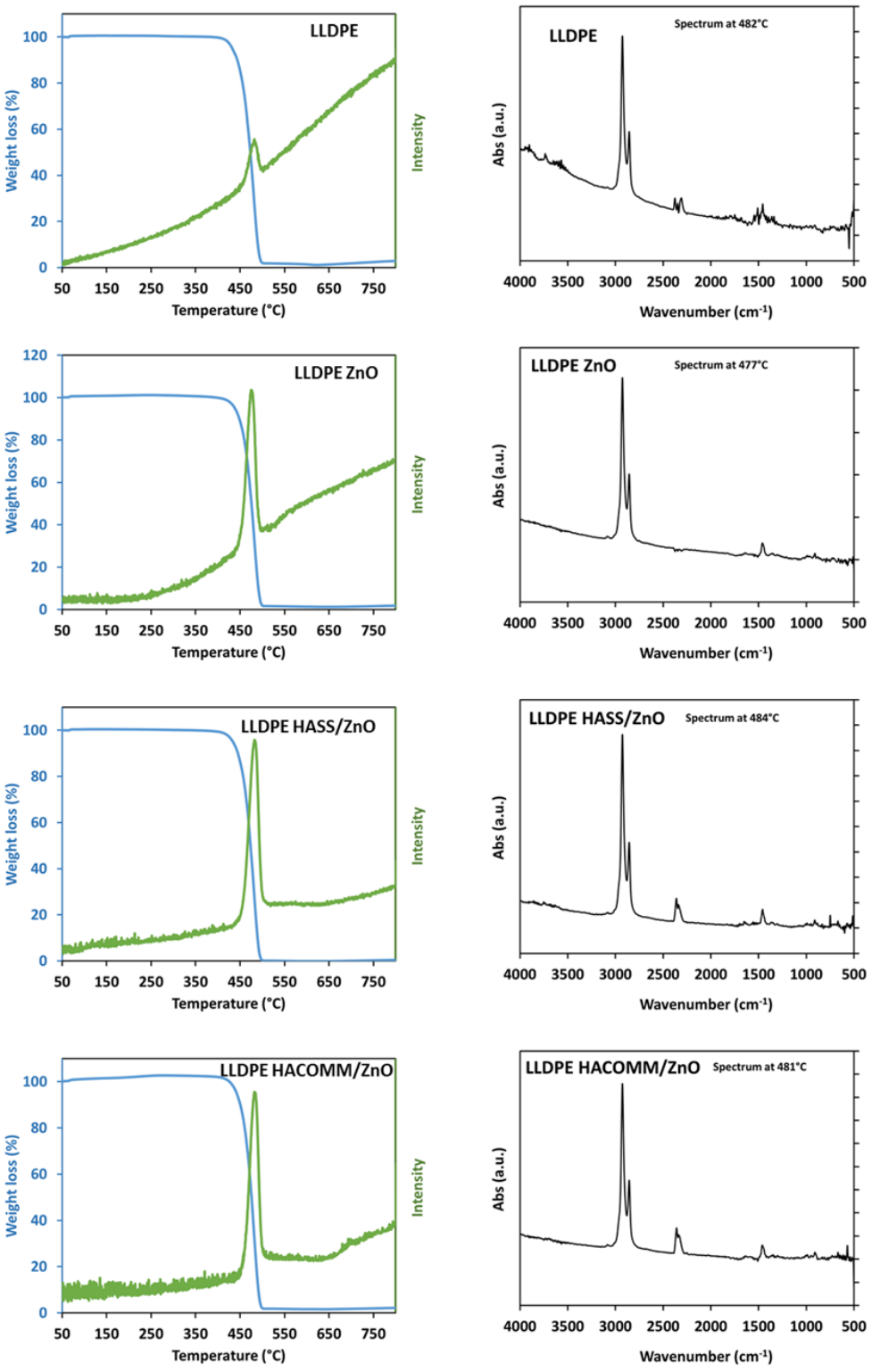

Figure 3.26. TG curves overlaid with the Gram-Schmidt plot and FTIR spectrum acquired on the volatile substance released at the temperature of the maximum degradation rate of LLDPE samples exposed to bare ZnO, HASS-doped/ZnO and HA-doped/ZnO catalysts after 225h.

On the other hand, a slight decrease (~2 °C) in the melting temperature (T_m) of LLDPE was observed after 225 h of UVA light exposure independently by the catalyst type used as photocatalyst (Figure 3.27a). The slight decrease of T_m observed in aged LLDPE samples could result from the increase in crystal defects occurring during photo-oxidation [117]. Instead, the crystallinity index X_c remained nearly constant after 75 h of irradiation whereas it underwent very slight changes after 225 h (~1-1.5%), confirming that the main effect of the photo-oxidation predominantly involved the polyethylene chains scission in the amorphous regions (Figure 3.27b).

Although the values appeared slightly lower than those estimated by XRD, the trends are fairly confirmed and agree with the previous ATR-FTIR and SEM analyses, indicating that the photo-oxidation in the presence of the photoactive nanoparticles mainly involved the surface of slices, generating local alterations that would be weak points for a further photodegradative action for longer times.

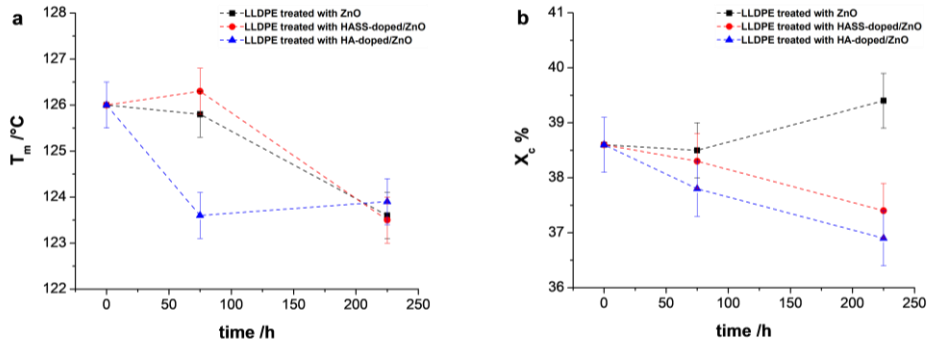

Figure 3.27. Thermal parameters of LLDPE slices as a function of the irradiation time: (a) melting temperature T_m (°C) and (b) crystallinity index X_c (%).

Then the photocatalytic degradation of PLA slices exposed to bare and ZnO doped nanoparticles was evaluated.

Likewise observed for LLDPE, the more evident morphological changes occurred after 225 h of UVA exposure, as shown by the analysis of SEM images displayed in Figure 3.28.

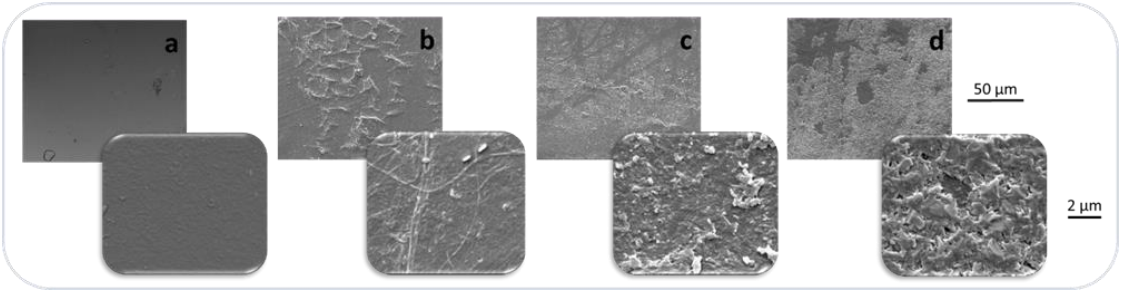

Figure 3.28. SEM micrographs of PLA slices before (a) and after 225 h of irradiation: in the presence of bare ZnO (b), HASS-doped/ZnO (c) and HA-doped/ZnO (d) nanoparticles.

ATR-FTIR spectra of PLA slices after 225 h of UV irradiation in wet dark, dry and wet photolysis do not show significant changes with respect to the spectrum of bare PLA (Figure 3.29).

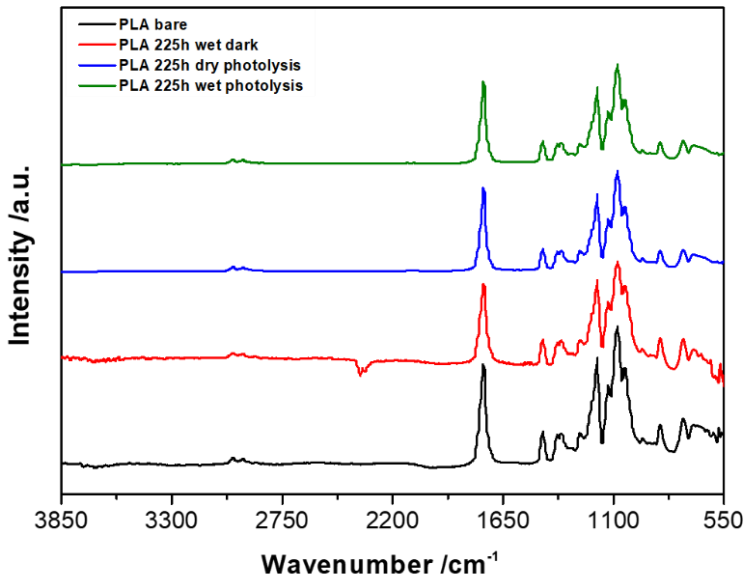

Figure 3.29. ATR spectra of PLA slices: bare, 225 h wet dark, 225 h dry photolysis and 225 h wet photolysis.

Figure 3.30 shows ATR-FTIR spectra of PLA before and after the photocatalytic treatment. The main typical bands of PLA are observed at: 1752 cm^{-1} ($\nu_{C=O}$), 1190 cm^{-1} ($\nu_{as\ C-O-C}$), and 1093 cm^{-1} ($\nu_{s\ C-O-C}$) [119]. Other absorption bands are seen at: 2997 cm^{-1} ($\nu_{as\ C-H}$), 2946 cm^{-1} ($\nu_{s\ C-H}$), 1456 cm^{-1} ($\delta_{as\ C-H}$), at 1382 cm^{-1} ($\delta_{s\ C-H}$), and 868 cm^{-1} (ν_{C-C}) [119].

The samples photo-exposed 75 h do not show significant changes with respect to bare PLA (Figure 3.30a), while marked changes are seen in the samples photo-exposed 225 h (Figure 3.30b). The photocatalytic process induced the formation of a broad absorption band in the hydroxyl region (3500-3300 cm^{-1}), corresponding to products such as hydroperoxides or alcohols, the decrease of the relative intensity of C=O band at 1752 cm^{-1} and the increase of the relative intensity of the bands at 1456 cm^{-1} ($\delta_{as\ C-H}$) and 1382 cm^{-1} ($\delta_{s\ C-H}$).

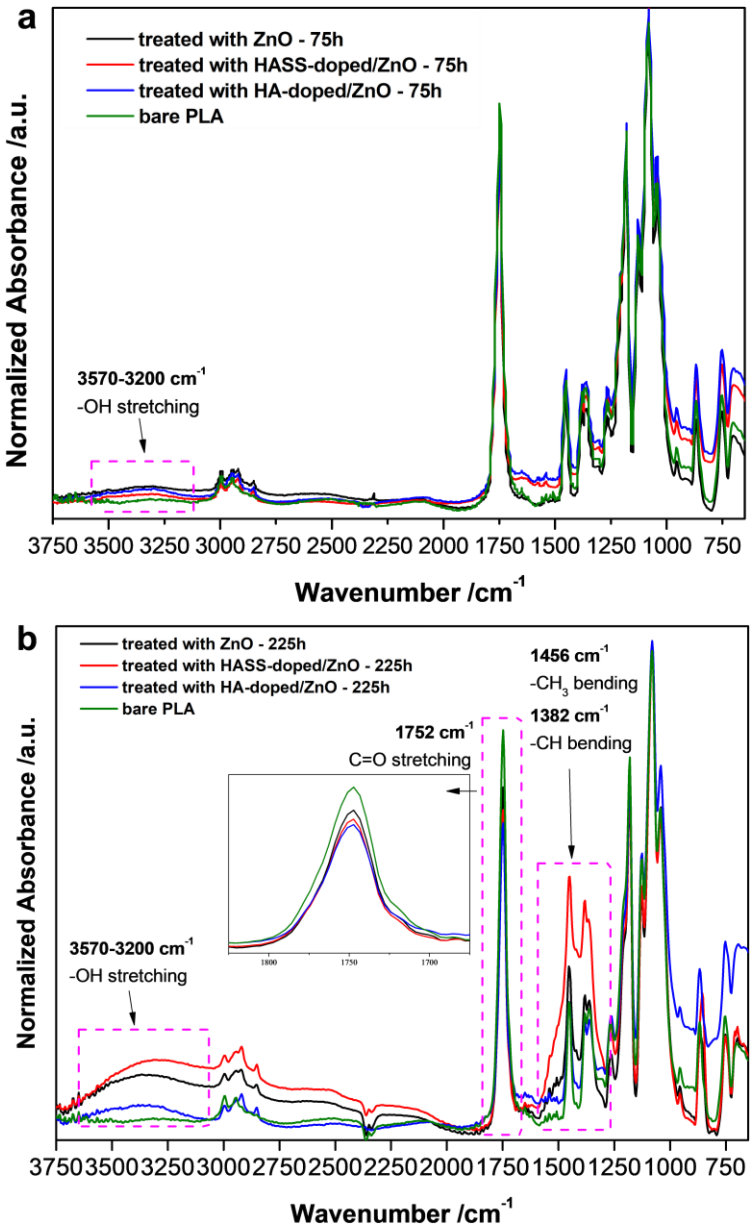

Figure 3.30. ATR-FTIR spectra of PLA treated with ZnO, HASS-doped/ZnO and HA-doped/ZnO nanoparticles, after 75 h (a) and 225 h (b) of the exposure to UVA lamp.

Carbonyl index (C.I.) was also evaluated as ratio between the absorbance of carbonyl groups around 1752 cm^{-1} and that of the internal reference peak at 1079 cm^{-1}. It was found that the greatest change occurred in the case of HA-doped/ZnO (0.64), then HASS-doped/ZnO (0.68) and finally bare ZnO (0.72) with respect to bare PLA slices (0.84).

The oxidation of PLA is proposed to occur via a Norrish type II mechanism, which involves the joint action of an oxidant and photochemical attack on the polymer [119,120].

XRD analysis was also performed to monitor the possible changes in the crystallization of PLA during photo-exposure. XRD patterns of the photo-exposed PLA slices (see Figures 3.31a,b) do not show any significant change with respect to the pattern of bare PLA, that is characterized by broad bands at 2θ~17° and 2θ~32°, attesting its predominant amorphous character.

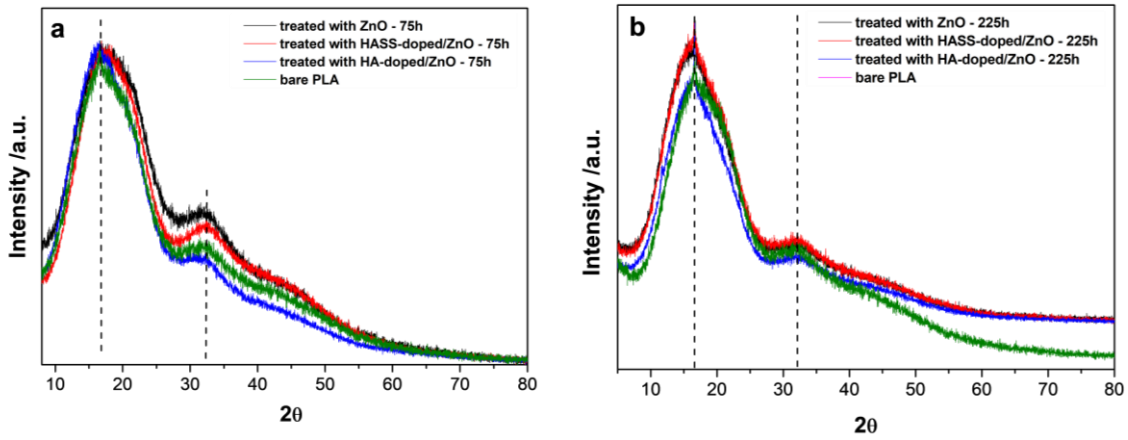

Figure 3.31. XRD spectra of PLA treated with ZnO, HASS-doped/ZnO and HA-doped/ZnO nanoparticles, after 75h (a) and 225 h (b) of exposure to UVA lamp.

The effect of photocatalytic process on the thermal properties of PLA slices was also analysed. Gram-Schmidt plots of evolved gases as a function of temperature and FTIR spectra of gases released at the maximum evolution rate temperature of PLA samples are reported in Figure 3.32. PLA exhibits only one weight loss step with onset at around 300 °C and the maximum rate decomposition temperature at 350 °C. At this temperature, FTIR spectrum shows an intense band in the carbonyl region, at 1790 cm^{-1}, a band at 3576 cm^{-1} (ν_{O-H}), bands in the 3005–2600 cm^{-1} region (ν_{C-H}), and bands at 1244 and 1106 cm^{-1} (ν_{C-O}). These bands suggest the formation of acetaldehyde and lactide monomer and carboxylic acids during degradation of PLA [121].

Photocatalytic oxidation of PLA slices exposed to bare and hybrid ZnO-based nanoparticles for 225 h induced a slight increase of temperature of the maximum degradation rate in the Gram-Schmidt plot (Figure 3.32).

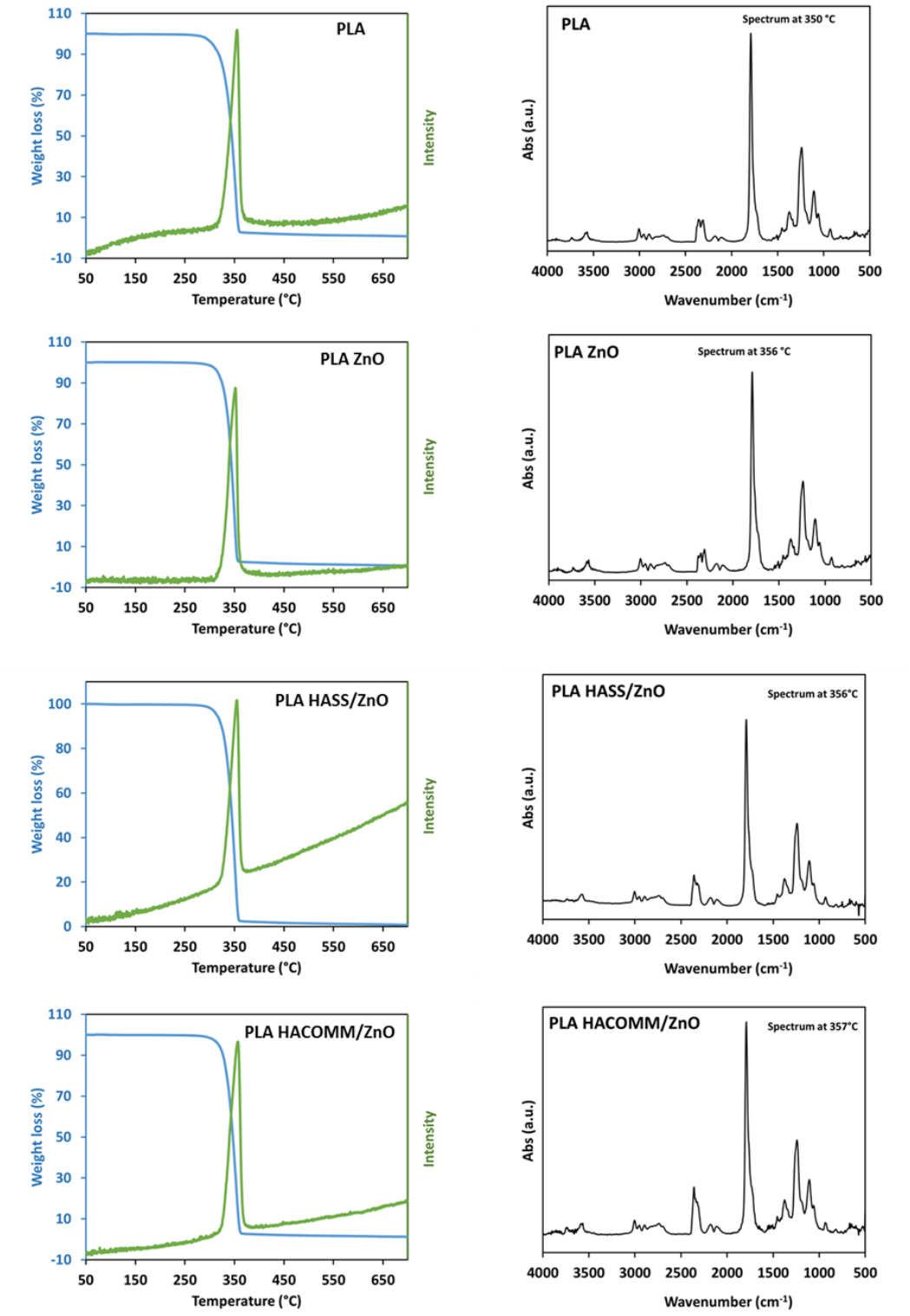

Figure 3.32. TG curves overlaid with the Gram-Schmidt plot and FTIR spectrum recorded on the volatile substance released at the temperature of the maximum degradation rate of PLA samples exposed to bare ZnO, HASS-doped/ZnO and HA-doped/ZnO catalysts after 225h.

DSC curves of PLA slices show an increase of glass transition temperature (T_g) and an endothermic peak associated with relaxation process in all the photo-aged samples (Figure 3.33).

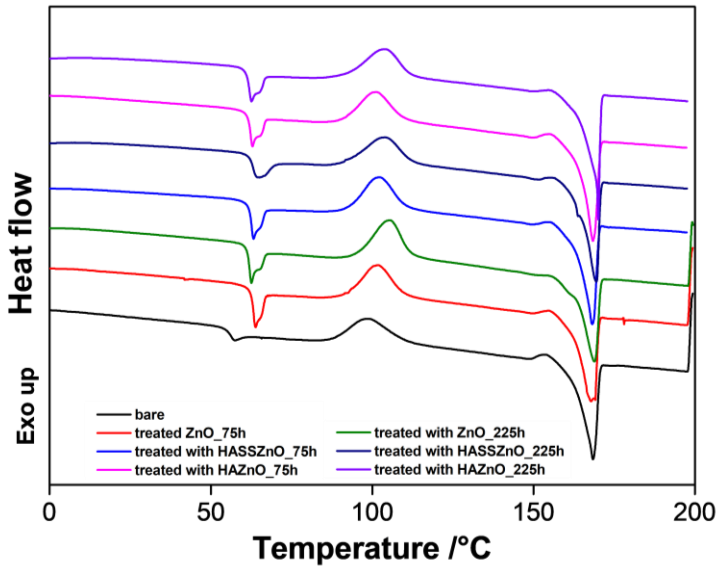

Figure 3.33. DSC thermograms of PLA slices.

It can be observed that the T_g of PLA samples increase from 56 °C to ~62 °C after 225 h of irradiation (Figure 3.34a**).** This behaviour should be determined by the PLA tendency to undergo physical aging at temperature values close to the ambient one [114,122]; this caused an increase in the T_g of the aged materials due to a reorganization of the amorphous chains [114,122].

On the other hand, cold crystallization temperature (T_c) progressively increased with irradiation (Figure 3.34b), and a greater increase was observed in the case of bare ZnO **(**DT_c ~ 6.1 °C) compared to HAs-doped/ZnO (DT_c ~ 4.7 °C).

As shown in Figure 3.34c, the crystallinity index (X_c) decreased after 75h of irradiation (~2-4 %), while it increased (~1.5-2 %) for more prolonged exposure times.

Indeed, PLA degradation started in the amorphous structures [123]. The polymer chains resulting from chain cleavage occurring during photodegradation were characterized by lower molecular weight and therefore a higher mobility to re-organize and create crystalline domains in the amorphous matrix [122], thus explaining the X_c increase observed after irradiation for 225 h.

Definitely, during the photocatalytic process in the presence of ZnO doped nanoparticles, PLA polymer underwent a chains rearrangement that induced a hindering of their mobility, thus determining the detected increase of the T_g and T_c values [122].

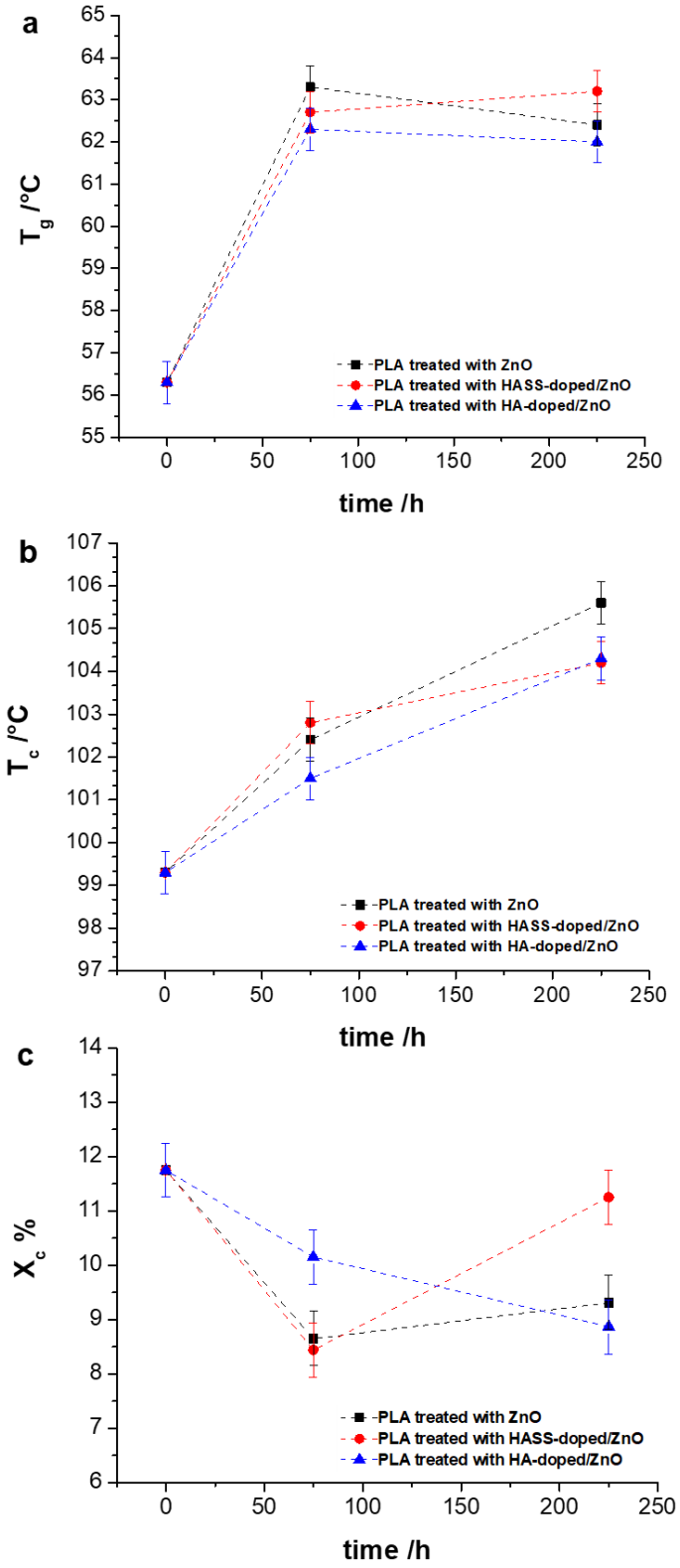

Figure 3.34. Trends of glass transition temperature T_g (°C) (a), cold crystallization temperature T_c (°C) (b) and crystallinity index X_c (%) (c) for PLA slices, in the presence of bare ZnO, HASS-doped/ZnO and HA-doped/ZnO nanoparticles.

3.1.5.2 Physicochemical characterization of PLA MPs treated with HS/ZnO and HS/TiO_2

SEM images of PLA MPs before (Figure 3.35A) and after the photocatalytic treatment with bare ZnO and TiO_2 (Figures 3.35B,E) and with HS/ZnO and HS/TiO_2 hybrid nanoparticles under UVA (Figures 3.35C,F) and solar radiation (Figures 3.35D,G) are reported.

PLA samples show slight degradation phenomena on their surface in the presence of bare TiO_2 and ZnO nanoparticles after 500 h of UVA light irradiation (Figures 3.35B and 3.35E). On the other hand, the exposure, in the same experimental conditions but with hybrid HS/TiO_2 and HS/ZnO nanoparticles, induced an enhancement of the degradation phenomena (Figures 3.35C and 3.35F).

Indeed, some grooves and cracks were recognized on MPs surface exposed to HS/ZnO nanoparticles (Figure 3.35F), while cracks and holes were detected on PLA surface exposed to HS/TiO_2 (Figure 3.35C), suggesting that MPs photodegradation occurred in both cases. Specifically, it resulted more pronounced in the case of HS/ZnO and HS/TiO_2 nanoparticles than bare ZnO and TiO_2 ones.

This behavior could be correlated to the conjugation of inorganic semiconductors to humic substances, already containing free-electrons, that enables an improved production of ROS species by hybrid HS/TiO_2 and HS/ZnO photocatalysts [86]. Undoubtedly, hydroxyl radicals and photogenerated holes are the main oxidants that attacked PLA microfilms leading to their degradation [109].

The solar exposures of PLA MPs treated with HS/TiO_2 and HS/ZnO nanoparticles resulted in a very pronounced degradation of the surface after 340 h (2116 $J \cdot cm^{-3}$) of irradiation, as evidenced by the eroded areas reported in Figures 3.35D,G.

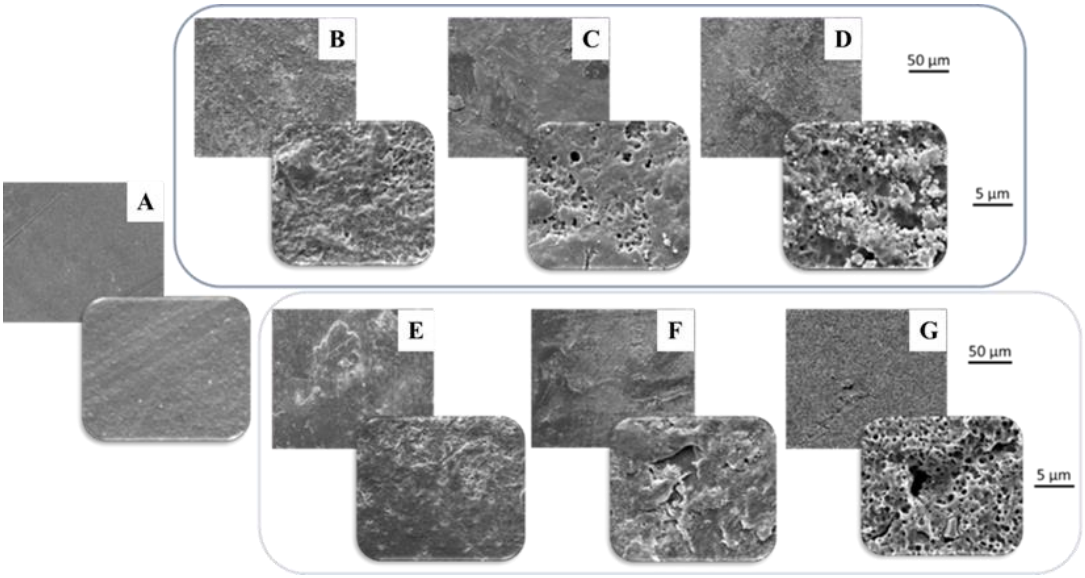

Figure 3.35. SEM micrographs of bare PLA (A) and photodegraded PLA MPs in the presence of (B) bare TiO_2 under UVA light for 500 h, (C) HS/TiO_2 under UVA light for 500 h, (D) HS/TiO_2 under solar light for 340 h, (E) ZnO under UVA light for 500 h; (F) HS/ZnO under UVA light for 500 h, (G) HS/ZnO under solar light for 340 h.

ATR-FTIR spectra of PLA MPs were acquired before and after the UVA/solar light exposure to investigate the chemical changes on film surfaces.

The ATR analyses were carried out after 100 h (8508 J·cm^{-3}), 225 h (19314 J·cm^{-3}), 350 h (30120 J·cm^{-3}) and 500 h (42543 J·cm^{-3}) of treatment in the presence of TiO_2 and HS/TiO_2 nanoparticles, and after 100 h (8168 J·cm^{-3}), 200 h (16762 J·cm^{-3}), 300 h (25015 J·cm^{-3}) and 500 h (42543 J·cm^{-3}) in the presence of ZnO and HS/ZnO ones.

As observed in our previous work [80] and discussed in Section 3.1.5.1, PLA slices in the absence of the catalyst but under UVA irradiation did not show any change.

Figures 3.36A-D compare the ATR-FTIR spectra of PLA MPs treated with HS/TiO_2, HS/ZnO, TiO_2 and ZnO nanoparticles.

ATR spectra show absorption bands at: 1747 cm^{-1} ($\nu_{C=O}$), 1454-1360 cm^{-1} (-CH_3 deformation), 1265 cm^{-1} ($\delta_{C=O}$), 1182 cm^{-1} (ν_{C-O-C}), 1130-1088 cm^{-1} (ν_{C-O}), 1043-948 cm^{-1} (δ_{O-H}) and 867-752 cm^{-1} (ν_{C-C}). No shifts of the characteristic bands of PLA nor formation of new bands are observed, suggesting that any byproduct was formed on the surface of PLA samples. However, the intensity of the carbonyl peak at 1748 cm^{-1} progressively decreased during the treatment but its decrease appears more marked in the case of hybrid (Figure 3.36A,B) than of bare nanoparticles (Figure 3.36C,D). Moreover, as shown in Figure 3.36B, after 300 h (25015 $J \cdot cm^{-3}$) and 500 h (42543 $J \cdot cm^{-3}$), the formation of a new band in the range 1550-1480 cm^{-1} (ν_{O-C-O}) can be also observed.

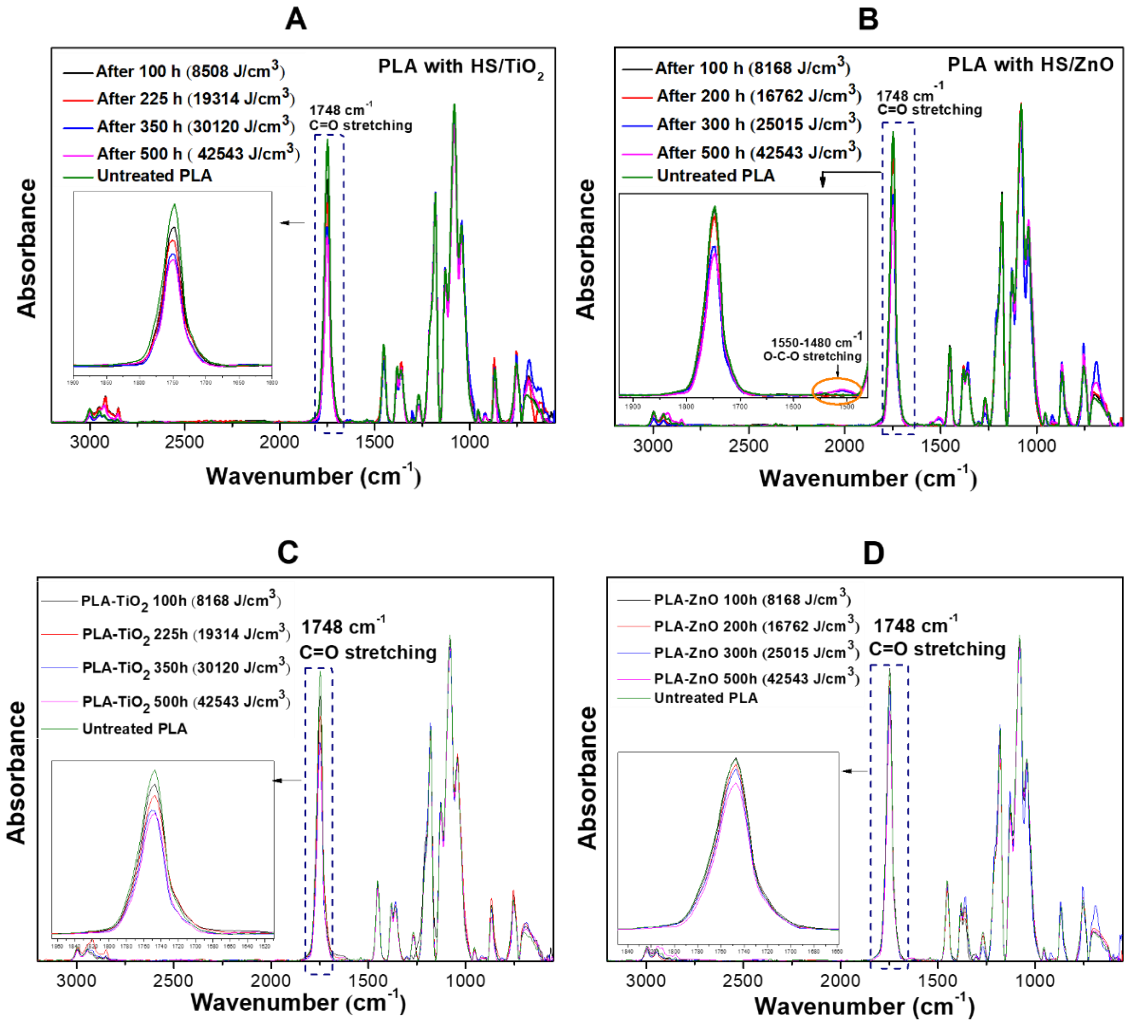

Figure 3.36. ATR-FTIR spectra of PLA photodegradation trend using HS/TiO_2 (A), HS/ZnO (B), TiO_2 (C) and ZnO (D) under UVA light.

Since the intensity of the carbonyl peak at 1748 cm^{-1} decreased, C.I. values for each investigated treatment time were estimated as described in Equation 3.4 [124]:

$$C.I. = \frac{Area\ under\ the\ peak\ (1748\ cm^{-1})}{Area\ under\ the\ peak\ of\ reference\ (1130\ cm^{-1})} \quad (3.4)$$

Figures 3.37A,B show C.I. values plotted against Q_{UV} and time. Both hybrid HS/TiO_2 and HS/ZnO nanoparticles were able to promote MPs degradation more effectively (i.e. decreasing the C.I. more markedly) than bare ones. The higher photodegradation behaviour of hybrid nanoparticles than bare ones could be related to the presence of HS conjugated with metal oxides that boosted the ROS-generating ability of semiconductor photocatalysts.

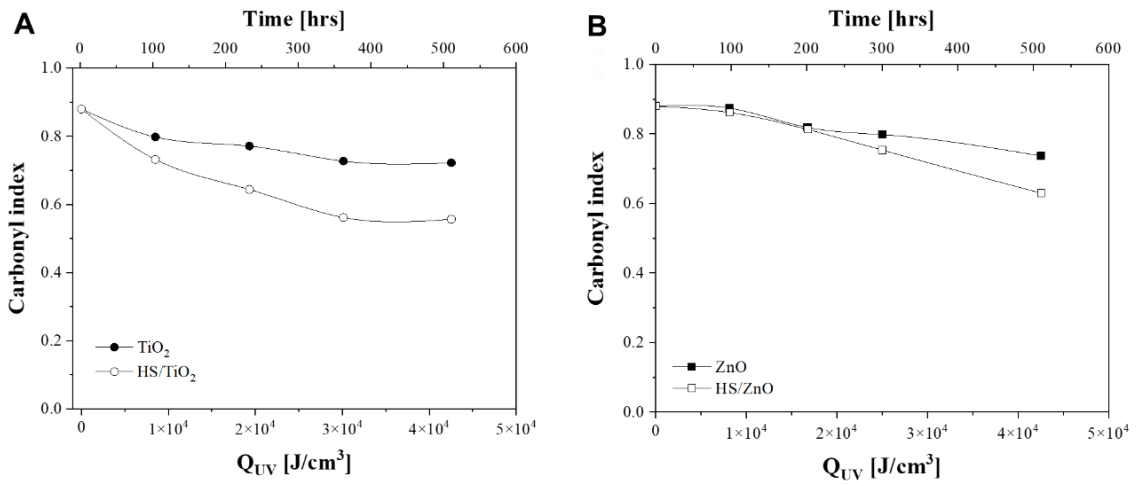

Figure 3.37. Comparison between C.I. values estimated for PLA MPs exposed under UVA light to bare TiO_2 and hybrid HS/TiO_2 (A) and to bare ZnO and HS/ZnO nanoparticles (B).

Similar results were obtained in the case of the solar photocatalytic process (Figures 3.38A-D and 3.39A,B), confirming the higher performances of hybrid HS/ZnO and HS/TiO_2 nanoparticles than those of bare ones.

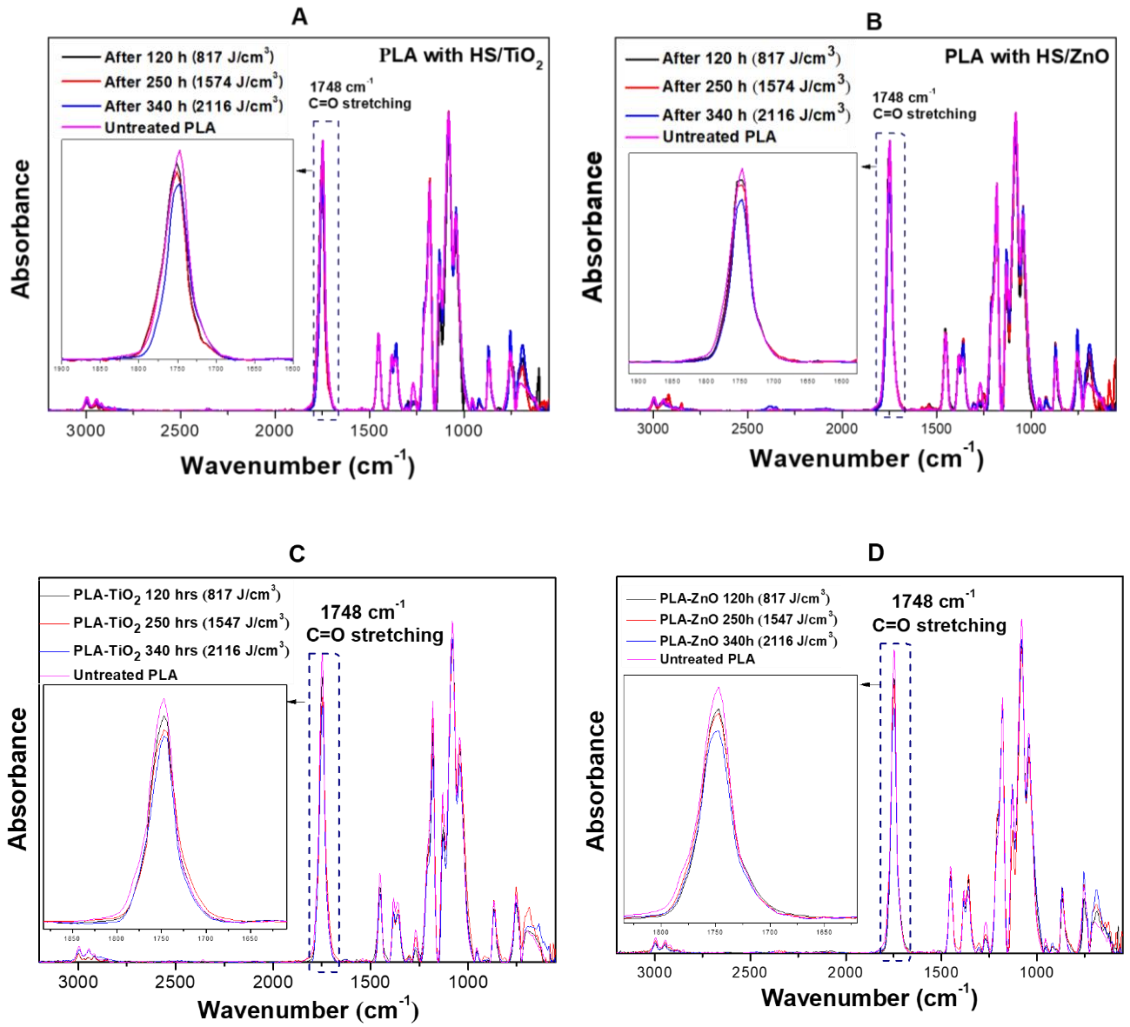

Figure 3.38. ATR-FTIR spectra of PLA photodegradation trend using HS/TiO_2 (A), HS/ZnO (B), TiO_2 (C) and ZnO (D) under solar light.

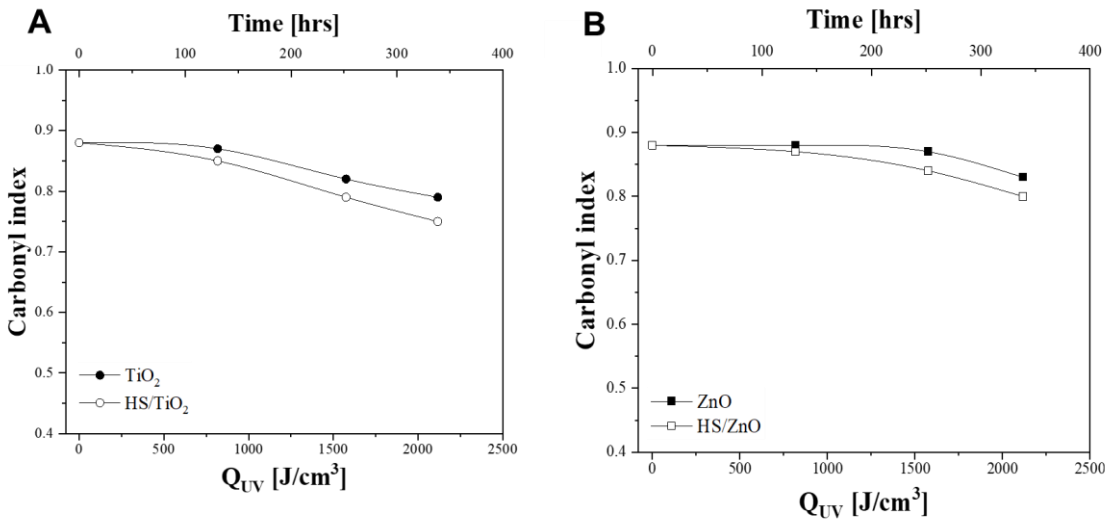

Figure 3.39. Comparison between C.I. values estimated for PLA microplastic samples exposed under solar light to bare TiO_2 and hybrid HS/TiO_2 (A) and to bare ZnO and HS/ZnO (B).

To investigate the effect of photocatalytic oxidation on thermal transitions of PLA samples, DSC analysis from 0 to 200 °C was performed. As a result, the glass transition temperature (T_g), cold-crystallization temperature and enthalpy (T_c, ΔH_c) and melting temperature and enthalpy (T_m, ΔH_m) of PLA samples are reported in Table 3.5.

T_g values of PLA after photodegradation were higher than that of bare PLA (56.8 °C). Exposure of PLA MPs to ZnO- and TiO_2-based nanoparticles induced a shift of T_g to higher temperature due to a reorganization of the amorphous chains caused by the degradation.

Moreover, cold crystallization, not detectable in neat PLA, was present in all the photodegraded samples. The photodegradation of PLA enhanced by ZnO- and TiO_2-based nanoparticles promoted the appearance of a cold crystallization peak because of the improvement of chain diffusion at temperatures above T_g [125].
PLA samples exposed to HS/TiO_2 for 500 h show a T_c value lower (89.4 °C) than that of PLA samples exposed to HS/ZnO for 500 h (96.9 °C). These data suggest that the photocatalyst type slightly influenced the chain diffusion process during cold crystallization.

Photodegradation also affected the melting of PLA MPs samples, leading to double melting transition in PLA photodegraded samples (except in the PLA exposed to HS/ZnO for 500 h). The multiple melting behavior of PLA can be ascribed to different thermal stability of the crystal modifications, and the possible interconversion among the various crystal forms. The presence of double melting is consistent with crystal re-structuring occurring during photodegradation [126].

Then, the photodegradation process caused changes in the crystalline content of PLA. An increase of PLA X_c was induced by the exposure to all nanoparticles (except in PLA exposed to HS/ZnO for 500 h). The increase of X_c can be explained because the amorphous regions are more susceptible to degradation than the crystalline ones and the resulting shorter polymer chains show a suitable mobility to re-organize and create crystalline domains in the amorphous matrix [80].

Table 3.5. Thermal transitions of bare and photodegraded PLA samples.

Sample	T_g (°C)	T_c (°C)	ΔH_c (J/g)	T_{m1} (°C)	T_{m2} (°C)	ΔH_m (J/g)	X_c (%)
Untreated PLA	56.8			165.9		12.24	0.13
PLA_TiO₂ 500 h	63.9	91.1	17.1	167.3	173.1	57.6	0.43
PLA_HS/TiO₂ 500 h	64.9	89.4	17.9	166.7	173.4	60.0	0.45
PLA_HS/TiO₂ 340 h solar	63.2	92.6	27.9	168.1	173.3	58.1	0.32
PLA_ZnO 500 h	64.1	95.7	25.9	169.5	173.5	53.9	0.30
PLA_HS/ZnO 500 h	65.9	96.9	39.7	167.8		50.2	0.11
PLA_HS/ZnO 340 h solar	62.0	90.2	8.7	167.9	173.2	72.3	0.68

3.2 Indirect daylight oxidative degradation of LLDPE and PET MPs by a bio-waste modified TiO_2-based material

An innovative strategy of pollutants degradation was recently proposed by our research groups in which ROS were generated on the surface of inorganic-organic hybrid gel-derived materials under indirect daylight at room temperature, without the need for external energy sources [41,42]. This process is driven by Ligand-to-Metal Charge Transfer (LMCT) complexes occurring between suitable organic molecules and titanium or zirconium [127–129].

Based on this expertise, an innovative oxidative approach for treating MPs, which avoids direct energy inputs (irradiation or heat), is here proposed.

By designing a hybrid material coupling titanium oxide and bio-waste (rosin), the degradation of LLDPE MPs under mild conditions is successfully achieved [130]. This approach offers a promising cost-effective strategy and sustainable method for MPs remediation, potentially contributing to circular waste management solutions.

3.2.1 Sol-gel synthesis

The sol-gel method is a versatile wet chemical route to produce amorphous and crystalline solid materials in different shapes, i.e. film, bulk and powder, using low processing temperature. With respect to the solid state and other wet syntheses, it allows to control:

- the homogeneity, purity and composition of the final material up to the molecular scale;
- the particle size and morphology by means the addition of templates, structure-directing agents or dopants.

The method involves the transition from a sol to a solid gel phase. A sol is a colloidal suspension of particles in the range of 1-1000 nm, while a gel can be defined as a continuous solid skeleton enclosing a continuous liquid phase or as an interconnected, non-fluid three-dimensional network that extends through a fluid phase.

Sol-gel synthesis process allows modulating the microstructure, morphological and textural properties of the final materials by means of the processing parameters (i.e. precursor concentration, water/metal molar ratio, temperature, pH of the reaction medium).

In the hydrolytic sol-gel method, the sol-gel transition involves two key steps: hydrolysis and polycondensation. Generally, hydrolysis is started by the addition of small amounts of water. When the precursors are insoluble in water, non-aqueous solvents such as alcohols are added to the reaction medium to form a homogeneous solution.

3.2.2 Synthesis of T-*Abi* for the indirect daylight oxidative degradation of LLDPE and PET MPs

3.2.2.1 Materials

Titanium (IV) n-butoxide (Ti(OBu)4, 97+%) and ethanol (EtOH, 99.8+%) were provided by Sigma-Aldrich (Milan, Italy).

Commercial rosin was used as bio-waste.

Flexirene FG 20 F, a linear low-density polyethylene (LLDPE), manufactured as 150 μm thick films, was supplied by Blu Plast s.r.l.

0.1 mm thick sheet of commercial polyethylene terephthalate (PET) was used as target polymer sample.

3.2.2.2 Bio-waste characterization

Rosin, a natural bio-waste generally consisting in a mixture of resin acids, was chosen to explore its interaction with titanium, based on the coordination ability of the carboxylic group, and the potential consequences on the redox properties of the modified titanium oxide. An accurate chemical characterization of the bio-waste was first carried out by XRD, XPS and FTIR analyses. The XRD pattern shows the broad peak at about 15° of 2θ typical of rosins [131] (Figure 3.40).

XPS survey spectra acquired on a powdered bio-waste sample indicate the presence of only carbon and oxygen (Figure 3.41a). The curve fitting of high-resolution spectra of C

1s (Figure 3.41b) and O 1s (Figure 3.41c) signals was performed considering the functional groups and the stoichiometry of abietic acid, assuming that this compound is the major component of the bio-waste sample. In order to take into account the presence of abietic acid, C 1s signal (Figure 3.41b) was fitted considering two components ascribed to aliphatic and olefinic carbon and to carboxylic carbon of the abietic acid, located at 285.0 (0.1) eV and 289.3 (0.2) eV [132] respectively, and with an area ratio of 17:1, according to the stoichiometry of the chemical formula provided in Figure 3.41. The numbers between parentheses denotes the standard uncertainty of the results of measurements.

The O 1s signal was fitted with two Gaussian/Lorentzian curves at 532.4 (0.1) eV and 533.4 (0.1) eV ascribed to C=O and to C-OH oxygen in carboxylic group, respectively [133]. The area ratio between these components is constrained equal to 1, according to the stoichiometry.

The quantitative composition of the powdered bio-waste sample is given in the Table reported in Figure 3.41. Considering C1s signal, it is possible to estimate the amount of abietic acid in the bio-waste and it resulted to be about 80%. The experimental ($O_{C=O\,-\,Abi}$ + $O_{C\text{-}OH\,-\,Abi}$)/C_{Abi} at% ratio was found to be 0.15 (0.01), that is higher than the expected ratio from stoichiometry (0.11). This might be due to the presence of other carboxylate-bearing constituents of the bio-waste.

The chemical structure of the bio-waste was further investigated by FTIR spectroscopy. The material exhibits absorption bands at 2958 cm^{-1} and 2934 cm^{-1} ($\nu_{as\ C\text{-}H}$), at 2868 cm^{-1} ($\nu_{s\ C\text{-}H}$) and a pronounced one at 1693 cm^{-1} ($\nu_{\ C=O}$) (Figure 3.41d). Absorption bands at 1460 cm^{-1} ($\delta_{as\ C\text{-}H}$) and at 1278 cm^{-1} ($\nu_{\ C\text{-}O}$) are also observed.

Therefore, according to the above results, it can be asserted that the adopted bio-waste is mainly constituted by abietic acid, the major terpene belonging to the mixture of resin acids [134–136].

In the following, the bio-waste at issue will be considered as formed by abietic acid only and will be indicated as HAbi.

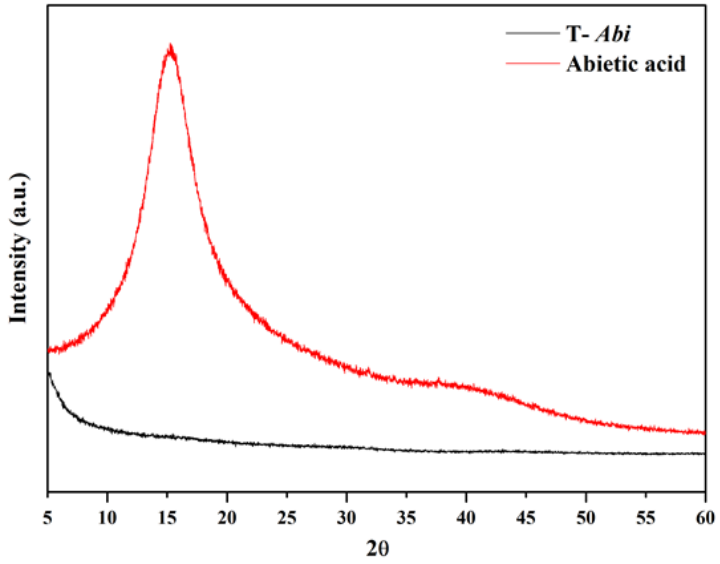

Figure 3.40. XRD spectra of Abietic acid and T-*Abi*.

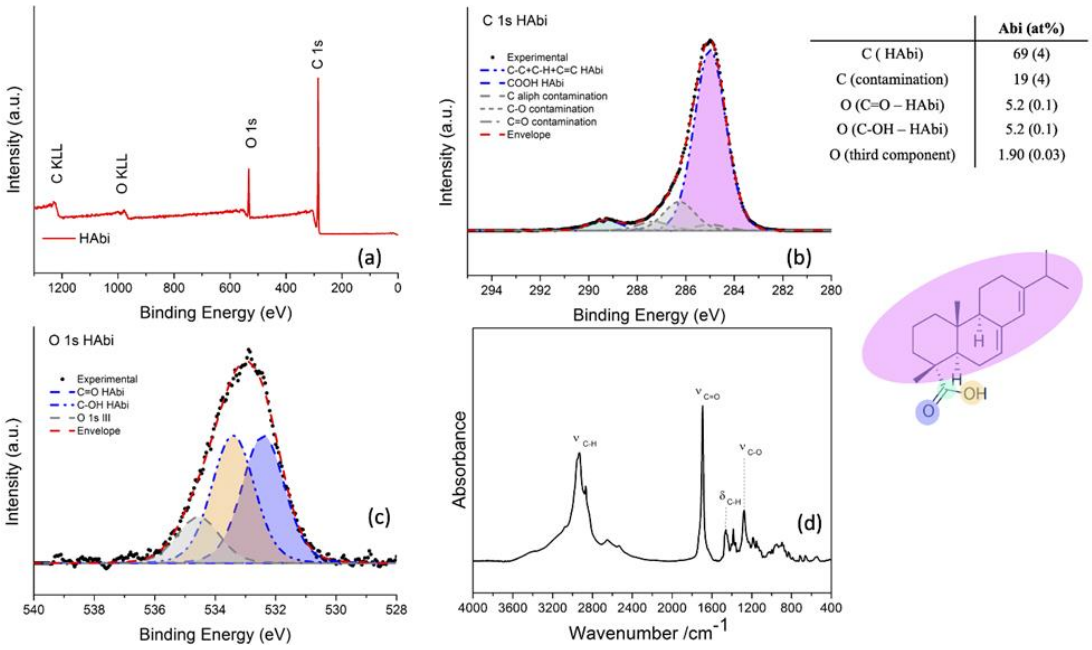

Figure 3.41. XPS spectra of the powdered bio-waste sample: a) survey spectrum; b) C 1s high-resolution spectrum: aliphatic and olefinic carbons are shadowed in pink (BE = 285.0 eV), carboxylic carbon in green (BE = 289.3 eV), c) O 1s high-resolution spectrum: C=O oxygen of carboxylic group (BE = 532.4 eV) is shadowed in blue and C-OH oxygen (BE = 533.4 eV) in orange; d) FTIR spectrum of the bio-waste. The structure of abietic acid and the quantitative composition (at%) by XPS analysis are also reported.

3.2.2.3 Theoretical investigation of the interaction between abietic acid and TiO_2 surface

Once known the chemical composition of the bio-waste, before designing a synthesis procedure, density functional theory (DFT) calculations were employed to verify if the abietic acid can form LMCT complexes with Ti^{4+}, as occurred for carboxylic acids, diols, β-diketones [127]. These complexes play a key role in the stabilization of ROS species on the surface of the hybrid materials [41,42,127]. To this aim, a detailed study of the interaction between abietic acid molecule and stoichiometric as well as O-defective TiO_2 anatase (101) surfaces was performed. Reduced TiO_2 (101) anatase surface was modeled by removing a two-coordinated O atom from the external layer of the surface resulting in two unsaturated and reduced Ti^{3+} atoms [127,137]. The abietic acid molecule is expected to interact with TiO_2 in its deprotonated form (abietate, Abi). The adsorption energies (E_{ads}, eV) of the most stable interaction between abietate and stoichiometric TiO_2 anatase surface, $ATiO_2$ (101) surface, is -1.4 eV. Despite this quite favorable E_{ads} value, the results indicate that the adsorption of the organic ligand on O-defective anatase surface (VO1) is preferred by 0.6 eV. For this reason, in the following, the interaction between the abietate and the reduced anatase surface (101) is discussed.

Figure 3.42 shows the optimized geometry of the most stable structure with the abietate adsorbed on the reduced anatase surface VO1. The computed value of the adsorption energy is of -2.0 eV. In this configuration the abietate molecule coordinates the VO1 surface adopting a bidentate coordination mode with the oxygen atoms of the carboxylate group bonded to the two tetra-coordinated reduced Ti^{3+} atoms (Ti1 and Ti2) deriving from the formation of the vacancy VO1. As a result, abietate restores the hexa-coordinated configuration of Ti1 and Ti2. The PDOS plots of the lowest energy configuration of abietate coordinated to VO1 surface, displayed in Figure 3.42b, show a valence band (VB) with mainly O 2s and 2p characters and a conduction band (CB) with Ti 3d character. The computed value of the bandgap is 2.3 eV, in agreement with the experimentally calculated value (see below). This value is smaller than the one calculated for other carboxylic acids [128], and β-diketones [127] as well as for the stoichiometric anatase surface (experimental gap of 3.2 eV [138–140] and theoretical gap of 3.0 eV [127,138]), suggesting that the coordination of abietate significantly reduces the TiO_2

surface bandgap. Filled bandgap states are generated due to the conjugated double bond of the diterpene (blue peaks between -2.0 and -2.2 eV and at -0.2 eV) and the two reduced Ti^{3+} atoms (purple peaks at -0.9 eV) [127] as confirmed by spin density analyses where the electron excess on the organic ligand and the two Ti^{3+} are indicated with blue and purple densities, respectively, analogously to the colors of the respective bandgap peaks (Figure 3.42c). The computed variation of Bader charges (Δq, e^-), indicates a charge transfer from the organic ligand to VO1 of about 0.3 e^- which adds to the excess charge already present on the surface, in agreement with the LMCT suggested by DRUV spectroscopy.

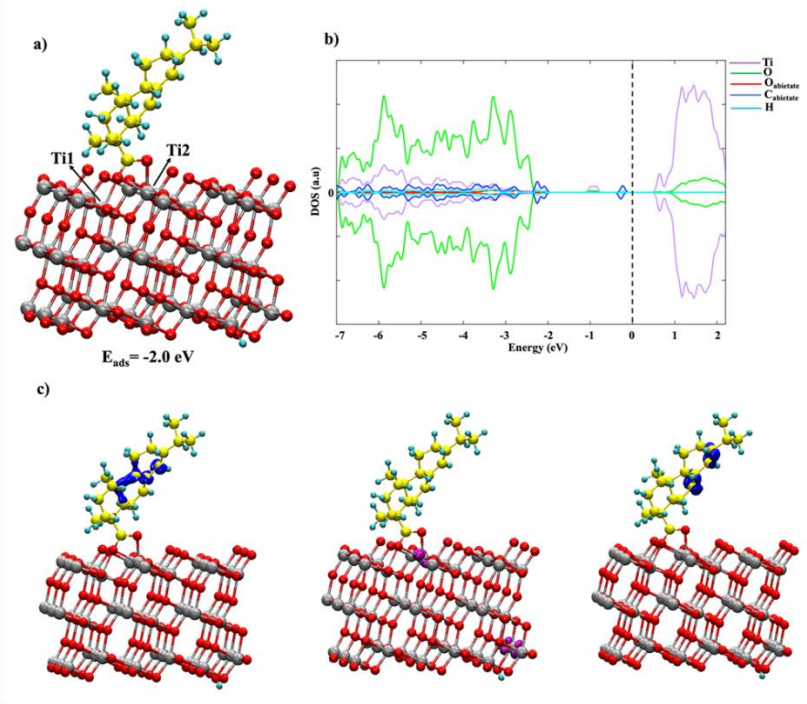

Figure 3.42. a) Optimized structure of the interaction of abietate with O-defective anatase surface (101) with the corresponding E_{ads} (eV). Ti, C, H, and O surface and ligand atoms are represented in ball and sticks and depicted in gray, yellow, cyan, and red, respectively. b) PDOS and c) spin density plots for abietate on VO1 system, respectively. The state of titanium (Ti) and oxygen (O) surface atoms, oxygen (O_{ab}), carbon (C) and hydrogen (H) ligand atoms are represented in purple, green, red, blue, and cyan, respectively. On the DOS (a.u.) axis, the values above and below 0 a.u. indicate the electrons with spin up and spin down, respectively. The Fermi energy level is represented with a red line at 0 eV.

To investigate the capability of the abietate-modified TiO_2 to form ROS in ambient conditions, the interaction between O_2 molecules and the hybrid surface was simulated. In this case, two O_2 molecules bind VO1 with an adsorption energy of -1.2 eV. The adsorption of O_2 molecules on VO1 is accompanied by a charge transfer from the surface to the O_2 molecules that turn into superoxide radical anions ($O_2^{\bullet-}$).

3.2.2.4 Synthesis procedure of hybrid T-Abi

The hybrid TiO_2-based material was prepared by a hydrolytic sol-gel route (Figure 3.43). In a typical procedure, a solution containing 5 mL of titanium (IV) n-butoxide, 20 mL of ethanol and 0.88 g of rosin (acting as a complexing ligand) was prepared and stirred for about 30 minutes. Then a second solution containing distilled water and ethanol was prepared and mixed with the first one.

The resulting molar ratio Ti : rosin : ethanol : water was 1 : 0.2 : 24 : 4.

The final solution was stirred for 2 hours and after ageing at room temperature for 24 h, it was centrifuged. The resulting particulate gel was dried at 50 °C in a ventilated oven until constant weight to obtain a light-yellow powder material, named T-*Abi* as abietic acid was the major component of the rosin.

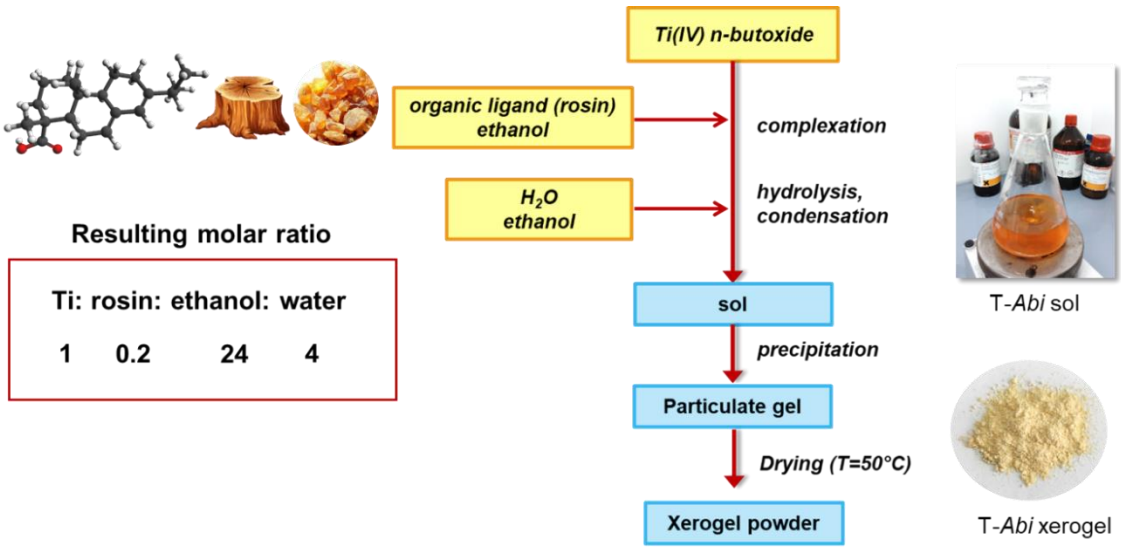

Figure 3.43. Schematic representation of the sol-gel synthesis of T-*Abi*.

3.2.3 Physicochemical characterization of hybrid T-*Abi*

SEM micrographs of hybrid T-*Abi* are shown in Figure 3.44a,b. T-*Abi* is formed by microparticles with a mean size of about 0.83 μm (Figure 3.44c).

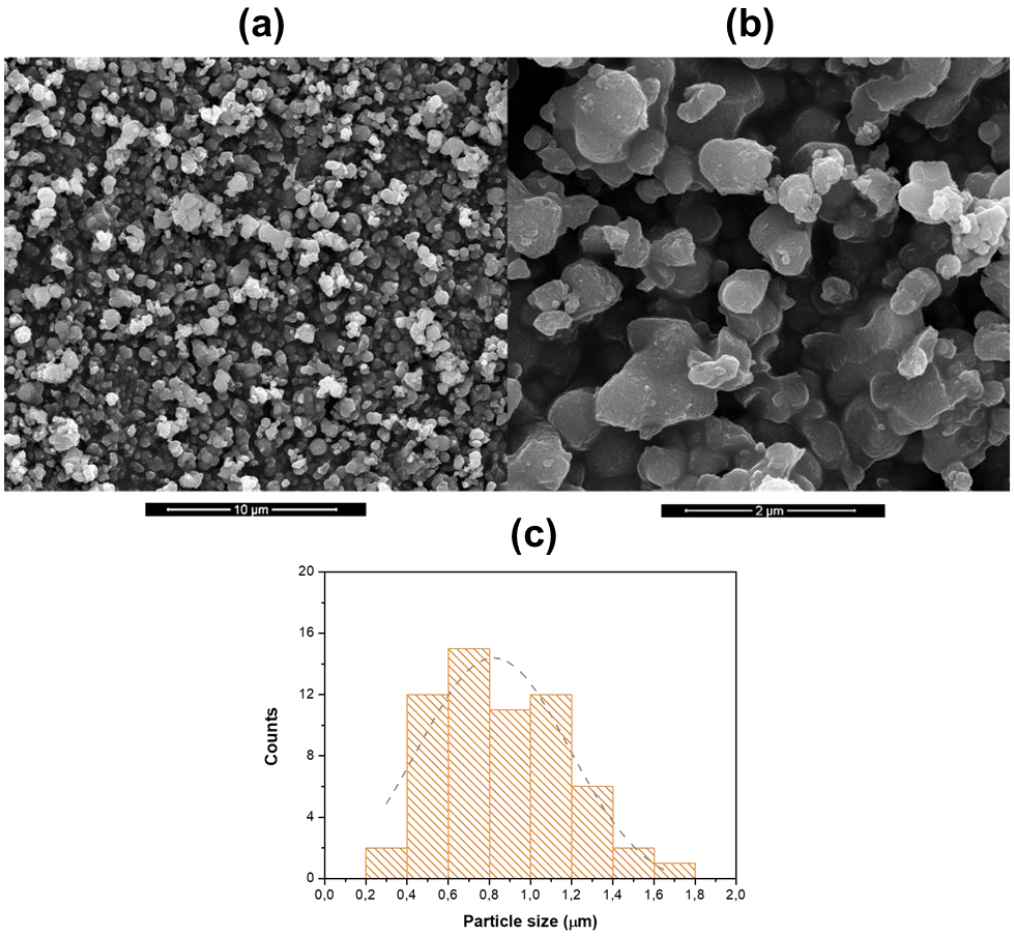

Figure 3.44. SEM micrographs (a-b) and size histogram (c) of T-*Abi*.

XPS survey of T-*Abi* shows the presence of Ti signals together with carbon and oxygen ones (Figure 3.45).

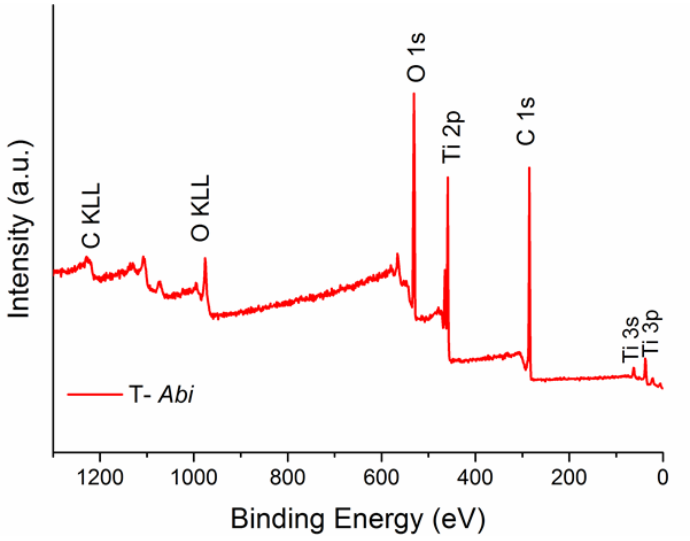

Figure 3.45. Survey spectrum of T-*Abi* sample. X-ray source: Al ka.

The high-resolution spectra of C 1s, O 1s and Ti 2p and the quantitative composition (at%) of the hybrid material determined by XPS are given in the Table reported in Figure 3.46. Curve fitting was performed for substantiating and implementing the information on the charge transfer complex T-*Abi*. Curve fitting was performed using the same parameters applied for verifying the composition of the Abi sample. The carbon C1s signal was fitted with two components ascribed to the aliphatic and olefinic carbon and to the carboxylic carbon of the abietic acid; the signals were found at 285.0 (0.1) eV and 289.3 (0.2) eV [132] (Figure 3.46a).

The oxygen, O 1s signal, was also multicomponent and it was fitted with three model curves: the one at binding energy of 530.7 (0.1) eV is ascribed to the oxygen atoms in TiO_2, -OH and oxygen in defective sites is detected at 531.9 (0.1) [139] and the peak at 532.7 (0.1) eV is assigned to the carboxylic group of the abietic acid coordinating Ti atoms. This finding is substantiating the hypothesis of the bidentate coordination mode of abietic acid (Figure 3.46b).

As far as the titanium, the most intense photoelectron signal is the Ti 2p peak (Figure 3.46c). It is characterized by the presence of an intense doublet due to the spin orbit splitting assigned to Ti (IV) and a less intense doublet due to the presence of small amounts of Ti (III). The binding energy of the Ti $2p_{3/2}$ components of the two doublets was found to be 459.1 (0.1) eV and 457.2 (0.1) eV for Ti (IV) and Ti (III) respectively, in agreement with [139].

The quantitative composition in at.% of the T-*Abi* sample determined by XPS was calculated assuming the homogeneity of the sample and it is presented in the Table reported in Figure 3.46. The results show that titanium at the surface is only partially coordinated by Abi ligands, since according to the hypothesis of the bidentate coordination mode, the stoichiometric ratio between Ti and O_{Abi} should be 1:1, and the expected ratio between these two signals would be 2.5 considering the nominal molar composition of the sample (Abi/Ti = 0.2), while the experimental one is 3.4 (0.2). This difference is due to the contribution of titanium oxide and hydroxides to Ti 2p signal, that is confirmed also by the presence of the correspondent signals in O 1s (Figure 3.46b).

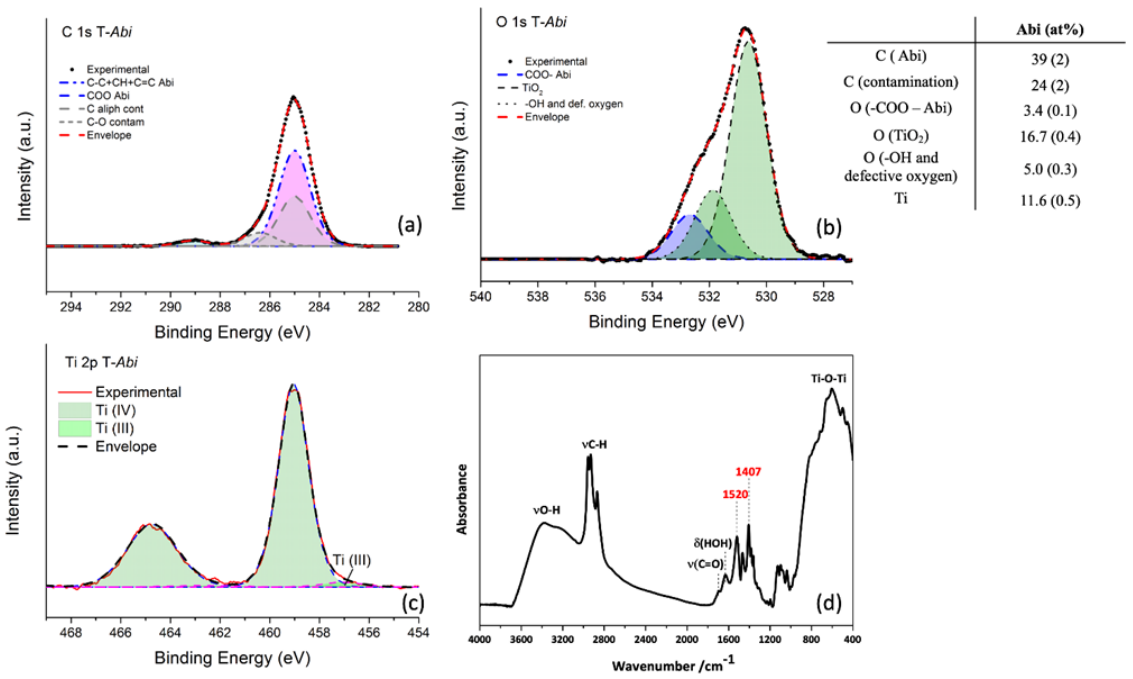

	Abi (at%)
C (Abi)	39 (2)
C (contamination)	24 (2)
O (-COO – Abi)	3.4 (0.1)
O (TiO_2)	16.7 (0.4)
O (-OH and defective oxygen)	5.0 (0.3)
Ti	11.6 (0.5)

Figure 3.46. XPS spectra of the T-*Abi* sample: a) C 1s high-resolution spectrum: aliphatic and olefinic carbons are shadowed in pink (BE = 285.0 eV), carboxylic carbon in green (BE = 289.3 eV) , b) O 1s high-resolution spectrum: the components ascribed to O^{2-} (BE = 530.7 eV) and OH^- (BE = 531.9 eV) or oxygen in defective sites are shadowed in green; COO^- oxygen atoms of carboxylic group from the abietic acid (BE = 532.7 eV) is shadowed in blue; c) Ti 2p signal; d) FTIR spectrum of T-*Abi*. The quantitative composition (at%) by XPS analysis is reported in the Table.

The hybrid nature and the coordination bonding of the T-*Abi* was additionally verified through FTIR spectroscopy. The FTIR spectrum of hybrid T-*Abi* (Figure 3.46d) shows absorption bands above 3000 cm^{-1} (ν_{O-H}), near 2900 cm^{-1} (ν_{C-H}), at 1637 cm^{-1} (δ_{HOH}) and the vibrations of Ti-O-Ti bonds below 800 cm^{-1}.

The comparison between the FTIR spectrum of the net Abi with that of T-*Abi* (Figure 3.47) shows that the band related to C=O bonds at 1693 cm^{-1} ($\nu_{C=O}$) is shifted towards low wavenumbers in the spectrum of the hybrid material, giving the asymmetric and symmetric stretching at 1520 cm^{-1} ($\nu_{as\ C=O}$) and at 1407 cm^{-1} ($\nu_{s\ C=O}$) and proving that the carboxylate groups are involved in coordinative bonds with Ti^{4+} (Figure 3.48).

The splitting between these bands, Δ, is equal to 113 cm^{-1}, confirming also the bidentate interaction between abietate and Ti^{4+} (Δ value lies in the 50−150 cm^{-1} range), in agreement with XPS results and DFT calculations [141].

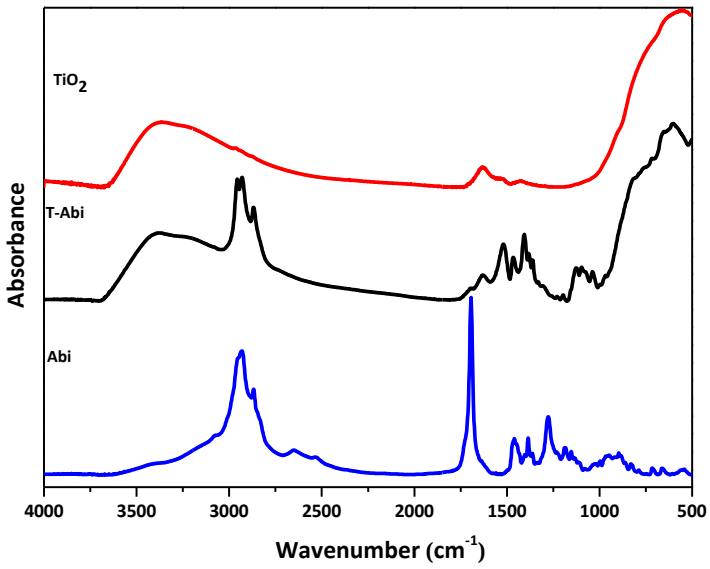

Figure 3.47. FTIR spectra of T-*Abi*, *Abi* and bare TiO_2 from 4000 cm^{-1} to 500 cm^{-1}.

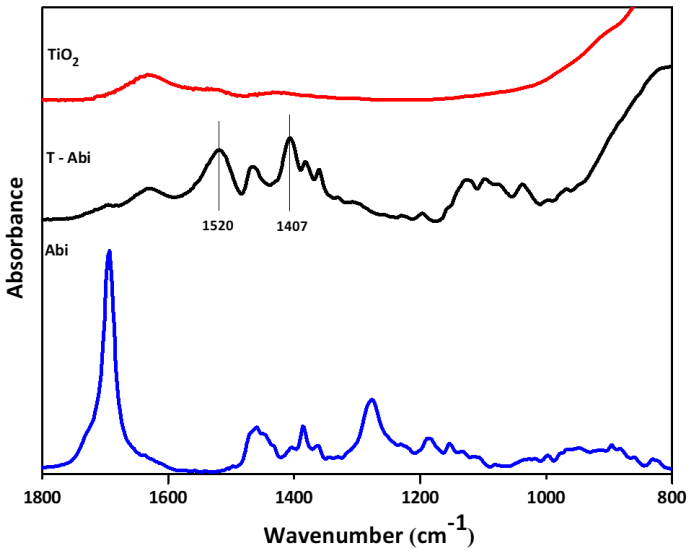

Figure 3.48. FTIR spectra of T-*Abi*, *Abi* and bare TiO_2 from 1800 cm^{-1} to 800 cm^{-1}.

The structure of the synthesized hybrid material is substantially amorphous, as ascertained by its XRD pattern (data not shown).

DRUV analysis was also performed to explore the optical behaviour of the hybrid material. The DRUV spectrum of T-*Abi* is characterized by a broad peak centred at around 250 nm with a shoulder like tail in the visible region up to 500 nm, compared to a bare TiO_2 sample prepared by an analogous sol-gel procedure without the addition of HAbi (Figure 3.49).

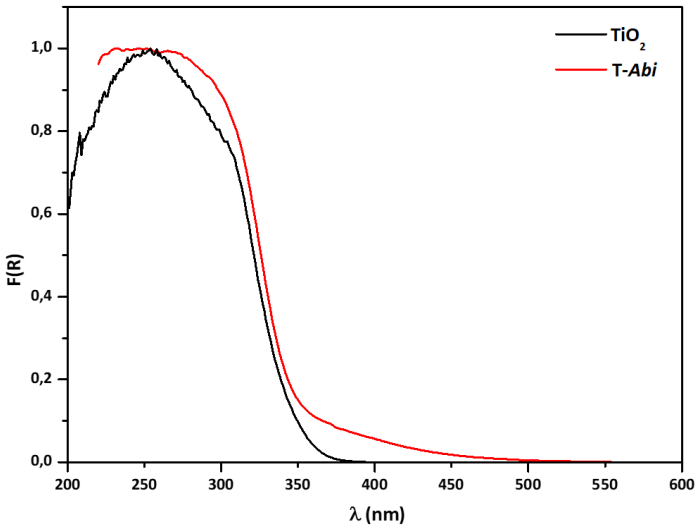

Figure 3.49. DRUV spectra of bare TiO_2 and T-*Abi*.

The implementation of Kubelka-Munk function and the Tauc plot linearization allowed the estimation of the effective band gap energy value [142]. It results to be about 2.5 eV (Figure 3.50), in fair agreement with the value of 2.3 eV predicted by DFT (Section 3.2.2.3). The partial absorption in the visible region and the observed band gap are further evidence of the formation of a charge transfer complex of TiO_2 with the abietic acid ligand.

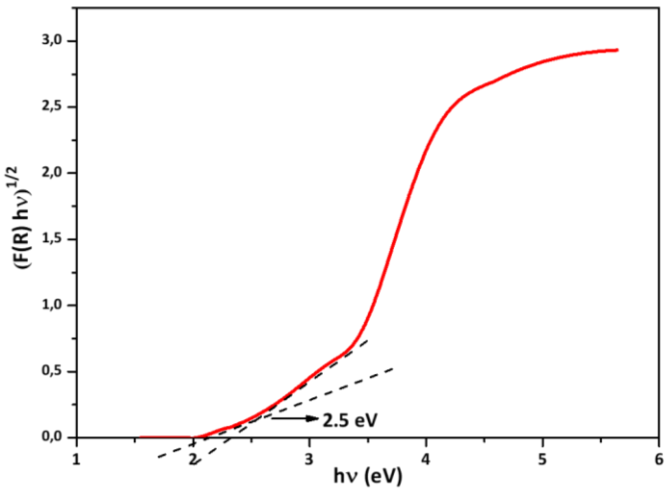

Figure 3.50. Tauc-Plot linearization of T-*Abi* for estimating the band gap energy.

The thermal stability of the hybrid T-*Abi* was investigated by thermal analysis. TG-DTA curves of T-*Abi* recorded under N_2 atmosphere are displayed in Figure 3.51. The weight loss occurs in two main regions: below 200 °C and between 300-400 °C. The former (about 10 wt. %), that takes place progressively from room temperature up to 200 °C, is related to the evacuation of water, solvent (ethanol) and the alkoxide molecules. The latter (about 46 wt.%), that occurs quickly, can be related to the volatilization of the organic ligands, as attested by the presence of two DTA endothermic peaks at about 319 and 356 °C in the corresponding DTA curve. This weight loss is close to the nominal mass content of HAbi in the hybrid material (43%).

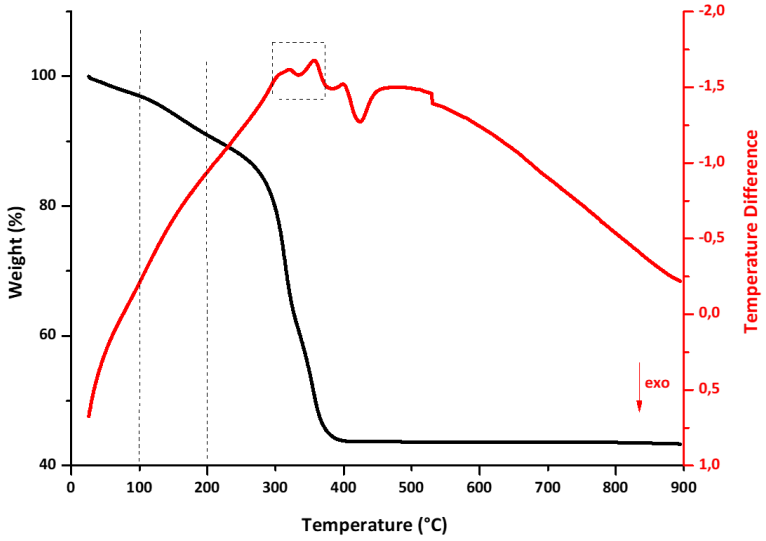

Figure 3.51. TG-DTA curves of T-*Abi*.

The presence of superoxide radical ions on the surface of the hybrid TiO_2, predicted by DFT calculations (Section 3.2.2.3) and in agreement with XPS data (presence of Ti(III) and defective oxygen), was ascertained by EPR spectroscopy.

Figure 3.52 displays the EPR spectrum of the T-*Abi* xerogel powder, which was recorded at room temperature in the dark without any sample pre-treatment. The three-component signal shows the characteristic line shape and g values of the $O_2^{\bullet-}$ radical adsorbed on the surface of titanium oxide [143]. This result unambiguously proves that T-*Abi*, simply exposed to air in ambient conditions, generates $O_2^{\bullet-}$ radicals and maintains them stably

adsorbed on its surface. Here we demonstrate that this special ability, which was previously shown by TiO_2 hybrids with β-diketones as organic ligands [42,127,144], is exhibited also by T-*Abi*. In this case, the carboxylic group of the abietic acid forms a LMCT complex with Ti^{4+} through the mechanism elucidated by DFT modelling (see Section 3.2.2.3). The EPR spectrum seems to include a relatively weak overlapped peak with a g value between 2.003 and 2.009, which could be ascribed to a carbon-centred radical species, likely formed on the organic ligand. Similar signals with diverse intensity have been observed for different cyclic and aromatic molecules bonded with titanium in hybrid gels [128]. The spontaneous production of ROS on the surface of the hybrid material without the need for direct light irradiation encouraged us to test T-*Abi* in the oxidative degradation of a model microplastic.

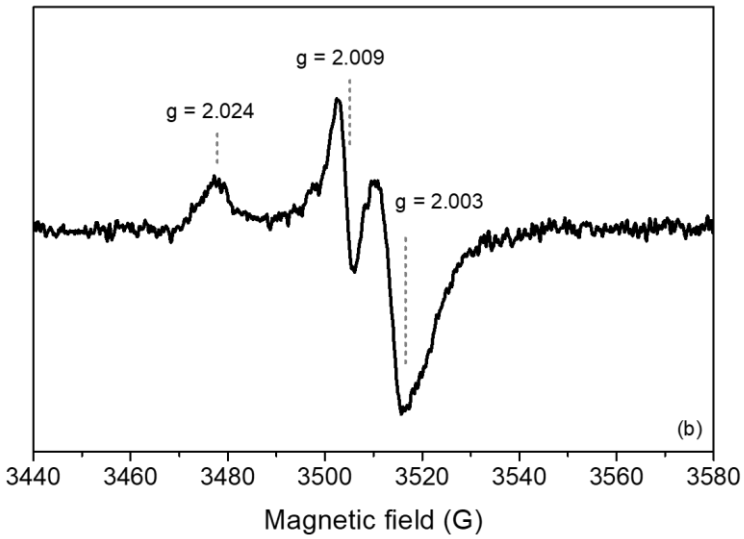

Figure 3.52. EPR spectra of T-*Abi* powder.

The EPR spin trapping method was employed to investigate the capability of T-*Abi* to generate ROS in the aqueous environment (Figure 3.53). The short lifetime of ROS in solution makes their direct determination by EPR very tough. Therefore, DMPO spin-trap was used, as it can react with unstable oxygen-centered radicals, forming new longer-living radical adducts observable by EPR.

The appearance of a signal in the EPR spectrum of the supernatant was observed, showing a characteristic quartet with a 1:2:2:1 intensity ratio, which corresponds to the DMPO-OH adduct formed from the trapping of hydroxyl radical, $OH^{\bullet}$, on DMPO [41,145]. The quantitative analysis of this spectrum was realized determining the hyperfine coupling constants for the nitroxide nitrogen and for the β-proton ($a_N = a_{\beta H} = 14.8 \pm 0.1$ G), in agreement with those reported in the literature [41,145], thus confirming the formation of $OH^{\bullet}$ radicals.

As previously reported [146,147]**,** their most probable source is from surface adsorbed $O_2^{\bullet-}$ that easily reacts with water forming hydroperoxyl radical ($HO_2^{\bullet}$), then H_2O_2 and finally $OH^{\bullet}$, which may take part in the degradation of LLDPE.

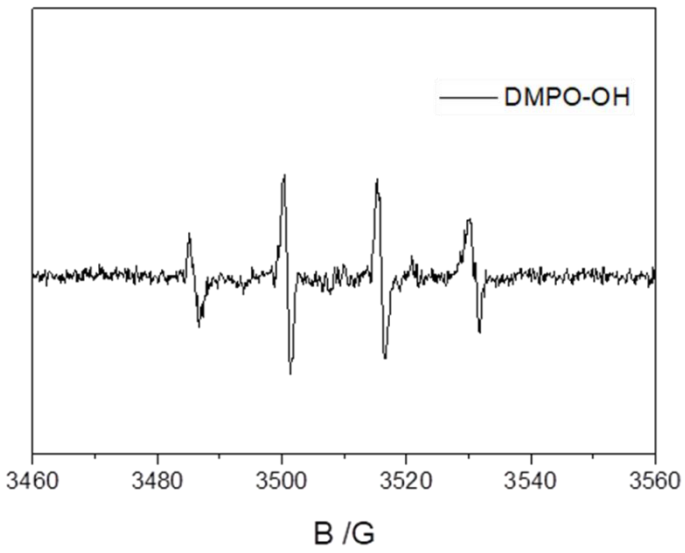

Figure 3.53. DMPO-OH spin-adduct formed in aqueous medium in the presence of T-*Abi* (c).

Furthermore, it should be noted that the formation of Ti-*Abi* complexes hinders the auto-oxidation phenomena generally occurring in the case of resin acids that, according with time and temperature, transform into more oxidized compounds, like dehydroabietic acid, 15-hydroxy-7-oxodehydroabietic acid and isopimaric acid [134,135].

3.2.4 Degradation test of LLDPE MPs in the presence of T-*Abi*

After synthesized T-Abi material, a reaction system was set-up as follows.

An aqueous suspension of T-*Abi* (1 mg/mL) was prepared in a 50 mL volume becker. Then, after stirring it for about 10 min, 12 pieces of LLDPE (5 mm x 5 mm) were added to the suspension. The whole system was kept under magnetic stirring for 4 days, 14 days and 1 month, so to investigate the degradation of the polymer at different incubation times.

The tests were performed at room temperature (about 30 °C) in indirect daylight conditions, i.e., under artificial laboratory illumination during the working days and darkness along the night.

The experimental set-up is schematized in Figure 3.54.

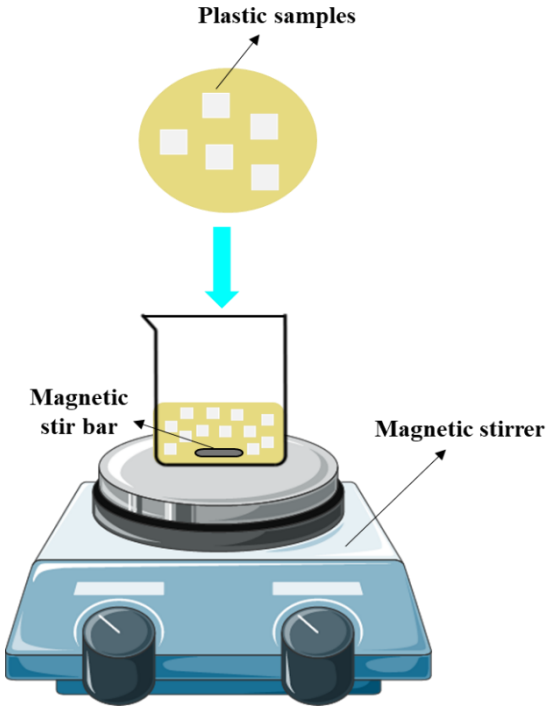

Figure 3.54. Schematic representation of the experimental set-up used.

3.2.5 Degradation test of PET MPs in the presence of T-*Abi*

Three different aqueous suspensions of T-*Abi* material at different concentration (1 mg/mL, 2 mg/mL, 4 mg/mL) were prepared.
Then, after stirring them for about 10 min by means of a shaker (Figure 3.55), 12 pieces of PET (4 mm x 4 mm) were added to the suspensions. The whole system was kept under stirring for 7 days, 14 days and 1 month, so to investigate the degradation of the polymeric at different incubation times.

The tests were performed at room temperature (about 30 °C) in indirect daylight conditions, i.e., under artificial laboratory illumination during the working days and darkness along the night.

Figure 3.55. Degradation test of PET MPs in the presence of T-*Abi*.

3.2.6 Degradation mechanism of LLDPE MPs

As previously described, LLDPE samples were immersed in an aqueous suspension of T-*Abi* (1 mg/mL) and stirred by the aid of a magnetic stirrer until 1 month at indirect daylight, without any external excitation source. This choice was adopted both to exploit an oxidative degradation pathway closer to real environmental conditions, fulfilling the day-night illumination cycle, and to establish a green and cost effective microplastic decontamination strategy.

After incubation, the aqueous suspension of T-*Abi* was recovered by centrifugation at 10000 rpm for 10 min. The supernatant obtained was filtered (0.45 μm), lyophilized, subjected to extraction, and finally analysed by means of GC-MS.

The GC-MS analysis of the degradation by-products obtained from LLDPE incubated for 1 month allowed us to identify various short-chain compounds shown in Figure 3.56a, where the total chromatogram of the degradation products is also reported.

The identified compounds can be included in three classes: alkanes, alcohols and esters (Figure 3.56b); moreover, their absence in the control, obtained by incubating T-*Abi* for 1 month without LLDPE, demonstrates that the degradation of LLDPE occurred effectively.

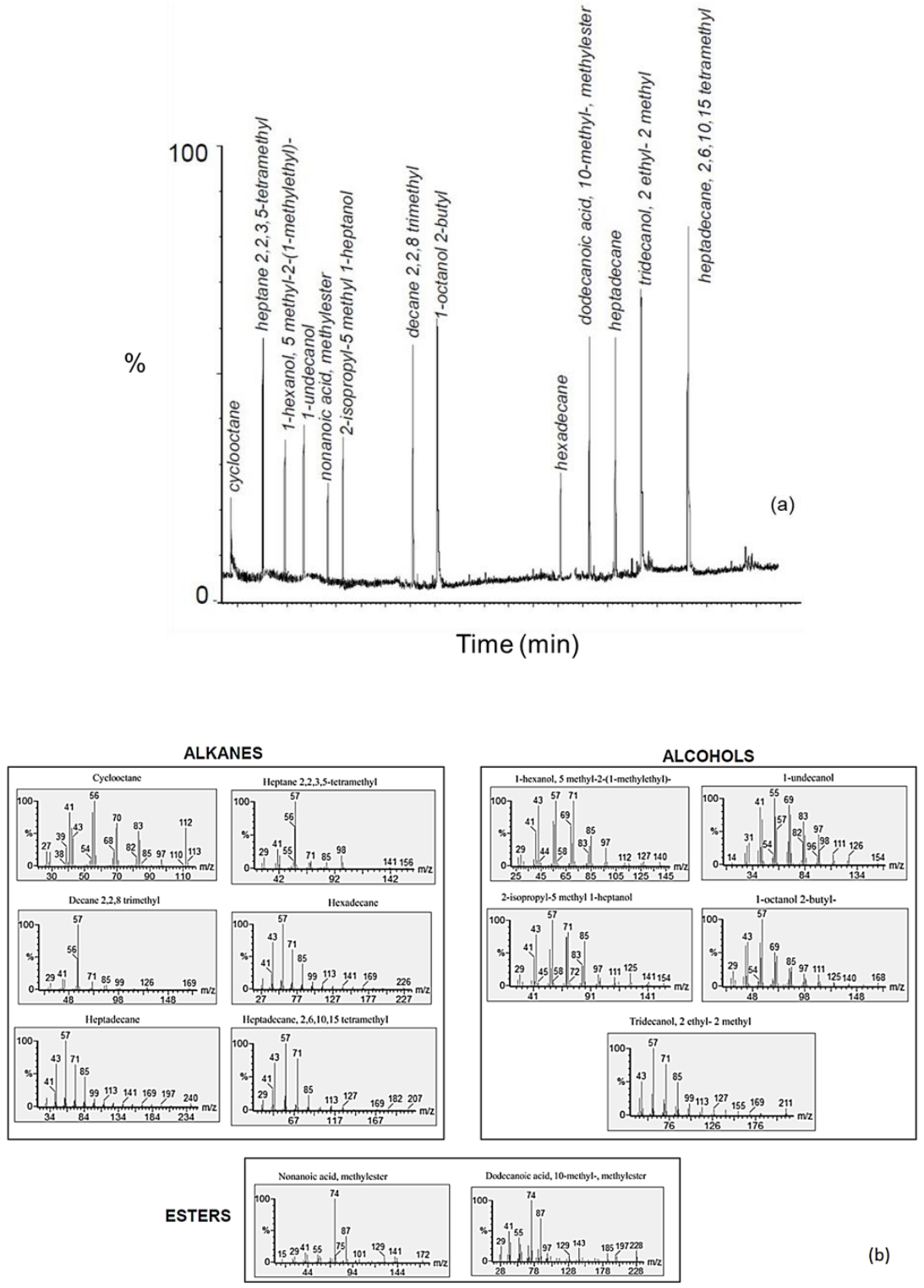

Figure 3.56. Total chromatogram of the degradation by-products obtained after incubation of LLDPE with T-*Abi* for 1 month (a) and standard mass spectrum of each compound identified (b).

The degradation by-products detected by GC-MS are recognized as environmentally friendly low-molecular-weight organic compounds. In previous works, similar organic compounds were found as intermediates of MPs degradation. These latter were demonstrated to be of low toxicity, even acting as the carbon source for algae growth [148,149]. Considering that T-*Abi* is an amorphous material with a high content of organic component, a significant photooxidation contribution can be excluded (see Figure 3.40).

Based on the GC-MS results reported above, the following degradation mechanism of LLDPE might be proposed (Scheme 3.1).

As shown in Scheme 3.1, a possible route, occurring in the aqueous suspension, may involve the homolytic scission of LLDPE polymer in the presence of an $OH^{\bullet}$ radical, generated in solution by T-*Abi*, as demonstrated by the spin-trapping EPR spectrum of DMPO-OH adduct (Figure 3.52), forming a generic alkyl radical ($R_1\bullet$).
This radical may be terminated by reaction with another alkyl radical ($R_2\bullet$), probably generated by a similar mechanism, to provide an alkane (R_3H).
Alternatively, $R_1\bullet$ radical may undergo termination by reaction with an $OH^{\bullet}$ radical, resulting in the production of an alcohol (R_1OH). Due to the presence of the ROS species in solution, a further oxidation of the alcohol (R_1OH) can occur giving a carboxylic acid (R_4COOH).
In this reaction environment, in presence of the T-*Abi*, the carboxylic acid (R_4COOH) could react with an alcohol (R_5OH) to form an ester (R_4COOR_5) through an esterification reaction, possibly aided by the acidic character of the TiO_2 surface.

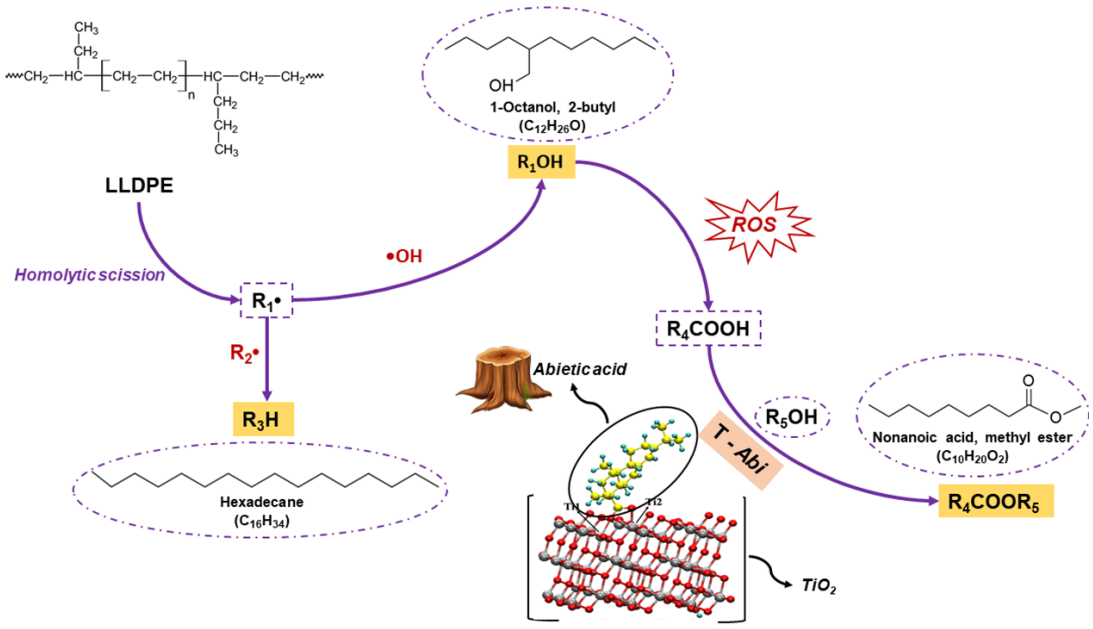

Scheme 3.1. Schematic representation of the possible LLDPE degradation mechanism in the presence of T-*Abi*.

In the literature, the mechanism generally reported for the photoinitiated oxidative degradation of LLDPE (or polypropylene) is the following [68,150–152]. In the initiation step, the photogenerated hydroxyl radicals $OH^{\bullet}$ break the C-H bonds on the polymer backbone and generate polyethylene alkyl radicals $(–CH_2–CH•–)_n$. During propagation, an alkyl radical reacts with oxygen to form a peroxyl radical $(–CH_2–HCOO•–CH_2–)_n$ that extracts a hydrogen atom from another polymer chain to form hydroperoxide species $(–CH_2–HCOOH–CH_2–)_n$. The hydroperoxide, an unstable specie, is further cleaved into two new free oxy and hydroxyl radicals by the scission of the weak O–O bond. In conclusion, β-scission and chain transfer of these carbon-centred radicals give rise to the random C–C backbone cleavage and molecular weight reduction. Accordingly, in the end, the existence of carbonyl compounds (e.g., aldehydes, carboxylic acids and ketones) usually confirms the photo-oxidative degradation of long- and short-branched polyolefins.

Some similarities can be found between the above reported mechanism and the radical-mediated reaction pathway envisaged to occur in our case, driven by the generated ROS.

As a matter of fact, both involve the formation of $OH^{\bullet}$ radicals that are either photogenerated or produced through the reaction of superoxide ion radicals with H_2O.

3.2.7 Physicochemical characterization of LLDPE MPs treated with T-*Abi*

The progressive modification and degradation of LLDPE was assessed after 4 days, 14 days and 1 month of processing by means of XRD, DSC and ATR-FTIR.

Figure 3.57a displays XRD diffractograms of bare LLDPE and the one treated for 1 month. XRD plot of bare LLDPE shows the typical reflections (i.e., (110), (200) and (020)) of the orthorhombic crystal structure, which are responsible for the appearance of three main peaks at 21.8°, 24.1° and 36.5° [153]. It is possible to observe that, in the case of treated LLDPE sample, these peaks shift to lower 2θ angles, due to an increase of interplanar distances (d) changing from 7.38 Å and 4.92 Å to 7.52 Å and 4.99 Å for a and b axes, respectively (Figure 3.57a).

Table 3.6 reports the crystallinity degree (X_c) of both bare and treated LLDPE samples evaluated as described in Section 5, and the mean size of crystallites (D) determined by Scherrer equation. The increase of both D and X_c values sheds some light on the degradation mechanism of LLDPE. T-*Abi* is responsible for the oxidative degradation of LLDPE, which results in a secondary crystallization phenomenon and in an increase of the crystal size. More in detail, the action of T-*Abi* makes the polymer chains, in the amorphous region, more mobile and free to further crystallize [116].

To confirm that the degradation mechanism of LLDPE occurs through an increase of its crystallinity degree, DSC measurements were performed on pristine and treated LLDPE samples and the resulting thermograms are shown in Figure 3.57b. The enthalpic crystallinity index was estimated for bare and treated LLDPE, together with their melting temperatures (T_m), following the procedure reported in Section 5. As shown in Figure 3.57b, the oxidative degradation of LLDPE causes the increase of the enthalpic crystallinity grade, which changes from 33 to 36 % in agreement with XRD analysis (Table 3.6) [154]. The degradation of LLDPE leads to an increase of the crystallinity

degree and of the concentration of chemical impurities (i.e., by-products with low molecular weight derived from the degradation process) [80,117], in agreement with the slight decrease of the melting temperature from 127.6 °C (bare LLDPE) to 125.6 °C (treated LLDPE).

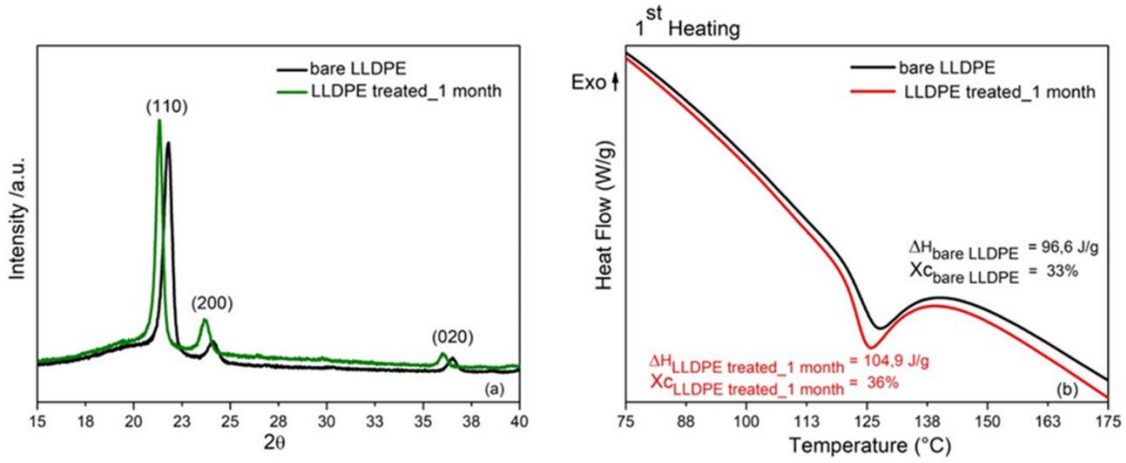

Figure 3.57. a) XRD spectra of bare LLDPE and LLDPE treated with T-*Abi* for 1 month and b) Thermograms for bare LLDPE and LLDPE treated with T-*Abi* for 1 month (first heating).

Table 3.6. Values of crystallite sizes, D, crystalline indexes, Xc and carbonyl index, C.I., of LLDPE samples before and after the treatment with T-*Abi*.

Sample	**D_{110} (Å)**	**D_{200} (Å)**	**D_{020} (Å)**	**X_c (%)** ***X-ray analysis***	**X_c (%)** ***Thermal analysis***	**Carbonyl Index, C.I.**
Bare LLDPE	156	105	126	34	33	0.040
LLDPE treated 1 month	217	141	171	39	36	0.13

To monitor the chemical changes on the film surfaces induced by the treatment in the presence of T-*Abi*, ATR-FTIR spectra of LLDPE samples were recorded, as shown in Figure 3.58.

Beside the characteristic IR bands of bare LLDPE already described in Section 3.1.5.1, ATR-FTIR analysis demonstrated the appearance of new significant IR bands during the treatment, already after 4 days. Indeed, *i)* a broad band in the range 3600-3200 cm^{-1} (ν_{OH}), ascribable to the presence of hydrogen-bonded products; *ii)* a small band in the range 1700-1500 cm^{-1} ($\nu_{C=O}$), the intensity of which increases slightly over the time [80] and *iii)* two peaks, the first in the range (1237 cm^{-1}-1210 cm^{-1}) and the second at 1150 cm^{-1}. The appearance of the band related to carbonyl group was widely associated in literature [69,155] to the surface oxidation extent of MPs, and the related carbonyl index (CI) was evaluated and displayed in Table 3.6. It should be noted that, recently, the CI index was adopted as a method to estimate the degradation efficiency of LDPE films [156]. Even if it is not easy to compare our results with the ones obtained under UV exposure, the observed CI change appears significant, considering that it was obtained in absence of any direct illumination source.

The highest IR bands appearing during the degradation of LLDPE, occurred in the range (1237-1150) cm^{-1}, assigned to polytetrafluoroethylene (PTFE) [157] highlight that the exploited oxidative mechanism may also alter the backbone of materials like PTFE, generally recognized as chemically resistant and inert. Based on that, it seems that the treatment of LLDPE samples with T-*Abi* may induce an exfoliation of PTFE from the virgin magnetic stir bar used during the experiments, as already observed in a recent study [158].

This evidence occurred will be further investigated and discussed in the Section 3.3.

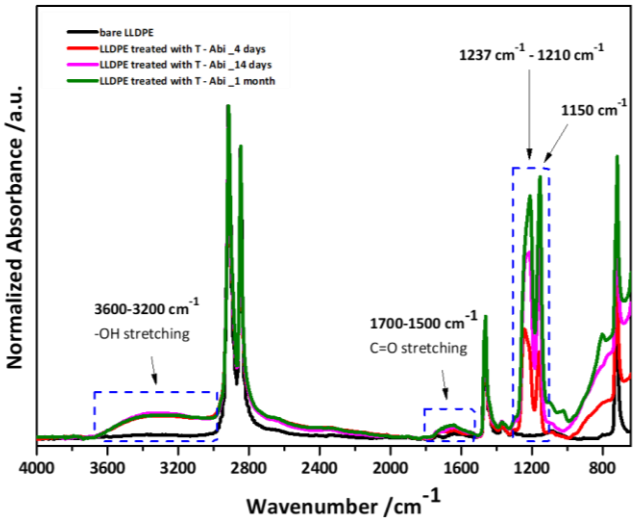

Figure 3.58. ATR-FTIR spectra of bare LLDPE and LLDPE treated with T-*Abi* for 4 days, 14 days and 1 month.

3.2.8 Degradation of PET MPs in the presence of T-*Abi*

As previously described in Section 3.2.5, PET samples were immersed in three different aqueous suspension of T-*Abi* (1 mg/mL, 2 mg/mL, 4 mg/mL) and stirred by the aid of a shaker until 1 month at indirect daylight, without any external excitation source. The choice of the shaker was adopted to avoid the risk of contamination due to the exfoliation of PTFE-coated magnetic stir bars detected in previous experiments (see Section 3.2.7).

After incubation, the aqueous suspensions of T-*Abi* were recovered by centrifugation at 10000 rpm for 10 min. The supernatants obtained were filtered (0.45 μm), subjected to extraction, and finally analysed by means of GC-MS.

The GC-MS analysis did not reveal any degradation by-products from PET incubated for 1 month with T-*Abi* (1 mg/mL), while different compounds were identified from PET incubated with T-*Abi* (2 mg/mL) (see Table 3.7) and T-*Abi* (4 mg/mL) (see Table 3.8). The identified compounds can be included in three classes: alkanes (straight-chain, branched and cyclic), esters and alcohols. Moreover, their absence in the control, obtained by incubating T-*Abi* for 1 month without PET, demonstrates that the degradation of PET occurred effectively.

Table 3.7. Degradation by-products of PET, identified by GC-MS, after treatment with T-*Abi* (2 mg/mL).

Compound	**Molecular formula**	**Molecular mass (g mol^{-1})**
Octadecane 2,6,10,14-tetramethyl	$C_{22}H_{46}$	310
Heptadecane 8-methyl	$C_{18}H_{38}$	254
Heptadecane, 2,6,10,15 tetramethyl	$C_{21}H_{44}$	296
7 Methyl-octodecane	$C_{19}H_{40}$	268
Undecane, 5-ethyl-5-propyl	$C_{16}H_{34}$	226
1,4-Dimethylcyclohexane	C_8H_{16}	112
1-Ethyl-2-Methylcyclohexane	C_9H_{18}	126
Ethylbenzene	C_8H_{10}	106
Pentanoic acid 2-ethylhexylester	$C_{13}H_{26}O_2$	214
2,2 dimethyl propanoic acid, 4-hexadecylester	$C_{21}H_{42}O_2$	326
2,2-dimethylpropanoic acid, nonylester	$C_{14}H_{28}O_2$	228
Pentanoic acid, propyl ester	$C_8H_{16}O_2$	144
Tridecanol, 2 ethyl-2-methyl	$C_{16}H_{34}O$	242

Table 3.8. Degradation by-products of PET, identified by GC-MS, after treatment with T-*Abi* (4 mg/mL).

Compound	**Molecular formula**	**Molecular mass (g mol^{-1})**
Nonadecane	$C_{19}H_{40}$	268.53
Tetracosane	$C_{24}H_{50}$	338.70
Pentacosane	$C_{25}H_{52}$	352.68
Eicosane	$C_{20}H_{42}$	282.55
Hexacosane	$C_{26}H_{54}$	366.71
Eicosane, 9-octyl-	$C_{28}H_{58}$	394.76
Tetradecane	$C_{14}H_{30}$	198.39
Hexadecane	$C_{16}H_{34}$	226.44
Octadecanoic acid, 2,3-dihydroxypropyl ester	$C_{21}H_{42}O_4$	358.55
Hexadecanoic acid, 2-hydroxy-1-(hydroxymethyl)ethyl ester	$C_{19}H_{38}O_4$	330.50
2-Heptadecenal	$C_{17}H_{32}O$	252.40

However, the experimental results shown are preliminary and the degradation of PET MPs in the presence of T-*Abi* will be further investigated in the future.

3.3 Physical and chemical degradation of PTFE magnetic stir bars

PTFE is a fluorinated polymer that exhibits many interesting properties, such as high chemical and thermal stability, strong surface hydrophobicity, low dielectric constant, and high piezoelectric activity [159]. Specifically, PTFE magnetic stir bars are widely used in laboratory, industrial, and biomedical routine activities due to their chemical inertness.
The exfoliation of the external layers of PTFE-coated magnetic stir bars was observed in our recent experimentation dealing with the indirect daylight oxidative degradation of LLDPE MPs, that does not require any direct energy source (irradiation or heat) and takes place in atmosphere and at room temperature [130].
Chemical degradation of LLDPE occurred within 1 month giving alkanes, alcohols and esters and, simultaneously, the surface exfoliation of the PTFE magnetic stir bar was evidenced already after 4 days in the presence of T-*Abi* (Section 3.2.9).
In this section, a specific experimentation is reported to evidence and clarify the role played by T-*Abi* in PTFE exfoliation and an astonishing result was discovered: the chemical degradation of the external layer of PTFE magnetic stir bar with the formation of fluorinated esters and alkanes [160].

3.3.1 Degradation test of PTFE magnetic stir bars

Two aqueous suspensions were prepared in a 50 mL beaker of borosilicate glass each of them containing commercial PTFE magnetic stir bar of the same size (3 cm) that had never been used before. The suspension A contained only T-*Abi* (1 mg/mL); the suspension B consisted in T-*Abi* (1 mg/mL) and 12 pieces of LLDPE (5 mm × 5 mm). The adopted experimental conditions were the same as the conditions previously optimized for investigating the chemical degradation of LLDPE (Section 3.2.4).
Moreover, to further confirm the degradative activity of T-*Abi* on PTFE, a suspension C, only containing TiO_2 P90 (1 mg/mL) and stirred with a commercial PTFE magnetic stir bar, that had never been used before and whose size was the same of those used to stir the suspensions A and B, was also prepared.

For comparison, a blank sample consisting of a PTFE magnetic stir bar, that had never been used before and whose size was the same of those used to stir the above suspensions, was introduced in a borosilicate glass beaker filled with the same volume of water used for the preparation of the above suspensions and left stirring for 1 month.

3.3.2 Physicochemical characterizations

The solid residues obtained through centrifugation from the above A and B aqueous suspensions with T-*Abi* were examined by XRD, ATR-FTIR spectroscopy, and XPS, and, hereafter, will be denoted as: A-4d, A-1m, and B-1m, respectively.

The PTFE exfoliation was already evident after 4 days and became increasingly marked along the time up to one month, as demonstrated by the FTIR and XRD results displayed in Figures 3.59a,b. The typical absorption bands of PTFE at 1210 cm^{-1} ($\nu_{as\ C\text{-}F}$), 1150 cm^{-1} ($\nu_{s\ C\text{-}F}$) and 639 cm^{-1} ($\omega_{\ C\text{-}F}$) [161] are clearly visible on the surface of A-4d, A-1m and B-1m (Figure 3.59a). Moreover, the analysis of XRD patterns of A-4d, A-1m, and B-1m, showing the most intense XRD peaks of PTFE [162], confirms the presence of exfoliated PTFE (see Figure 3.59b).

However, after one month of incubation, an impressive exfoliation of the PTFE magnetic stir bar was observed for the TiO_2 P90, as clearly shown in the photographs of Figures 3.59c,d. The external PTFE layer appears in more points almost completely removed, resulting in the exposure of the metallic part of the stir bar and in the complete covering by PTFE residues of the walls of the glass beaker containing suspension C, as confirmed by FTIR spectrum of the white precipitate, displayed in Figure 3.59e, where absorption bands of PTFE at 1210 cm^{-1}, 1150 cm^{-1} and 639 cm^{-}1 are evident. This result demonstrates that TiO_2 P90 exerts a strong tribological effect, inducing a progressive erosion of surface layers of the PTFE coating and giving a macroscopic exfoliation of the PTFE magnetic stir bar after 1 month of incubation. The exfoliated PTFE fragments, being strongly hydrophobic, tend to adhere to solid surfaces, particularly those with low polarity, such as LLDPE or T-*Abi* (because of the exposed abietate ligands). On the contrary, the PTFE magnetic stir bar that was used to stir the beaker containing only water after 1 month did not reveal any evidence of exfoliation.

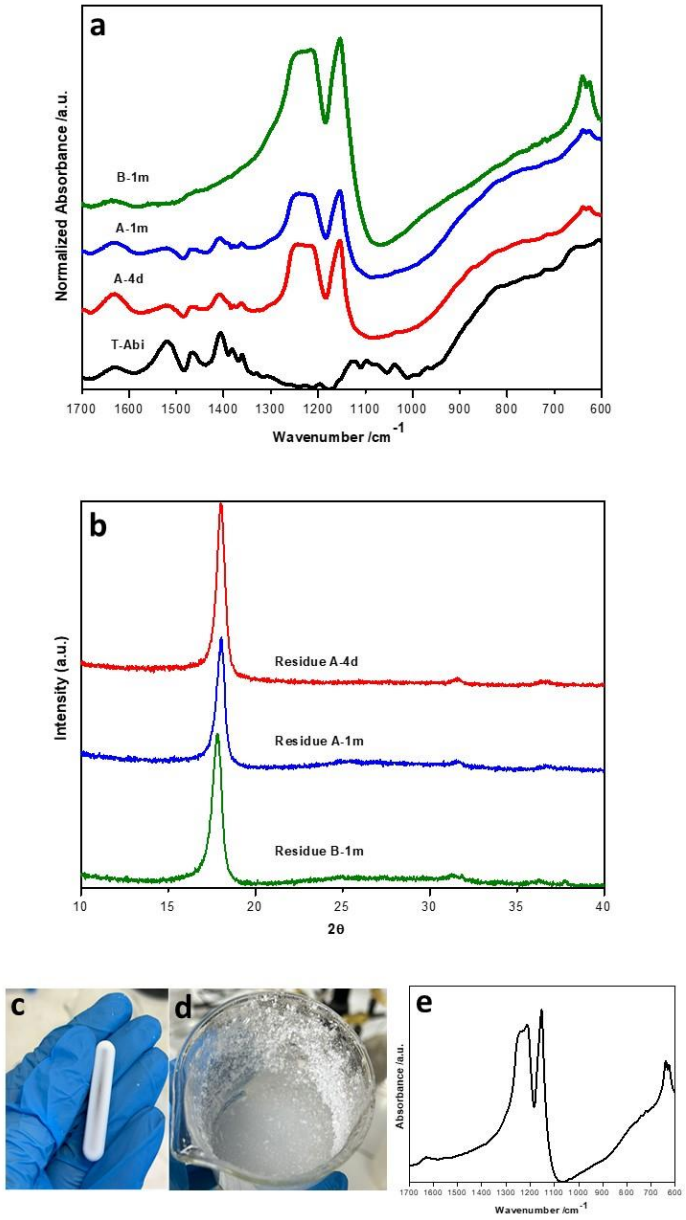

Figure 3.59. (a) FTIR spectra of: bare T-*Abi*, T-*Abi* incubated 4 days (A-4d) and 1 month (A-1m,) without LLDPE, T-*Abi* incubated 1 month with LLDPE (B-1m); (b) XRD profiles of: T-*Abi* incubated 4 days (A-4d) and 1 month (A-1m) without LLDPE, T-*Abi* incubated 1 month with LLDPE (B-1m) (c) PTFE magnetic stir bar that was used to stir the suspension C after 1 month; (d) the glass beaker that contained the suspension C after 1 month; (e) FTIR spectrum of the white precipitate on the beaker walls of Fig 3.60(d).

Then, the A-1m, B-1m, and C aqueous suspensions were recovered by centrifugation at 10000 rpm for 10 min after incubation to examine the presence of eventual degradation products. The supernatants obtained were filtered (0.45 µm), lyophilized, submitted to extraction, and finally analysed by means of GC-MS.

The analysis of GC–MS spectra performed on suspension C (TiO_2 P90 in water stirred with the PTFE bar) did not reveal any degradation products. In contrast, dodecyl 2-fluoroacetate and 1-fluorododecane were identified in suspension A-1m (Figure 3.60a), while only 1-fluorododecane was found in suspension B-1m (Figure 3.60b). It should be noted that any compound was identified by GC–MS analysis performed on the blank sample (only water).

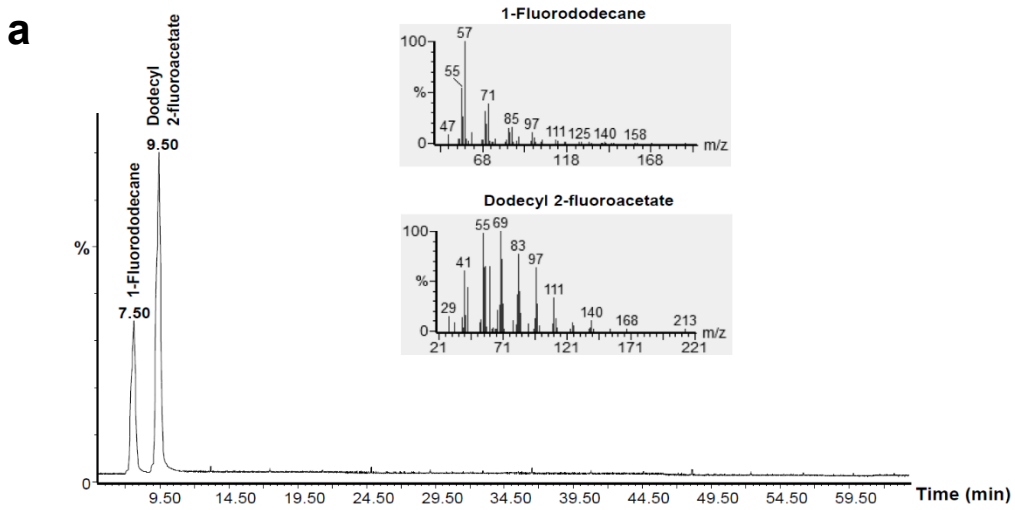

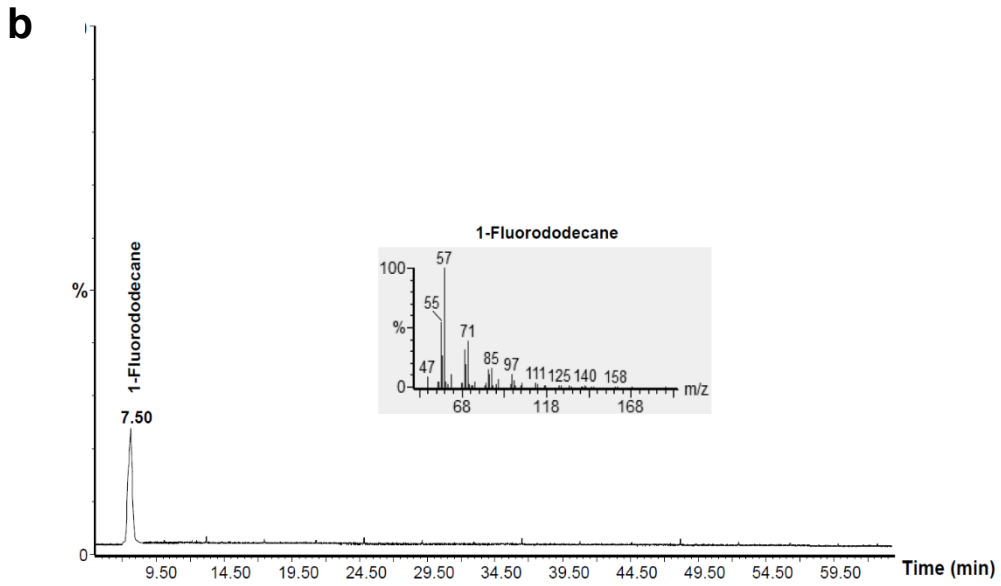

Figure 3.60. Total chromatogram of the degradation by-products obtained analysing the supernatants of a) suspension A-1m, b) suspension B-1m, and standard mass spectrum of each compound identified.

To the best of our knowledge, the degradation by-products originating from a PTFE magnetic stir bar are here identified for the first time.

We assume that these products are originated by the degradation of organic fluorinated additives, such as per- or poly-fluoroalkyl compounds, used in the manufacturing of PTFE stir bars [163].

The PTFE exfoliation was confirmed through XPS analyses of A-4d, A-1m and B-1m sanples. The XPS survey spectra can be found in Figure 3.61.

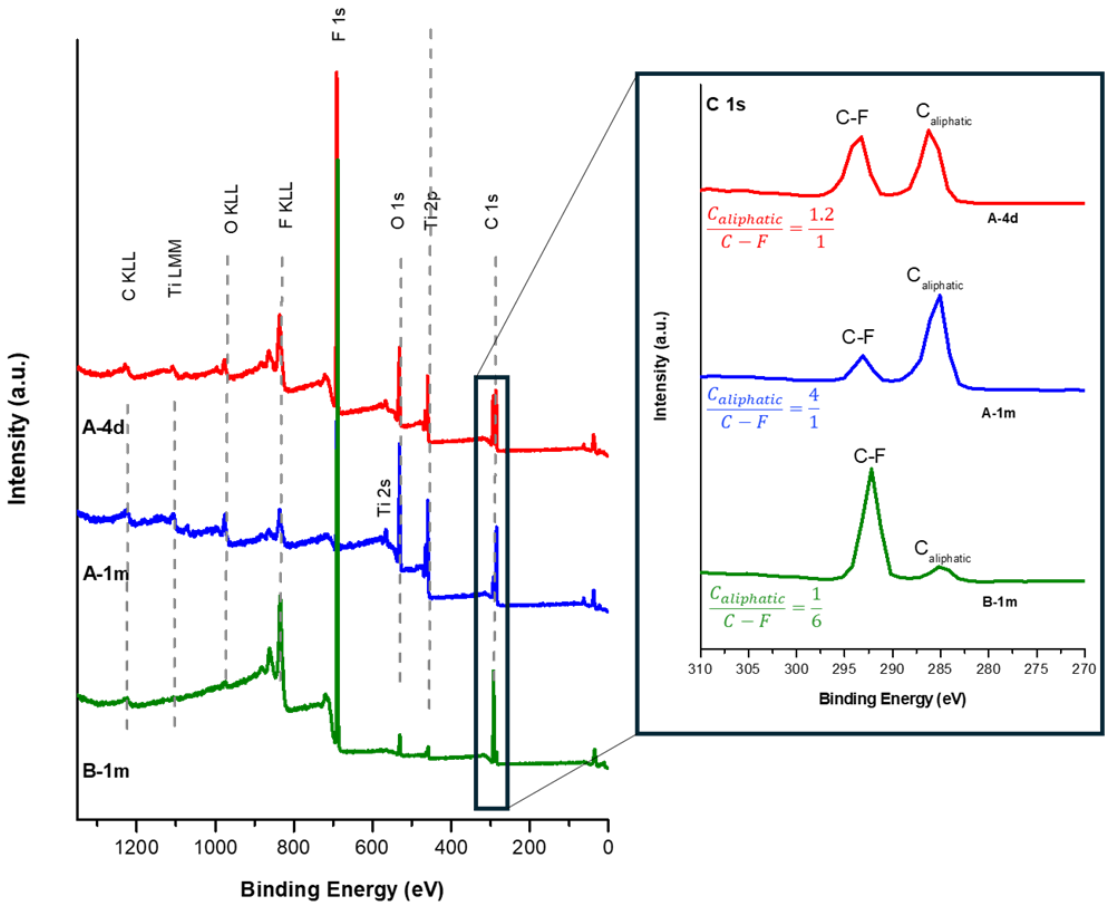

Figure 3.61. XPS survey spectra of the analysed samples. In the inset, a magnification of the C 1s region is shown, and the $R_C = C_{aliphatic}/C\text{-}F$ ratios are reported. X-ray source: Al ka.

The trend of the ratio (R_C) between the peak area of aliphatic carbon ($C_{aliphatic}$) and that of carbon linked to fluorine ($C_{C\text{-}F}$) provides intriguing indications. When LLDPE is absent, increasing the incubation time leads to an increase in R_C, confirming the progress of PTFE exfoliation and its subsequent deposition on the surface of T-*Abi*. However, at the same incubation time (1 month), in the presence of LLDPE, the R_C is much lower than that for T-*Abi*, indicating that the deposition of exfoliated PTFE on the surface of T-*Abi* is favored and, consequently, its degradation is disfavored in agreement with the GC-MS data.

In view of the above results, a mechanism for the physical exfoliation and related degradation phenomena is proposed, as illustrated in Scheme 3.2.

The role of water may be crucial in both processes. The permeation of water and ions through nanochannels in the PTFE coating may weaken its structure, facilitating the

surface erosion and consequent exfoliation [164,165]. The nanochannels and other structural defects formed in the PTFE coating may also allow the transport of reactive oxygen species (ROS) generated in aqueous solution to the inner layers of the material and the contact with ROS may assist the release and partial degradation of fluorinated organic components of the PTFE-coated stir bar.

The redox-active species could derive from two main sources: the activity of T-*Abi* under indirect daylight conditions and a tribocatalytic effect. Specifically, T-*Abi* has a hybrid structure with Ti-abietate charge transfer complexes that promote the adsorption of O_2, its reduction to superoxide radical, $O_2^{\bullet-}$, and the stabilization of the latter at surface sites, as previously proven for similar hybrid TiO_2 systems by experimental and computational methods [127,166]. In water medium, hydroxyl radicals, $OH^{\bullet}$, are generated from $O_2^{\bullet-}$ and these species concur to oxidative processes without continuous light irradiation [41,130]. The same mechanism is expected to occur in this case, under the same conditions that allowed the surface chemical degradation of LLDPE.

Additionally, a semiconductor such as TiO_2 may act as a tribocatalyst, exploiting mechanical energy to separate electron/hole pairs [167,168], and a tribocatalytic activity was reported even for bare PTFE particles derived from stir bars [169] due to its high triboelectric charge density [170,171]. Here, the friction between PTFE bars, TiO_2 particles and the glass beaker results in PTFE exfoliation and the chemical degradation of fluorinated compounds can be ruled out. On the contrary, in the presence of the hybrid TiO_2 material, T-*Abi*, the ROS are stabilized, and they are responsible for the presence of fluorinated by-products in solution.

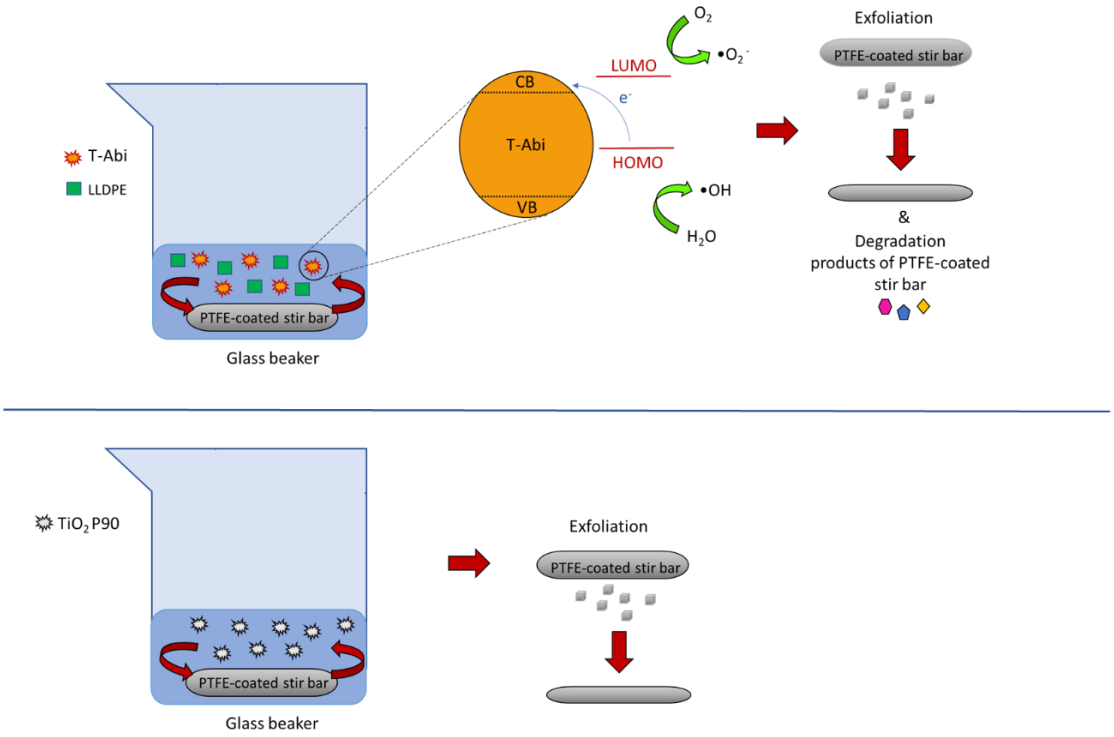

Scheme 3.2. Schematic drawing of the physical and chemical degradation of PTFE in the presence of T-*Abi* (upper panel) and of the physical degradation of PTFE in the presence of TiO_2 P90 (lower panel).

4. CONCLUSIONS

This doctoral thesis presents significant advancements in the eco-friendly degradation of MPs, addressing one of the most pressing environmental challenges of our time, the accumulation of plastic waste in the environment.

The core of this research focused on the development of hybrid materials, which combine semiconducting metal oxides, such as ZnO and TiO_2, with bio-waste materials like humic substances and rosin. These hybrid materials, synthesized by wet bottom-up techniques adopting a waste-to-wealth approach, demonstrated a significant photooxidation activity towards a few polymer targets, such as LLDPE, PLA, and PET, due to the ability to stabilize reactive oxygen species on their surfaces.

ZnO and TiO_2 nanoparticles doped and/or functionalized with humic substances, synthesized through solvothermal route, result photoactive under UVA and solar light illumination producing valuable morphological and structural changes in the target LLDPE and PLA polymer samples.

The development of a simple, green and sustainable sol-gel route enabled the utilization of a rosin bio-waste, mainly composed of abietic acid, without any costly and time-consuming chemical transformations, has been the most important result of this research. In the resulting TiO_2-abietate material, T-*Abi*, the bio-waste compound acts as ligand to Ti^{4+} ions forming a ligand-to-metal charge transfer complex, as predicted by DFT calculations and then assessed by XPS, FTIR and DRUV analyses. This complex plays a key role in the spontaneous generation of superoxide radical ions on the hybrid surface, without requiring any energy source. These radicals remain stable at indirect daylight and room temperature, as ascertained by EPR spectroscopy, which makes this material a powerful green tool for oxidative degradation processes.

An impressive degradation of LLDPE was observed after 1 month of exposure in a batch configuration under indirect daylight, as evidenced by the products revealed by GC-MS analysis and by chemical and structural modifications of the polymer surface.

The chemical characterization elucidates that LLDPE undergoes a secondary crystallization mechanism and a partial surface oxidation, including the break of polymer chains. The observed modifications, induced by the presence of the hybrid material without direct external energy inputs, allowed to propose an exemplificative degradation mechanism that differs from that reported in the literature for the photoinitiated oxidative degradation. The photoactivity of T-*Abi* under indirect daylight conditions has started to test also towards PET target polymer obtaining extraordinary preliminary results considering both the chemical inertness of PET and the mild conditions in which the degradation products were achieved.

This novel approach represents a promising method for tackling microplastic pollution, since the degradation process occurs under mild and environmentally friendly conditions, offering a real advantage over conventional energy-intensive methods. This is a crucial step forward, as traditional methods of plastic degradation often require high energy inputs, chemicals, or extreme environmental conditions. By utilizing bio-waste materials, this research contributes to the development of low-cost, eco-friendly alternatives for plastic waste remediation.

On the other hand, the extraordinary oxidative activity of T-*Abi* under indirect daylight conditions was proved by the chemical surface degradation of PTFE magnetic stir bars that was achieved for the first time.

Starting from the promising results achieved in this PhD project, the following future perspectives should be considered. The scaling-up of the hybrid materials for real-world applications is crucial. The current synthesis methods, though effective on lab-scale, need to be optimized for large-scale production to ensure the materials can be employed in environmental remediation effectively.
Additionally, research should explore the long-term stability and efficiency of these materials in complex environmental conditions, where factors like temperature, humidity, and pollutant concentration may affect performance.
Moreover, the reuse of the degradation by-products converting them in value-added molecules is another promising future perspective to optimize the whole polymer degradation process making it a close loop cycle.

This approach would not only address the environmental issue of MPS pollution but also contribute to the creation of a circular economy model for plastic waste management.

In conclusion, this doctoral thesis presents a promising approach for the degradation of MPs exploiting hybrid materials derived from bio-waste. The findings provide a sustainable, cost-effective solution to one of the most critical environmental problems. The integration of circular economy principles into the research highlights the potential for these hybrid materials to contribute to both environmental remediation and the promotion of a more sustainable, resource-efficient future.

5. EXPERIMENTAL SECTION

5.1 Physicochemical characterization of the synthesized hybrid materials

The hybrid materials were characterized by a series of analytical techniques to investigate their structural, physicochemical and functional properties. Here the instruments used, the measurement conditions and information about the elaboration of collected data are reported. The characterization procedures of polymeric samples are described in the next section.

5.1.1 Transmission Electron Microscopy (TEM)

Transmission electron microscopy (TEM) was carried out to assess the morphology of bare and hybrid metal-oxide nanoparticles. A small amount of each nanoparticles suspension was deposited onto copper meshes and examined in bright field mode on an FEI TecnaiG12 Spirit Twin TEM running at 120kV acceleration voltage.
The specific surface area (S_{BET}) was evaluated by N_2 adsorption at -196 °C starting from P/P0 = 5 × 10-6 using a Quantachrome Autosorb-1C instrument (Quantachrome, Anton Paar Italia, Rivoli, Italy), after degassing the samples at 120 °C for 4 h.

5.1.2 Scanning Electron Microscope (SEM)

The T-*Abi* surface morphology was studied by using a field emission scanning electron microscope (mod. FEI QUANTA 200F). Micrographs were acquired on a Tescan Mira3 system using a 10 kV acceleration voltage.

5.1.3 X-Ray Diffraction (XRD)

The amorphous nature and crystallizing phases in the structure of the samples were ascertained by X-ray Diffraction (XRD) carried out in the laboratory of diffractometry of the Department of Chemical, Materials and Production Engineering (University of Naples Federico II) with a Malvern Panalytical diffractometer (Malvern, UK) with a nickel filter and Cu Kα radiation. Giuseppe Mocci is acknowledged for the measurements.

The average crystal size (τ) was evaluated through the Scherrer equation:

$$\tau = K\lambda/\beta \cos\theta \qquad (5.1)$$

where K is a dimensionless shape factor (assumed to be K=0.9), λ is the X-ray radiation wavelength, β is the width at half the maximum intensity (FWHM) of the main diffraction peak (in radians) and θ is the Bragg's angle.

5.1.4 Thermogravimetric – Differential Thermal Analysis (TG-DTA)

To investigate the thermal stability of the synthesized materials, Thermogravimetric (TG) and Differential Thermal (DTA) analyses were conducted at the Department of Chemical, Materials and Production Engineering (University of Naples Federico II), using a TA Instrument simultaneous thermo-analyzer SDT Q600 (TA instrument, New Castle, DE, USA).

To evaluate the weight loss of hybrid HAs-doped/ZnO, HS/ZnO and HS/TiO_2 and, therefore, HA and HS content in hybrid nanoparticles, TGA analyses were carried out according to the Standard Test Methods for Proximate Analysis (ASTM D 5142-02, 1994) [80,81].

To evaluate the weight loss of T-*Abi*, about 10 mg of the sample was placed in a platinum pan and tested in inert atmosphere. The analyses were carried out in the temperature range between 25 °C and 900 °C with a heating rate of 10°C/min.

5.1.5 Fourier-Transform Infrared Spectroscopy (FTIR)

The chemical structure of the synthesized hybrid materials was studied by Fourier Transform Infrared (FTIR) spectroscopy by using a Nicolet Instrument Nexus model (Thermo Scientific, Waltham, MA, USA) that was equipped with a DTGS KBr (deuterated triglycine sulfate with potassium bromide windows) detector. The measurements were carried out at the Department of Chemical, Materials and Production Engineering (University of Naples Federico II). The FTIR spectra were recorded at room temperature in the 4000-400 cm^{-1} range at a resolution of 2 cm^{-1} on pressed disks of powders that had been previously diluted in KBr (1 wt%). The FTIR spectrum of each sample was corrected based on a spectrum of blank KBr.

5.1.6 X-Ray Photoelectron Spectroscopy (XPS)

XPS spectroscopy allowed the identification of the elements present on the surface of the materials, provided their speciation and their quantitative analysis. The measurements were performed on selected samples by the group of Prof. Antonella Rossi and Prof. Marzia Fantuzzi at the University of Cagliari, Department of Chemical and Geological Sciences. XPS analyses were performed on powdered samples mounted on copper bi-adhesive tape and analyzed by a Theta Probe spectrometer (Thermo Fisher Scientific) equipped with an Al Ka X-ray source (hn = 1486.6 eV). A nominal 400 mm spot size (100.5 W) was used for acquiring the spectra. Survey and high-resolution spectra were obtained in fixed analyzer transmission (FAT) mode and the pass energy was set at 200 eV and 100 eV for the wide scan and narrow (high resolution spectra) scan spectra, respectively. Under these conditions, the full width at half-maximum of Ag $3d_{5/2}$ peak acquired on a sputtered silver sample was 0.96 eV. To verify the linearity of the binding energy scale, a periodic calibration was performed following ISO 15472:2010. A flood gun neutralizer was used to compensate for sample charging. The spectra were acquired in the standard lens mode, and, under this condition, the emission angle was 53°. For each

sample, three different areas were analyzed. The total duration of the acquisition was 30 minutes in each analyzed area. The binding energy scale was referenced to the aliphatic carbon component at 285.0 eV. XPS spectra were processed by CasaXPS software (version 2.3.24PR1.0) [172]. An iterated Shirley – Sherwood background was subtracted before curve fitting. The product of Gaussian and Lorentzian functions was used as model functions. Quantitative composition was calculated using the first-principle method [173] under the assumption that the samples were homogeneous in composition.

5.1.7 Diffuse Reflectance UV-visible spectroscopy (DRUV-vis)

The optical properties of the synthesized hybrid materials were investigated by performing Diffuse-Reflectance UV-vis (DRUV) measurements with a UV-2600i UV-VIS spectrophotometer, 230V (Shimadzu, Milan, Italy), equipped with an integrating sphere ISR-2600Plus operating in a wavelength range of 220 - 1400 nm at the Department of Chemical Sciences of the University of Naples Federico II. Barium sulfate was used as a reflectance standard. The measured intensity was expressed as the value of the Kubelka-Munk function, F(R), while the direct band-gap energy value was evaluated according to the Tauc-plot linearization.

5.1.8 Electron Paramagnetic Resonance (EPR) spectroscopy

Electron paramagnetic resonance (EPR) spectroscopy was exploited to check the presence of radical species on the studied materials. The analyses were performed at the Department of Chemical Sciences of the University of Naples Federico II.

The spectra were acquired at room temperature with an X-band (9 GHz) Bruker Elexys E-500 spectrometer (Bruker, Rheinstetten, Germany), collecting 16 scans, selecting the following instrumental settings: sweep width, 140 G; resolution, 1024 points; modulation frequency, 100 kHz; modulation amplitude, 1.0 G; time constant, 20.5 ms; attenuation, 10 dB. The g-factor values were evaluated by means of an internal standard, Mn^{2+}-doped MgO. EPR spin-trapping experiments were also performed to detect ROS generation in aqueous environment.

The following procedure was adopted for HAs-doped/ZnO: a specific amount of a stock aqueous solution of 5,5-dimethyl-1-pyrroline-1-oxide (DMPO) spin-trap was added in 1mL of the aqueous suspension of nanoparticles (both bare ZnO and HAs-doped/ZnO, alternatively) at a concentration of 2mg×mL^{-1}, with the aim to have a final spin-trap concentration of 20mM. After 10 min from the dispersion preparation, the mixtures of ZnO-based nanoparticles and DMPO were exposed for 10 minutes to the UVA/light lamp used for the photocatalytic experiments before to be centrifuged to recover the supernatants, which were independently placed in a capillary to be analysed by EPR. The spectra were recorded with an attenuation of 15 dB and 64 scans were accumulated.
The following procedure was adopted for T-*Abi*: a specific amount of 5,5-dimethyl-1-pyrroline-1-oxide (DMPO) spin-trap (20 mmol/L) was added to an aqueous suspension of T-Abi at a concentration of 1 mg/mL kept in dark. After 10 min from the dispersion preparation, the sample was centrifuged to recover the supernatant, which was placed in a capillary to be analyzed by EPR. The spectrum was recorded with an attenuation of 15 dB and 64 scans were accumulated.

5.2 Characterization of the polymeric samples

5.2.1 Scanning electron microscopy (SEM)

The surface morphologies of LLDPE and PLA slices before and after photodegradation were analysed by means of Scanning electron microscopy (SEM) using a FEI Quanta 200 FEG SEM (Eindhoven, The Netherlands). Small specimens were cut from the middle of the sample and mounted on aluminium stubs by means of carbon adhesive disks and coated with a thin layer (about 10 nm thick) of an Au-Pd alloy by means of a sputter coating system (Emitech K575, Quorum Technologies LTD, UK).

5.2.2 Attenuated total reflectance Fourier transform infrared spectroscopy (ATR-FTIR)

Attenuated total reflectance Fourier transform infrared spectroscopy (ATR-FTIR) analysis on LLDPE and PLA (bare and treated with the synthesized materials) was carried out for finding out any alterations in the chemical structure. The samples were placed on a ZnSe crystal, and the ATR-FTIR absorption spectra were recorded in the 4000-400 cm^{-1} range with 8 cm^{-1} spectral resolution. The spectrum of each sample was corrected for that of blank, which was carried out in air.

ATR-FTIR spectra allowed the estimation of the degradation efficiency of LLDPE and PLA through the Carbonyl Index (C.I.) method [156].

The C.I. of LLDPE was calculated as the ratio between the absorbance of the carbonyl groups (1700-1500 cm^{-1}) and the absorbance of the reference peak of CH_2 and CH_3 at (1480-1420 cm^{-1}) [174]:

$$\text{Carbonyl Index (C. I.)} = \frac{\text{Absorption of carbonyl species } (1700-1500\ \text{cm}^{-1})}{\text{Absorption of } CH_2,CH_3\ (1480-1420\ \text{cm}^{-1})} \quad (5.2)$$

The C.I. of PLA was estimated as described in equation (eq. 5.3)[80,81]:

$$\text{Carbonyl Index (C. I.)} = \frac{\text{Absorption of carbonyl species } (1700-1500\ \text{cm}^{-1})}{\text{Absorption of reference peak } (1130\ \text{cm}^{-1})} \quad (5.3)$$

5.2.3 X-Ray Diffraction (XRD)

XRD analysis on LLDPE and PLA was performed as previously described in Section 5.1.1, to check the possible change in crystalline structure of each polymer following the treatment with the synthesized materials.

The crystallinity index (X_c) is a quantitative indicator of crystallinity, and it was calculated according to:

$$\text{Crystallinity index, } X_c\ (\%) = \frac{\text{Area of all the crystalline peaks}}{\text{Area of all the crystalline and amorphous peaks}} \quad (5.4)$$

5.2.4 Differential Scanning Calorimetry (DSC) analysis

Thermal properties of the samples were determined by performing a Differential Scanning Calorimetry (DSC) analysis.

DSC measurements of LLDPE and PLA slices treated with hybrid nanoparticles were performed using a TAQ2000differential scanning calorimeter equipped with RCS-90 cooling unit (TA Instrument, New Castle, DE, USA). The instrument was calibrated in temperature and energy with pure indium. About 5 mg of the samples were sealed into a Tzero® aluminium pan. The thermal cycle was from -50 to 200 °C at 10 °C/min. High-purity nitrogen gas was fluxed at 20 mL/min during all measurements. The melting enthalpy was determined by integrating the melting peak using the software TA Universal Analysis2000, Version 4.7 A. The crystallinity of the samples was calculated by dividing the sample melting enthalpy by the melting enthalpy of the fully crystalline polymer that was 93.6 J/g for PLA [175], and 293 J/g for LDPE [176]. TGA measurements were carried out using a Perkin Elmer Pyris 1 analyser. About 5 mg of each sample were placed in a platinum open pan and heated from 50 °C to 800 °C at 10 °C/min. High purity nitrogen was fluxed through the furnace at a flow rate of 40 mL/min. EGA analysis was performed using hyphenated TGA/FTIR system. The TGA, Perkin Elmer, Pyris 1, was interfaced with FTIR spectrometer (Perkin-Elmer, Frontier). Evolved gases were piped (gas flow: 65 mL min-1) via pressurized heated-transfer line, and continuously analysed by the FTIR with a thermo-stated conventional gas cell. The temperatures of the transfer line and gas cell were both set at 270 °C. Time/temperature-resolved spectra were acquired in the

4000-600 cm-1 wavenumber range (resolution: 4 cm-1) and analysed with the Spectrum software (Perkin-Elmer).

DSC measurements of LLDPE MPs treated with T-*Abi* were carried out on polymer samples by using the same TA instrument described above in Section 5.1.2 for TG-DTA. The melting enthalpy was determined by integrating the melting peak using the software OriginPro by OriginLab Corporation. The degree of crystallization of the samples was calculated by dividing ΔH_m (i.e., the sample melting enthalpy), by ΔH_0 (i.e., the theoretical value of the melting enthalpy of 100% crystalline LDPE):

$$\text{Crystallinity index, } X_c\ (\%) = \frac{\Delta H_m}{\Delta H_0}(\%) \tag{5.5}$$

The value ΔH_0 = 293 J/g was used in calculations [176].

5.3 Characterization of the aqueous suspensions

The degradation intermediates of LLDPE and PET treated with T-*Abi* were identified by gas chromatography-mass spectrometry (GC-MS) according to the standard spectra of the NIST 1.7 library data. Prior to GC-MS analysis, the lyophilized samples, obtained after 1 month of incubation of LLDPE and PET with T-*Abi*, were extracted by using three different organic solvents, toluene, hexane and chloroform. The same experimental procedure was performed for the controls, obtained after the same incubation time (1 month) but without T-*Abi*.

All the samples were analysed on a Perkin Elmer AutoSystemTMXL GC, equipped with a Programmed Temperature Split/Splitless injector; a Restek Rtx-5MS capillary column (5% diphenyl-95% dimethylpolysiloxane, 30 m × 0.25 mm, 0.25 μm) and a Perkin-Elmer Turbo Mass Goldmass-spectrometer. The initial temperature of the column oven was held at 40 °C for 5 min, and then heated up to 285 °C at a ramping rate of 5 °C/min. Helium was used as carrier gas. Mass spectrometric detection was operated with 70 eV electron impact (EI) mode at an ionization current of 50 μA and an ion source temperature of 250 °C. The mass spectra were recorded in a full scan mode (m/z 50-1000) for qualitative analysis.

Bibliography

[1] P.G.C. Nayanathara Thathsarani Pilapitiya, A.S. Ratnayake, The world of plastic waste: A review, Clean. Mater. 11 (2024) 100220. https://doi.org/10.1016/j.clema.2024.100220.

[2] S. Sharma, S. Basu, N.P. Shetti, M.N. Nadagouda, T.M. Aminabhavi, Microplastics in the environment: Occurrence, perils, and eradication, Chem. Eng. J. 408 (2021) 127317. https://doi.org/10.1016/j.cej.2020.127317.

[3] J. Chen, J. Wu, P.C. Sherrell, J. Chen, H. Wang, W. xian Zhang, J. Yang, How to Build a Microplastics-Free Environment: Strategies for Microplastics Degradation and Plastics Recycling, Adv. Sci. 9 (2022) 1–36. https://doi.org/10.1002/advs.202103764.

[4] S. Miri, R. Saini, S.M. Davoodi, R. Pulicharla, S.K. Brar, S. Magdouli, Biodegradation of microplastics: Better late than never, Chemosphere. 286 (2022) 131670. https://doi.org/10.1016/j.chemosphere.2021.131670.

[5] G. Zhou, H. Xu, H. Song, J. Yi, X. Wang, Z. Chen, X. Zhu, Photocatalysis toward Microplastics Conversion: A Critical Review, ACS Catal. . 14 (2024) 8694–8719. https://doi.org/10.1021/acscatal.4c01449.

[6] M.C. Ariza-Tarazona, J.F. Villarreal-Chiu, J.M. Hernández-López, J. Rivera De la Rosa, V. Barbieri, C. Siligardi, E.I. Cedillo-González, Microplastic pollution reduction by a carbon and nitrogen-doped TiO2: Effect of pH and temperature in the photocatalytic degradation process, J. Hazard. Mater. 395 (2020) 122632. https://doi.org/10.1016/j.jhazmat.2020.122632.

[7] a K. Van Der Vegt, A.K. van der Vegt, From Polymers to Plastics, (2002) 268. http://www.vssd.nl/hlf/m008.htm%5Cnhttp://www.vssd.nl/hlf/m028.htm.

[8] M.H. Rahman, P.R. Bhoi, An overview of non-biodegradable bioplastics, J. Clean. Prod. 294 (2021). https://doi.org/10.1016/j.jclepro.2021.126218.

[9] A. Shrivastava, Introduction to Plastics Engineering, Introd. to Plast. Eng. (2018) 1–16. https://doi.org/10.1016/b978-0-323-39500-7.00001-0.

[10] E. Analysis, The Circular Economy for Plastics About the report, (2024).

[11] Tawfik Abdo Saleh, Chapter 3 - Polymer science and polymerization methods toward hybrid materials, in: Tawfik Abdo Saleh (Ed.), Polym. Hybrid Mater. Nanocomposites, William Andrew Publishing, 2021: pp. 59–103. https://doi.org/https://doi.org/10.1016/B978-0-12-813294-4.00004-2.

[12] M. Gilbert, Plastics Materials: Introduction and Historical Development, Brydson's Plast. Mater. Eighth Ed. (2016) 2–18. https://doi.org/10.1016/B978-0-323-35824-8.00001-3.

[13] S. Kumari, A. Rao, M. Kaur, G. Dhania, Petroleum-Based Plastics Versus Bio-Based Plastics: A Review, Nat. Environ. Pollut. Technol. 22 (2023) 1111–1124. https://doi.org/10.46488/NEPT.2023.v22i03.003.

[14] L. Ständecke, L. Gockel, M. Busch, Mixing in High-Pressure Polymerization Reactors: A Combined Experimental and Modeling Approach, Chemie-Ingenieur-Technik. 95 (2023) 761–766. https://doi.org/10.1002/cite.202200218.

[15] G.P. Francesco Guzzi, Elvira Parrotta, Simona Zaccone, Tania Limongi, Giovanni Cuda, Chapter 4 - Materials, in: P.L. Gerardo Perozziello, Ulrich Krühne (Ed.), Microfluid. Cell. Appl., 2023: pp. 119–187. https://doi.org/https://doi.org/10.1016/B978-0-12-822482-3.00005-1.

[16] https://www.european-bioplastics.org/, (n.d.).

[17] Y. Zhong, P. Godwin, Y. Jin, H. Xiao, Biodegradable polymers and green-based antimicrobial packaging materials: A mini-review, Adv. Ind. Eng. Polym. Res. 3 (2020) 27–35. https://doi.org/10.1016/j.aiepr.2019.11.002.

[18] T. Abate, C. Amabile, R. Muñoz, S. Chianese, D. Musmarra, Polyhydroxyalkanoate recovery overview: properties, characterizations, and extraction strategies, Chemosphere. 356 (2024). https://doi.org/10.1016/j.chemosphere.2024.141950.

[19] R. Sirohi, J. Prakash Pandey, V. Kumar Gaur, E. Gnansounou, R. Sindhu, Critical overview of biomass feedstocks as sustainable substrates for the production of polyhydroxybutyrate (PHB), Bioresour. Technol. 311 (2020) 123536.

https://doi.org/10.1016/j.biortech.2020.123536.

[20] P.N. Angnunavuri, F. Attiogbe, B. Mensah, Particulate plastics in drinking water and potential human health effects: Current knowledge for management of freshwater plastic materials in Africa, Environ. Pollut. 316 (2023) 120714. https://doi.org/10.1016/j.envpol.2022.120714.

[21] A.A. Horton, A. Walton, D.J. Spurgeon, E. Lahive, C. Svendsen, Microplastics in freshwater and terrestrial environments: Evaluating the current understanding to identify the knowledge gaps and future research priorities, Sci. Total Environ. 586 (2017) 127–141. https://doi.org/10.1016/j.scitotenv.2017.01.190.

[22] M. Liu, S. Lu, Y. Song, L. Lei, J. Hu, W. Lv, W. Zhou, C. Cao, H. Shi, X. Yang, D. He, Microplastic and mesoplastic pollution in farmland soils in suburbs of Shanghai, China, Environ. Pollut. 242 (2018) 855–862. https://doi.org/10.1016/j.envpol.2018.07.051.

[23] D. Zhou, J. Chen, J. Wu, J. Yang, H. Wang, Biodegradation and catalytic-chemical degradation strategies to mitigate microplastic pollution, Sustain. Mater. Technol. 28 (2021) e00251. https://doi.org/10.1016/j.susmat.2021.e00251.

[24] J. Zhao, W. Ran, J. Teng, Y. Liu, H. Liu, X. Yin, R. Cao, Q. Wang, Microplastic pollution in sediments from the Bohai Sea and the Yellow Sea, China, Sci. Total Environ. 640–641 (2018) 637–645. https://doi.org/10.1016/j.scitotenv.2018.05.346.

[25] Y. Zhang, S. Kang, S. Allen, D. Allen, T. Gao, M. Sillanpää, Atmospheric microplastics: A review on current status and perspectives, Earth-Science Rev. 203 (2020) 103118. https://doi.org/10.1016/j.earscirev.2020.103118.

[26] S. Wang, H. Chen, X. Zhou, Y. Tian, C. Lin, W. Wang, K. Zhou, Y. Zhang, H. Lin, Microplastic abundance, distribution and composition in the mid-west Pacific Ocean, Environ. Pollut. 264 (2020) 114125. https://doi.org/10.1016/j.envpol.2020.114125.

[27] H. Deng, R. Wei, W. Luo, L. Hu, B. Li, Y. Di, H. Shi, Microplastic pollution in water and sediment in a textile industrial area, Environ. Pollut. 258 (2020) 113658.

https://doi.org/10.1016/j.envpol.2019.113658.

[28] B. Zhou, J. Wang, H. Zhang, H. Shi, Y. Fei, S. Huang, Y. Tong, D. Wen, Y. Luo, D. Barceló, Microplastics in agricultural soils on the coastal plain of Hangzhou Bay, east China: Multiple sources other than plastic mulching film, J. Hazard. Mater. 388 (2020) 121814. https://doi.org/10.1016/j.jhazmat.2019.121814.

[29] B. Jiang, A. Kauffman, L. Li, W. McFee, B. Cai, J. Weinstein, J. Lead, S. Chatterjee, G. Scott, S. Xiao, Impactos en la salud de la contaminación ambiental de micro y nanoplásticos: una revisión, Environ. Health Prev. Med. 25 (2020) 1–15.

[30] R. Dris, J. Gasperi, C. Mirande, C. Mandin, M. Guerrouache, V. Langlois, B. Tassin, A first overview of textile fibers, including microplastics, in indoor and outdoor environments, Environ. Pollut. 221 (2017) 453–458. https://doi.org/10.1016/j.envpol.2016.12.013.

[31] M. Klein, E.K. Fischer, Microplastic abundance in atmospheric deposition within the Metropolitan area of Hamburg, Germany, Sci. Total Environ. 685 (2019) 96–103. https://doi.org/10.1016/j.scitotenv.2019.05.405.

[32] A.I. Osman, M. Hosny, A.S. Eltaweil, S. Omar, A.M. Elgarahy, M. Farghali, P.S. Yap, Y.S. Wu, S. Nagandran, K. Batumalaie, S.C.B. Gopinath, O.D. John, M. Sekar, T. Saikia, P. Karunanithi, M.H.M. Hatta, K.A. Akinyede, Microplastic sources, formation, toxicity and remediation: a review, Springer International Publishing, 2023. https://doi.org/10.1007/s10311-023-01593-3.

[33] K. Duis, A. Coors, Microplastics in the aquatic and terrestrial environment: sources (with a specific focus on personal care products), fate and effects, Environ. Sci. Eur. 28 (2016) 1–25. https://doi.org/10.1186/s12302-015-0069-y.

[34] Y. He, X. Deng, L. Jiang, L. Hao, Y. Shi, M. Lyu, L. Zhang, S. Wang, Current advances, challenges and strategies for enhancing the biodegradation of plastic waste, Sci. Total Environ. 906 (2024) 167850. https://doi.org/10.1016/j.scitotenv.2023.167850.

[35] L. Liu, M. Xu, Y. Ye, B. Zhang, On the degradation of (micro)plastics:

Degradation methods, influencing factors, environmental impacts, Sci. Total Environ. 806 (2022) 151312. https://doi.org/10.1016/j.scitotenv.2021.151312.

[36] A. Babu Ponnusami, S. Sinha, H. Ashokan, M. V Paul, S.P. Hariharan, J. Arun, K.P. Gopinath, Q. Hoang Le, A. Pugazhendhi, Advanced oxidation process (AOP) combined biological process for wastewater treatment: A review on advancements, feasibility and practicability of combined techniques, Environ. Res. 237 (2023) 116944. https://doi.org/10.1016/j.envres.2023.116944.

[37] K. Rajeshwar, Solar energy conversion and environmental remediation using inorganic semiconductor-liquid interfaces: The road traveled and the way forward, J. Phys. Chem. Lett. 2 (2011) 1301–1309. https://doi.org/10.1021/jz200396h.

[38] M.P. Rayaroth, C.T. Aravindakumar, N.S. Shah, G. Boczkaj, Advanced oxidation processes (AOPs) based wastewater treatment - unexpected nitration side reactions - a serious environmental issue: A review, Chem. Eng. J. 430 (2022) 133002. https://doi.org/10.1016/j.cej.2021.133002.

[39] M. Priyadarshini, I. Das, M.M. Ghangrekar, L. Blaney, Advanced oxidation processes: Performance, advantages, and scale-up of emerging technologies, J. Environ. Manage. 316 (2022) 115295. https://doi.org/10.1016/j.jenvman.2022.115295.

[40] K. Krumova; G. Cosa, Overview of Reactive Oxygen Species, in: Singlet Oxyg. Appl. Biosci. Nanosci., 2016: pp. 1–21. https://doi.org/10.1039/9781782620389-00001.

[41] D. Pirozzi, C. Imparato, G. D'Errico, G. Vitiello, A. Aronne, F. Sannino, Three-year lifetime and regeneration of superoxide radicals on the surface of hybrid TiO2 materials exposed to air, J. Hazard. Mater. 387 (2020). https://doi.org/10.1016/j.jhazmat.2019.121716.

[42] F. Sannino, P. Pernice, C. Imparato, A. Aronne, G. D'Errico, L. Minieri, M. Perfetti, D. Pirozzi, Hybrid TiO2-acetylacetonate amorphous gel-derived material with stably adsorbed superoxide radical active in oxidative degradation of organic pollutants, RSC Adv. 5 (2015) 93831–93839. https://doi.org/10.1039/c5ra21176j.

[43] K. Roy, V.S. Moholkar, Sulfadiazine degradation using hybrid AOP of heterogeneous Fenton/persulfate system coupled with hydrodynamic cavitation, Chem. Eng. J. 386 (2020) 121294. https://doi.org/10.1016/j.cej.2019.03.170.

[44] S.P.M. Menacherry, U.K. Aravind, C.T. Aravindakumar, Critical review on the role of mass spectrometry in the AOP based degradation of contaminants of emerging concern (CECs) in water, J. Environ. Chem. Eng. 10 (2022) 108155. https://doi.org/10.1016/j.jece.2022.108155.

[45] T. Jiang, B. Wang, B. Gao, N. Cheng, Q. Feng, M. Chen, S. Wang, Degradation of organic pollutants from water by biochar-assisted advanced oxidation processes: Mechanisms and applications, J. Hazard. Mater. 442 (2023) 130075. https://doi.org/10.1016/j.jhazmat.2022.130075.

[46] F. Banat, S. Al-Asheh, M. Al-Rawashdeh, M. Nusair, Photodegradation of methylene blue dye by the UV/H2 O2 and UV/acetone oxidation processes, Desalination. 181 (2005) 225–232. https://doi.org/10.1016/j.desal.2005.04.005.

[47] Y. Chen, H. Chen, J. Li, L. Xiao, Rapid and efficient activated sludge treatment by electro-Fenton oxidation, Water Res. 152 (2019) 181–190. https://doi.org/10.1016/j.watres.2018.12.035.

[48] J. chao Wang, H. Wang, L. luo Huang, C. qing Wang, Surface treatment with Fenton for separation of acrylonitrile-butadiene-styrene and polyvinylchloride waste plastics by flotation, Waste Manag. 67 (2017) 20–26. https://doi.org/10.1016/j.wasman.2017.05.009.

[49] Z. Yang, Y. Li, G. Zhang, Degradation of microplastic in water by advanced oxidation processes, Chemosphere. 357 (2024) 141939. https://doi.org/10.1016/j.chemosphere.2024.141939.

[50] S. Wang, A Comparative study of Fenton and Fenton-like reaction kinetics in decolourisation of wastewater, Dye. Pigment. 76 (2008) 714–720. https://doi.org/10.1016/j.dyepig.2007.01.012.

[51] S.A. Walling, W. Um, C.L. Corkhill, N.C. Hyatt, Fenton and Fenton-like wet oxidation for degradation and destruction of organic radioactive wastes, Npj Mater.

Degrad. 5 (2021) 1–20. https://doi.org/10.1038/s41529-021-00192-3.

[52] S. Ziembowicz, M. Kida, Limitations and future directions of application of the Fenton-like process in micropollutants degradation in water and wastewater treatment: A critical review, Chemosphere. 296 (2022). https://doi.org/10.1016/j.chemosphere.2022.134041.

[53] P. Liu, L. Qian, H. Wang, X. Zhan, K. Lu, C. Gu, S. Gao, New Insights into the Aging Behavior of Microplastics Accelerated by Advanced Oxidation Processes, Environ. Sci. Technol. 53 (2019) 3579–3588. https://doi.org/10.1021/acs.est.9b00493.

[54] B. Liu, Q. Jiang, Z. Qiu, L. Liu, R. Wei, X. Zhang, H. Xu, Process analysis of microplastic degradation using activated PMS and Fenton reagents, Chemosphere. 298 (2022) 134220. https://doi.org/10.1016/j.chemosphere.2022.134220.

[55] D. Ortiz, M. Munoz, J. Nieto-Sandoval, C. Romera-Castillo, Z.M. de Pedro, J.A. Casas, Insights into the degradation of microplastics by Fenton oxidation: From surface modification to mineralization, Chemosphere. 309 (2022) 136809. https://doi.org/10.1016/j.chemosphere.2022.136809.

[56] S. Ghatge, Y. Yang, Y. Ko, Y. Yoon, J.H. Ahn, J.J. Kim, H.G. Hur, Degradation of sulfonated polyethylene by a bio-photo-fenton approach usingglucose oxidase immobilized on titanium dioxide, J. Hazard. Mater. 423 (2022) 127067. https://doi.org/10.1016/j.jhazmat.2021.127067.

[57] A.C. Vivekanand, S. Mohapatra, V.K. Tyagi, Microplastics in aquatic environment: Challenges and perspectives, Chemosphere. 282 (2021) 131151. https://doi.org/10.1016/j.chemosphere.2021.131151.

[58] J. Ge, Z. Zhang, Z. Ouyang, M. Shang, P. Liu, H. Li, X. Guo, Photocatalytic degradation of (micro)plastics using TiO2-based and other catalysts: Properties, influencing factor, and mechanism, Environ. Res. 209 (2022) 112729. https://doi.org/10.1016/j.envres.2022.112729.

[59] W. Li, W. Zhao, H. Zhu, Z.J. Li, W. Wang, State of the art in the photochemical degradation of (micro)plastics: from fundamental principles to catalysts and

applications, J. Mater. Chem. A. 11 (2023) 2503–2527. https://doi.org/10.1039/d2ta09523h.

[60] M. Surana, D.S. Pattanayak, V. Yadav, V.K. Singh, D. Pal, An insight decipher on photocatalytic degradation of microplastics: Mechanism, limitations, and future outlook, Environ. Res. 247 (2024) 118268. https://doi.org/10.1016/j.envres.2024.118268.

[61] R. Jiang, G. Lu, Z. Yan, J. Liu, D. Wu, Y. Wang, Microplastic degradation by hydroxy-rich bismuth oxychloride, J. Hazard. Mater. 405 (2021) 124247. https://doi.org/10.1016/j.jhazmat.2020.124247.

[62] X. Wang, Z. Zhu, J. Jiang, R. Li, J. Xiong, Preparation of heterojunction C3N4/WO3 photocatalyst for degradation of microplastics in water, Chemosphere. 337 (2023) 139206. https://doi.org/10.1016/j.chemosphere.2023.139206.

[63] Y. Zhong, B. Zhang, Z. Zhu, G. Wang, X. Mei, Y. Fang, W. Lu, Photocatalytic-Driven Self-Degradation of Polyester Microplastics Under Solar Light, J. Polym. Environ. 31 (2023) 2415–2423. https://doi.org/10.1007/s10924-023-02763-8.

[64] I. Nabi, A.U.R. Bacha, F. Ahmad, L. Zhang, Application of titanium dioxide for the photocatalytic degradation of macro- and micro-plastics: A review, J. Environ. Chem. Eng. 9 (2021) 105964. https://doi.org/10.1016/j.jece.2021.105964.

[65] F. Dong, S. Guo, H. Wang, X. Li, Z. Wu, Enhancement of the visible light photocatalytic activity of C-doped Tio2 nanomaterials prepared by a green synthetic approach, J. Phys. Chem. C. 115 (2011) 13285–13292. https://doi.org/10.1021/jp111916q.

[66] I. Nabi, A.U.R. Bacha, K. Li, H. Cheng, T. Wang, Y. Liu, S. Ajmal, Y. Yang, Y. Feng, L. Zhang, Complete Photocatalytic Mineralization of Microplastic on TiO2 Nanoparticle Film, IScience. 23 (2020) 101326. https://doi.org/10.1016/j.isci.2020.101326.

[67] K. Qi, B. Cheng, J. Yu, W. Ho, Review on the improvement of the photocatalytic and antibacterial activities of ZnO, J. Alloys Compd. 727 (2017) 792–820. https://doi.org/10.1016/j.jallcom.2017.08.142.

[68] T.S. Tofa, K.L. Kunjali, S. Paul, J. Dutta, Visible light photocatalytic degradation of microplastic residues with zinc oxide nanorods, Environ. Chem. Lett. 17 (2019) 1341–1346. https://doi.org/10.1007/s10311-019-00859-z.

[69] A. Uheida, H.G. Mejía, M. Abdel-Rehim, W. Hamd, J. Dutta, Visible light photocatalytic degradation of polypropylene microplastics in a continuous water flow system, J. Hazard. Mater. 406 (2021) 124299. https://doi.org/10.1016/j.jhazmat.2020.124299.

[70] P. Praus, Photoreforming for microplastics recycling: A critical review, J. Environ. Chem. Eng. 12 (2024) 112525. https://doi.org/10.1016/j.jece.2024.112525.

[71] T.T. Nguyen, K. Edalati, Brookite TiO2 as an active photocatalyst for photoconversion of plastic wastes to acetic acid and simultaneous hydrogen production: Comparison with anatase and rutile, Chemosphere. 355 (2024) 141785. https://doi.org/10.1016/j.chemosphere.2024.141785.

[72] P. Ebrahimbabaie, K. Yousefi, J. Pichtel, Photocatalytic and biological technologies for elimination of microplastics in water: Current status, Sci. Total Environ. 806 (2022). https://doi.org/10.1016/j.scitotenv.2021.150603.

[73] B. Shojaei, M. Abtahi, M. Najafi, Chemical recycling of PET: A stepping-stone toward sustainability, Polym. Adv. Technol. 31 (2020) 2912–2938. https://doi.org/10.1002/pat.5023.

[74] A. Bifulco, J. Chen, A. Sekar, W.W. Klingler, A. Gooneie, S. Gaan, Recycling of flame retardant polymers: Current technologies and future perspectives, J. Mater. Sci. Technol. 199 (2024) 156–183. https://doi.org/10.1016/j.jmst.2024.02.039.

[75] Z. Jia, L. Gao, L. Qin, J. Yin, Chemical recycling of PET to value-added products, RSC Sustain. 1 (2023) 2135–2147. https://doi.org/10.1039/d3su00311f.

[76] S. Conroy, X. Zhang, Theoretical insights into chemical recycling of polyethylene terephthalate (PET), Polym. Degrad. Stab. 223 (2024) 110729. https://doi.org/10.1016/j.polymdegradstab.2024.110729.

[77] Humus Chemistry: Genesis, Composition, Reactions, Second Edition (Stevenson, F. J.), J. Chem. Educ. 72 (1995). https://doi.org/10.1021/ed072pa93.6.

[78] P. MacCarthy, The principles of humic substances: An introduction to the first principle, in: Humic Subst., 2007. https://doi.org/10.1039/9781847551085-00019.

[79] S. Vaz, L. Gebler, Management of Agrochemical Residues in the Environment, 2019. https://doi.org/10.1007/978-3-030-17891-8_12.

[80] P. Amato, M. Muscetta, V. Venezia, M. Cocca, G. Gentile, R. Castaldo, R. Marotta, G. Vitiello, Eco-sustainable design of humic acids-doped ZnO nanoparticles for UVA/light photocatalytic degradation of LLDPE and PLA plastics, J. Environ. Chem. Eng. 11 (2023) 109003. https://doi.org/10.1016/j.jece.2022.109003.

[81] S. Russo, M. Muscetta, P. Amato, V. Venezia, M. Verrillo, R. Rega, S. Lettieri, M. Cocca, R. Marotta, G. Vitiello, Humic substance/metal-oxide multifunctional nanoparticles as advanced antibacterial-antimycotic agents and photocatalysts for the degradation of PLA microplastics under UVA/solar radiation, Chemosphere. 346 (2024) 140605. https://doi.org/10.1016/j.chemosphere.2023.140605.

[82] M. Cocca, L. D'Orazio, Novel silver/polyurethane nanocomposite by In Situ reduction: Effects of the silver nanoparticles on phase and viscoelastic behavior, J. Polym. Sci. Part B Polym. Phys. 46 (2008) 344–350. https://doi.org/10.1002/polb.21308.

[83] V. Venezia, P.R. Avallone, G. Vitiello, B. Silvestri, N. Grizzuti, R. Pasquino, G. Luciani, Adding Humic Acids to Gelatin Hydrogels: A Way to Tune Gelation, Biomacromolecules. 23 (2022) 443–453. https://doi.org/10.1021/acs.biomac.1c01398.

[84] P.J.P. Espitia, N. de F.F. Soares, J.S. dos R. Coimbra, N.J. de Andrade, R.S. Cruz, E.A.A. Medeiros, Zinc Oxide Nanoparticles: Synthesis, Antimicrobial Activity and Food Packaging Applications, Food Bioprocess Technol. 5 (2012) 1447–1464. https://doi.org/10.1007/s11947-012-0797-6.

[85] J.N. Hasnidawani, H.N. Azlina, H. Norita, N.N. Bonnia, S. Ratim, E.S. Ali, Synthesis of ZnO Nanostructures Using Sol-Gel Method, Procedia Chem. 19 (2016) 211–216. https://doi.org/10.1016/j.proche.2016.03.095.

[86] G. Vitiello, V. Venezia, M. Verrillo, A. Nuzzo, J. Houston, S. Cimino, G. D'Errico, A. Aronne, L. Paduano, A. Piccolo, G. Luciani, Hybrid humic acid/titanium dioxide nanomaterials as highly effective antimicrobial agents against gram(−) pathogens and antibiotic contaminants in wastewater, Environ. Res. 193 (2021) 110562. https://doi.org/10.1016/j.envres.2020.110562.

[87] P. Jakes, E. Erdem, Finite size effects in ZnO nanoparticles: An electron paramagnetic resonance (EPR) analysis, Phys. Status Solidi - Rapid Res. Lett. 5 (2011) 56–58. https://doi.org/10.1002/pssr.201004450.

[88] E. Erdem, Microwave power, temperature, atmospheric and light dependence of intrinsic defects in ZnO nanoparticles: A study of electron paramagnetic resonance (EPR) spectroscopy, J. Alloys Compd. 605 (2014) 34–44. https://doi.org/10.1016/j.jallcom.2014.03.157.

[89] V. Venezia, G. Pota, B. Silvestri, G. Vitiello, P. Di Donato, G. Landi, V. Mollo, M. Verrillo, S. Cangemi, A. Piccolo, G. Luciani, A study on structural evolution of hybrid humic Acids-SiO2 nanostructures in pure water: Effects on physico-chemical and functional properties, Chemosphere. 287 (2022). https://doi.org/10.1016/j.chemosphere.2021.131985.

[90] L. Panzella, G. D'Errico, G. Vitiello, M. Perfetti, M.L. Alfieri, A. Napolitano, M. D'Ischia, Disentangling structure-dependent antioxidant mechanisms in phenolic polymers by multiparametric EPR analysis, Chem. Commun. 54 (2018) 9426–9429. https://doi.org/10.1039/c8cc05989f.

[91] G. Pota, A. Zanfardino, M. Di Napoli, D. Cavasso, M. Varcamonti, G. D'Errico, A. Pezzella, G. Luciani, G. Vitiello, Bioinspired antibacterial PVA/Melanin-TiO2 hybrid nanoparticles: the role of poly-vinyl-alcohol on their self-assembly and biocide activity, Colloids Surfaces B Biointerfaces. 202 (2021). https://doi.org/10.1016/j.colsurfb.2021.111671.

[92] G. Pota, V. Venezia, G. Vitiello, P. Di Donato, V. Mollo, A. Costantini, J. Avossa, A. Nuzzo, A. Piccolo, B. Silvestri, G. Luciani, Tuning functional behavior of humic acids through interactions with stöber silica nanoparticles, Polymers (Basel). 12 (2020). https://doi.org/10.3390/polym12040982.

[93] M.K. Debanath, S. Karmakar, Study of blueshift of optical band gap in zinc oxide (ZnO) nanoparticles prepared by low-temperature wet chemical method, Mater. Lett. 111 (2013) 116–119. https://doi.org/10.1016/j.matlet.2013.08.069.

[94] S. Abbasi, Photocatalytic activity study of coated anatase-rutile titania nanoparticles with nanocrystalline tin dioxide based on the statistical analysis, Environ. Monit. Assess. 191 (2019). https://doi.org/10.1007/s10661-019-7352-0.

[95] K. Yang, B. Xing, Adsorption of fulvic acid by carbon nanotubes from water, Environ. Pollut. 157 (2009) 1095–1100. https://doi.org/10.1016/j.envpol.2008.11.007.

[96] K. Yang, B. Xing, Sorption of phenanthrene by humic acid-coated nanosized TiO 2 and ZnO, Environ. Sci. Technol. 43 (2009) 1845–1851. https://doi.org/10.1021/es802880m.

[97] K.M. Reddy, S. V. Manorama, A.R. Reddy, Bandgap studies on anatase titanium dioxide nanoparticles, Mater. Chem. Phys. 78 (2003) 239–245. https://doi.org/10.1016/S0254-0584(02)00343-7.

[98] E.G. Goh, X. Xu, P.G. McCormick, Effect of particle size on the UV absorbance of zinc oxide nanoparticles, Scr. Mater. 78–79 (2014) 49–52. https://doi.org/10.1016/j.scriptamat.2014.01.033.

[99] V. Venezia, M. Verrillo, N. Gallucci, R. Di Girolamo, G. Luciani, G. D'Errico, L. Paduano, A. Piccolo, G. Vitiello, Exploiting bioderived humic acids: A molecular combination with ZnO nanoparticles leads to nanostructured hybrid interfaces with enhanced pro-oxidant and antibacterial activity, J. Environ. Chem. Eng. 11 (2023) 108973. https://doi.org/10.1016/j.jece.2022.108973.

[100] R. Del Vecchio, N. V. Blough, On the origin of the optical properties of humic substances, Environ. Sci. Technol. 38 (2004) 3885–3891. https://doi.org/10.1021/es049912h.

[101] S. Ma, M.E. Reish, Z. Zhang, I. Harrison, J.T. Yates, Anatase-Selective Photoluminescence Spectroscopy of P25 TiO2 Nanoparticles: Different Effects of Oxygen Adsorption on the Band Bending of Anatase, J. Phys. Chem. C. 121 (2017)

1263–1271. https://doi.org/10.1021/acs.jpcc.6b11714.

[102] C.C. Mercado, F.J. Knorr, J.L. McHale, S.M. Usmani, A.S. Ichimura, L. V. Saraf, Location of hole and electron traps on nanocrystalline anatase TiO 2, J. Phys. Chem. C. 116 (2012) 10796–10804. https://doi.org/10.1021/jp301680d.

[103] S. Lettieri, M. Pavone, TiO2-Based Nanostructures, Composites and Hybrid Photocatalysts, Materials (Basel). 15 (2022) 1–6. https://doi.org/10.3390/ma15041271.

[104] F.J. Knorr, J.L. McHale, Spectroelectrochemical photoluminescence of trap states of nanocrystalline TiO2 in aqueous media, J. Phys. Chem. C. 117 (2013) 13654–13662. https://doi.org/10.1021/jp402264p.

[105] D.K. Pallotti, L. Passoni, P. Maddalena, F. Di Fonzo, S. Lettieri, Photoluminescence Mechanisms in Anatase and Rutile TiO2, J. Phys. Chem. C. 121 (2017) 9011–9021. https://doi.org/10.1021/acs.jpcc.7b00321.

[106] S. Malato, J. Blanco, C. Richter, P. Fernández, M.I. Maldonado, Solar photocatalytic mineralization of commercial pesticides: oxamyl, Sol. Energy Mater. Sol. Cells. 64 (2000) 1–14. https://doi.org/10.1016/S0927-0248(00)00037-4.

[107] D. Spasiano, R. Marotta, S. Malato, P. Fernandez-Ibañez, I. Di Somma, Solar photocatalysis: Materials, reactors, some commercial, and pre-industrialized applications. A comprehensive approach, Appl. Catal. B Environ. 170–171 (2015) 90–123. https://doi.org/10.1016/j.apcatb.2014.12.050.

[108] A. Podstawczyńska, UV and global solar radiation in Łódź, Central Poland, Int. J. Climatol. 30 (2010) 1–10. https://doi.org/10.1002/joc.1864.

[109] W.L.W. Lee, C.S. Lu, H.P. Lin, J.Y. Chen, C.C. Chen, Photocatalytic degradation of ethyl violet dye mediated by TiO2 under an anaerobic condition, J. Taiwan Inst. Chem. Eng. 45 (2014) 2469–2479. https://doi.org/10.1016/j.jtice.2014.04.025.

[110] Y.C. Hsu, M.P. Weir, R.W. Truss, C.J. Garvey, T.M. Nicholson, P.J. Halley, A fundamental study on photo-oxidative degradation of linear low density polyethylene films at embrittlement, Polymer (Guildf). 53 (2012) 2385–2393.

https://doi.org/10.1016/j.polymer.2012.03.044.

[111] S. Baskaran, M. Sathiavelu, Application of Attenuated Total Reflection - Fourier Transform Infrared spectroscopy to characterize the degradation of littered multilayer food packaging plastics, Vib. Spectrosc. 109 (2020). https://doi.org/10.1016/j.vibspec.2020.103105.

[112] R. Xie, B. Qu, Thermo-oxidative degradation behaviors of expandable graphite-based intumescent halogen-free flame retardant LLDPE blends, Polym. Degrad. Stab. . 71 (2001) 395–402. www.elsevier.nl/locate/polydegstab.

[113] S.M. Al-Salem, M.H. Behbehani, A. Al-Hazza'a, J.C. Arnold, S.M. Alston, A.A. Al-Rowaih, F. Asiri, S.F. Al-Rowaih, H. Karam, Study of the degradation profile for virgin linear low-density polyethylene (LLDPE) and polyolefin (PO) plastic waste blends, J. Mater. Cycles Waste Manag. 21 (2019) 1106–1122. https://doi.org/10.1007/s10163-019-00868-8.

[114] D. Rasselet, A. Ruellan, A. Guinault, G. Miquelard-Garnier, C. Sollogoub, B. Fayolle, Oxidative degradation of polylactide (PLA) and its effects on physical and mechanical properties, Eur. Polym. J. 50 (2014) 109–116. https://doi.org/10.1016/j.eurpolymj.2013.10.011.

[115] B. Riinby, PHOTODEGRADATION AND PHOTO-OXIDATION OF SYNTHETIC POLYMERS, 1989.

[116] L. Guadagno, C. Naddeo, V. Vittoria, G. Camino, C. Cagnani, Chemical and morphologial modifications of irradiated linear low density polyethylene (LLDPE), Polym. Degrad. Stab. . 72 (2001) 175–186. www.elsevier.nl/locate/polydegstab.

[117] T. Ojeda, A. Freitas, K. Birck, E. Dalmolin, R. Jacques, F. Bento, F. Camargo, Degradability of linear polyolefins under natural weathering, Polym. Degrad. Stab. 96 (2011) 703–707. https://doi.org/10.1016/j.polymdegradstab.2010.12.004.

[118] C. Goedecke, D. Dittmann, P. Eisentraut, Y. Wiesner, B. Schartel, P. Klack, U. Braun, Evaluation of thermoanalytical methods equipped with evolved gas analysis for the detection of microplastic in environmental samples, J. Anal. Appl.

Pyrolysis. 152 (2020). https://doi.org/10.1016/j.jaap.2020.104961.

[119] M. Mucha, S. Bialas, H. Kaczmarek, Effect of nanosilver on the photodegradation of poly(lactic acid), J. Appl. Polym. Sci. 131 (2014). https://doi.org/10.1002/app.40144.

[120] J.E. Martín-Alfonso, J. Urbano, A.A. Cuadri, J.M. Franco, The combined effect of H2O2 and light emitting diodes (LED) process assisted by TiO2 on the photooxidation behaviour of PLA, Polym. Test. 73 (2019) 268–275. https://doi.org/10.1016/j.polymertesting.2018.11.031.

[121] W.A. Herrera-Kao, M.I. Loría-Bastarrachea, Y. Pérez-Padilla, J. V. Cauich-Rodríguez, H. Vázquez-Torres, J.M. Cervantes-Uc, Thermal degradation of poly(caprolactone), poly(lactic acid), and poly(hydroxybutyrate) studied by TGA/FTIR and other analytical techniques, Polym. Bull. 75 (2018) 4191–4205. https://doi.org/10.1007/s00289-017-2260-3.

[122] A. Antunes, A. Popelka, O. Aljarod, M.K. Hassan, A.S. Luyt, Effects of rutile-TiO2 nanoparticles on accelerated weathering degradation of poly(Lactic Acid), Polymers (Basel). 12 (2020). https://doi.org/10.3390/POLYM12051096.

[123] R. Patwa, A. Kumar, V. Katiyar, Crystallization kinetics, morphology, and hydrolytic degradation of novel bio-based poly(lactic acid)/crystalline silk nano-discs nanobiocomposites, J. Appl. Polym. Sci. 135 (2018). https://doi.org/10.1002/app.46590.

[124] J. Almond, P. Sugumaar, M.N. Wenzel, G. Hill, C. Wallis, Determination of the carbonyl index of polyethylene and polypropylene using specified area under band methodology with ATR-FTIR spectroscopy, E-Polymers. 20 (2020) 369–381. https://doi.org/10.1515/epoly-2020-0041.

[125] L. Santonja-Blasco, A. Ribes-Greus, R.G. Alamo, Comparative thermal, biological and photodegradation kinetics of polylactide and effect on crystallization rates, Polym. Degrad. Stab. 98 (2013) 771–784. https://doi.org/10.1016/j.polymdegradstab.2012.12.012.

[126] M. Cocca, M.L. Di Lorenzo, M. Malinconico, V. Frezza, Influence of crystal

polymorphism on mechanical and barrier properties of poly(l-lactic acid), Eur. Polym. J. 47 (2011) 1073–1080. https://doi.org/10.1016/j.eurpolymj.2011.02.009.

[127] I. Ritacco, C. Imparato, L. Falivene, L. Cavallo, A. Magistrato, L. Caporaso, M. Farnesi Camellone, A. Aronne, Spontaneous Production of Ultrastable Reactive Oxygen Species on Titanium Oxide Surfaces Modified with Organic Ligands, Adv. Mater. Interfaces. 8 (2021). https://doi.org/10.1002/admi.202100629.

[128] C. Imparato, G. D'Errico, W. Macyk, M. Kobielusz, G. Vitiello, A. Aronne, Interfacial Charge Transfer Complexes in TiO2-Enediol Hybrids Synthesized by Sol-Gel, Langmuir. 38 (2022) 1821–1832. https://doi.org/10.1021/acs.langmuir.1c02939.

[129] A.B. Muñoz-García, F. Sannino, G. Vitiello, D. Pirozzi, L. Minieri, A. Aronne, P. Pernice, M. Pavone, G. D'Errico, Origin and Electronic Features of Reactive Oxygen Species at Hybrid Zirconia-Acetylacetonate Interfaces, ACS Appl. Mater. Interfaces. 7 (2015) 21662–21667. https://doi.org/10.1021/acsami.5b06988.

[130] P. Amato, M. Fantauzzi, F. Sannino, I. Ritacco, G. Santoriello, M. Farnesi Camellone, C. Imparato, A. Bifulco, G. Vitiello, L. Caporaso, A. Rossi, A. Aronne, Indirect daylight oxidative degradation of polyethylene microplastics by a bio-waste modified TiO2-based material, J. Hazard. Mater. 463 (2024) 132907. https://doi.org/10.1016/j.jhazmat.2023.132907.

[131] C.M. Lee, S. Lim, G.Y. Kim, D. Kim, D.W. Kim, H.C. Lee, K.Y. Lee, Rosin microparticles as drug carriers: Influence of various solvents on the formation of particles and sustained-release of indomethacin, Biotechnol. Bioprocess Eng. 9 (2004) 476–481. https://doi.org/10.1007/BF02933489.

[132] D. Atzei, M. Fantauzzi, A. Rossi, P. Fermo, A. Piazzalunga, G. Valli, R. Vecchi, Surface chemical characterization of PM 10 samples by XPS, Appl. Surf. Sci. 307 (2014) 120–128. https://doi.org/10.1016/j.apsusc.2014.03.178.

[133] G. Beamson, D. Briggs, High Resolution XPS of Organic Polymers: The Scienta ESCA300 Database, J. Chem. Educ. 70 (1993) A25. https://doi.org/10.1021/ed070pA25.5.

[134] V. Beltran, N. Salvadó, S. Butí, T. Pradell, Ageing of resin from Pinus species assessed by infrared spectroscopy, Anal. Bioanal. Chem. 408 (2016) 4073–4082. https://doi.org/10.1007/s00216-016-9496-x.

[135] F. Ren, Y.F. Zheng, X.M. Liu, X.Y. Yue, L. Ma, W.G. Li, F. Lai, J.L. Liu, W.L. Guan, An investigation of the oxidation mechanism of abietic acid using two-dimensional infrared correlation spectroscopy, J. Mol. Struct. 1084 (2015) 236–243. https://doi.org/10.1016/j.molstruc.2014.12.055.

[136] S. Zumbühl, A. Brändle, A. Hochuli, N.C. Scherrer, W. Caseri, Derivatization Technique to Identify Specifically Carbonyl Groups by Infrared Spectroscopy: Characterization of Photooxidative Aging Products in Terpenes and Terpeneous Resins, Anal. Chem. 89 (2017) 1742–1748. https://doi.org/10.1021/acs.analchem.6b04008.

[137] Y. He, O. Dulub, H. Cheng, A. Selloni, U. Diebold, Evidence for the predominance of subsurface defects on reduced anatase TiO2(101), Phys. Rev. Lett. 102 (2009) 1–4. https://doi.org/10.1103/PhysRevLett.102.106105.

[138] W. Navarra, I. Ritacco, O. Sacco, L. Caporaso, M. Farnesi Camellone, V. Venditto, V. Vaiano, Density Functional Theory Study and Photocatalytic Activity of ZnO/N-Doped TiO2Heterojunctions, J. Phys. Chem. C. 126 (2022) 7000–7011. https://doi.org/10.1021/acs.jpcc.2c00152.

[139] A. Aronne, M. Fantauzzi, C. Imparato, D. Atzei, L. De Stefano, G. D'Errico, F. Sannino, I. Rea, D. Pirozzi, B. Elsener, P. Pernice, A. Rossi, Electronic properties of TiO2-based materials characterized by high Ti3+ self-doping and low recombination rate of electron-hole pairs, RSC Adv. 7 (2017) 2373–2381. https://doi.org/10.1039/c6ra27111a.

[140] H. Tang, H. Berger, P.E. Schmid, F. Lévy, G. Burri, Photoluminescence in TiO2 anatase single crystals, Solid State Commun. 87 (1993) 847–850. https://doi.org/10.1016/0038-1098(93)90427-O.

[141] A. Aronne, F. Sannino, S.R. Bonavolontà, E. Fanelli, A. Mingione, P. Pernice, R. Spaccini, D. Pirozzi, Use of a new hybrid sol-gel zirconia matrix in the removal of

the herbicide MCPA: A sorption/degradation process, Environ. Sci. Technol. 46 (2012) 1755–1763. https://doi.org/10.1021/es203223s.

[142] P. Makuła, M. Pacia, W. Macyk, How To Correctly Determine the Band Gap Energy of Modified Semiconductor Photocatalysts Based on UV-Vis Spectra, J. Phys. Chem. Lett. 9 (2018) 6814–6817. https://doi.org/10.1021/acs.jpclett.8b02892.

[143] T. Berger, M. Sterrer, O. Diwald, E. Knözinger, D. Panayotov, T.L. Thompson, J.T. Yates, Light-induced charge separation in anatase TiO 2 particles, J. Phys. Chem. B. 109 (2005) 6061–6068. https://doi.org/10.1021/jp0404293.

[144] J. Passaro, C. Imparato, D. Parida, A. Bifulco, F. Branda, A. Aronne, Electrospinning of PVP-based ternary composites containing SiO2 nanoparticles and hybrid TiO2 microparticles with adsorbed superoxide radicals, Compos. Part B Eng. 238 (2022) 109874. https://doi.org/https://doi.org/10.1016/j.compositesb.2022.109874.

[145] G. Vitiello, A. Zanfardino, O. Tammaro, M. Di Napoli, M.F. Caso, A. Pezzella, M. Varcamonti, B. Silvestri, G. D'Errico, A. Costantini, G. Luciani, Bioinspired hybrid eumelanin-TiO2 antimicrobial nanostructures: the key role of organo-inorganic frameworks in tuning eumelanin's biocide action mechanism through membrane interaction, RSC Adv. 8 (2018) 28275–28283. https://doi.org/10.1039/c8ra04315a.

[146] Y. Nosaka, A.Y. Nosaka, Generation and Detection of Reactive Oxygen Species in Photocatalysis, Chem. Rev. 117 (2017) 11302–11336. https://doi.org/10.1021/acs.chemrev.7b00161.

[147] M. Hayyan, M.A. Hashim, I.M. Alnashef, Superoxide Ion: Generation and Chemical Implications, Chem. Rev. 116 (2016) 3029–3085. https://doi.org/10.1021/acs.chemrev.5b00407.

[148] H. De Frond, L. Thornton Hampton, S. Kotar, K. Gesulga, C. Matuch, W. Lao, S.B. Weisberg, C.S. Wong, C.M. Rochman, Monitoring microplastics in drinking water: An interlaboratory study to inform effective methods for quantifying and

characterizing microplastics, Chemosphere. 298 (2022) 134282. https://doi.org/10.1016/j.chemosphere.2022.134282.

[149] J. Kang, L. Zhou, X. Duan, H. Sun, Z. Ao, S. Wang, Degradation of Cosmetic Microplastics via Functionalized Carbon Nanosprings, Matter. 1 (2019) 745–758. https://doi.org/10.1016/j.matt.2019.06.004.

[150] K.N. Fotopoulou, H.K. Karapanagioti, Degradation of Various Plastics in the Environment, Handb. Environ. Chem. 78 (2019) 71–92. https://doi.org/10.1007/698_2017_11.

[151] B. Gewert, M.M. Plassmann, M. Macleod, Pathways for degradation of plastic polymers floating in the marine environment, Environ. Sci. Process. Impacts. 17 (2015) 1513–1521. https://doi.org/10.1039/c5em00207a.

[152] B.E. Llorente-García, J.M. Hernández-López, A.A. Zaldívar-Cadena, C. Siligardi, E.I. Cedillo-González, First insights into photocatalytic degradation of HDPE and LDPE microplastics by a mesoporous N-TiO2 coating: Effect of size and shape of microplastics, Coatings. 10 (2020). https://doi.org/10.3390/coatings10070658.

[153] P. Xvi, P. Ii, P. Laboratorium, T H E Crystal Counter, 42 (1950) 517–527.

[154] V.G. Nguyen, H. Thai, D.H. Mai, H.T. Tran, D.L. Tran, M.T. Vu, Effect of titanium dioxide on the properties of polyethylene/TiO 2 nanocomposites, Compos. Part B Eng. 45 (2013) 1192–1198. https://doi.org/10.1016/j.compositesb.2012.09.058.

[155] S.S. Ali, I.A. Qazi, M. Arshad, Z. Khan, T.C. Voice, C.T. Mehmood, Photocatalytic degradation of low density polyethylene (LDPE) films using titania nanotubes, Environ. Nanotechnology, Monit. Manag. 5 (2016) 44–53. https://doi.org/10.1016/j.enmm.2016.01.001.

[156] P. Kaewkam, A. Kanchanapaetnukul, J. Khamyan, N. Phadmanee, K.Y.A. Lin, K. Kobwittaya, S. Sirivithayapakorn, UV-assisted TiO2photocatalytic degradation of virgin LDPE films: Effect of UV-A, UV-C, and TiO2, J. Environ. Chem. Eng. 10 (2022). https://doi.org/10.1016/j.jece.2022.108131.

[157] H. Hunke, N. Soin, T.H. Shah, E. Kramer, A. Pascual, M.S.L. Karuna, E. Siores,

Low-pressure H2, NH3 microwave plasma treatment of Polytetrafluoroethylene (PTFE) powders: Chemical, thermal and wettability analysis, Materials (Basel). 8 (2015) 2258–2275. https://doi.org/10.3390/ma8052258.

[158] Y. Wang, J. Zhang, L. Pu, M. Cao, S. Dong, C.D. Vecitis, G. Gao, Unexpected exfoliation and activity of nano poly(tetrafluoroethylene) particles from magnetic stir bars: Discovery and implication, Chemosphere. 291 (2022) 132797. https://doi.org/10.1016/j.chemosphere.2021.132797.

[159] G.J. Puts, P. Crouse, B.M. Ameduri, Polytetrafluoroethylene: Synthesis and Characterization of the Original Extreme Polymer, Chem. Rev. 119 (2019) 1763–1805. https://doi.org/10.1021/acs.chemrev.8b00458.

[160] P. Amato, M. Fantauzzi, A. Bifulco, C. Imparato, A. Rossi, A. Aronne, F. Sannino, Physical and chemical degradation of PTFE magnetic stir bars induced by TiO2-based materials, Appl. Surf. Sci. 676 (2024) 161018. https://doi.org/10.1016/j.apsusc.2024.161018.

[161] K. Yamauchi, Y. Yao, T. Ochiai, M. Sakai, Y. Kubota, G. Yamauchi, Antibacterial activity of hydrophobic composite materials containing a visible-light-sensitive photocatalyst, J. Nanotechnol. 2011 (2011). https://doi.org/10.1155/2011/380979.

[162] J. Si, R. Ma, Y. Wu, Y. Dong, K. Yao, Microstructure and magnetic properties of novel powder cores composed of iron-based amorphous alloy and PTFE, J. Mater. Sci. 57 (2022) 8154–8166. https://doi.org/10.1007/s10853-022-07199-4.

[163] L. Meng, B. Song, Y. Lu, K. Lv, W. Gao, Y. Wang, G. Jiang, The occurrence of per- and polyfluoroalkyl substances (PFASs) in fluoropolymer raw materials and products made in China, J. Environ. Sci. (China). 107 (2021) 77–86. https://doi.org/10.1016/j.jes.2021.01.027.

[164] J. Zhang, R. Pei, J. Tan, Z. Ni, S. Ye, Y. Luo, Visualizing Water Monomers and Chiral OH-(H2O) Complexes Infiltrated in a Macroscopic Hydrophobic Teflon Matrix, J. Am. Chem. Soc. 145 (2023) 26925–26931. https://doi.org/10.1021/jacs.3c09950.

[165] E.O. Pentsak, D.B. Eremin, E.G. Gordeev, V.P. Ananikov, Phantom Reactivity in

Organic and Catalytic Reactions as a Consequence of Microscale Destruction and Contamination-Trapping Effects of Magnetic Stir Bars, ACS Catal. 9 (2019) 3070–3081. https://doi.org/10.1021/acscatal.9b00294.

[166] C. Imparato, M.M. Bonifazzi, G. D'Errico, A. Bifulco, O. Tammaro, S. Esposito, A. Aronne, D. Pirozzi, Dark and sunlight-driven dye degradation over a TiO2–dibenzoylmethane hybrid xerogel, Colloids Surfaces A Physicochem. Eng. Asp. 684 (2024). https://doi.org/10.1016/j.colsurfa.2024.133148.

[167] C. Mao, H. Lei, Z. Guo, X. Jia, X. Cui, J. Huang, L. Fei, Y. Jia, W. Chen, Exceptional tribo-catalytic degradation of concentrated methyl orange and methylene blue solutions by DXN-RT30 TiO2 nanoparticles, Ceram. Int. 50 (2024) 4737–4745. https://doi.org/10.1016/j.ceramint.2023.11.218.

[168] X. Cui, P. Li, H. Lei, C. Tu, D. Wang, Z. Wang, W. Chen, Greatly enhanced tribocatalytic degradation of organic pollutants by TiO2 nanoparticles through efficiently harvesting mechanical energy, Sep. Purif. Technol. 289 (2022) 120814. https://doi.org/10.1016/j.seppur.2022.120814.

[169] Y. Wang, J. Zhang, L. Pu, M. Cao, S. Dong, C.D. Vecitis, G. Gao, Unexpected exfoliation and activity of nano poly(tetrafluoroethylene) particles from magnetic stir bars: Discovery and implication, Chemosphere. 291 (2022) 132797. https://doi.org/10.1016/j.chemosphere.2021.132797.

[170] Y. Wang, S. Shen, M. Liu, G. He, X. Li, Enhanced tribocatalytic degradation performance of organic pollutants by Cu1.8S/CuCo2S4 p-n junction, J. Colloid Interface Sci. 655 (2024) 187–198. https://doi.org/10.1016/j.jcis.2023.10.164.

[171] H. Zou, Y. Zhang, L. Guo, P. Wang, X. He, G. Dai, H. Zheng, C. Chen, A.C. Wang, C. Xu, Z.L. Wang, Quantifying the triboelectric series, Nat. Commun. 10 (2019) 1–9. https://doi.org/10.1038/s41467-019-09461-x.

[172] N. Fairley, V. Fernandez, M. Richard-Plouet, C. Guillot-Deudon, J. Walton, E. Smith, D. Flahaut, M. Greiner, M. Biesinger, S. Tougaard, D. Morgan, J. Baltrusaitis, Systematic and collaborative approach to problem solving using X-ray photoelectron spectroscopy, Appl. Surf. Sci. Adv. 5 (2021) 100112.

https://doi.org/10.1016/j.apsadv.2021.100112.

[173] J. Matthew, Surface analysis by Auger and x-ray photoelectron spectroscopy. D. Briggs and J. T. Grant (eds). IMPublications, Chichester, UK and SurfaceSpectra, Manchester, UK, 2003. 900 pp., ISBN 1-901019-04-7, 900 pp, Surf. Interface Anal. 36 (2004). https://doi.org/10.1002/sia.2005.

[174] Y.C. Hsu, M.P. Weir, R.W. Truss, C.J. Garvey, T.M. Nicholson, P.J. Halley, A fundamental study on photo-oxidative degradation of linear low density polyethylene films at embrittlement, Polymer (Guildf). 53 (2012) 2385–2393. https://doi.org/10.1016/j.polymer.2012.03.044.

[175] E.W. Fischer, H.J. Sterzel, G. Wegner, Investigation of the structure of solution grown crystals of lactide copolymers by means of chemical reactions, 1973.

[176] B. Wunderlich, G. Czornyj, A Study of Equilibrium Melting of Polyethylene, Macromolecules. 10 (1977) 906–913. https://doi.org/10.1021/ma60059a006.

List of Publications

P. Amato, M. Muscetta, V. Venezia, M. Cocca, G. Gentile, R. Castaldo, R. Marotta, G. Vitiello, Eco-sustainable design of humic acids-doped ZnO nanoparticles for UVA/light photocatalytic degradation of LLDPE and PLA plastics, Journal of Environmental Chemical Engineering 11 (2023) 109003. https://doi.org/10.1016/j.jece.2022.109003

J. Zhang, A. Bifulco, **P. Amato**, C. Imparato, K. Qi, Copper indium sulfide quantum dots in photocatalysis, Journal of Colloid and Interface Science 638 (2023) 193–219. https://doi.org/10.1016/j.jcis.2023.01.107

S. Russo, M. Muscetta, **P. Amato**, V. Venezia, M. Verrillo, R. Rega, S. Lettieri, M. Cocca, R. Marotta, G. Vitiello, Humic substance/metal-oxide multifunctional nanoparticles as advanced antibacterial-antimycotic agents and photocatalysts for the degradation of PLA microplastics under UVA/solar radiation, Chemosphere 346 (2024) 140605. https://doi.org/10.1016/j.chemosphere.2023.140605

P. Amato, M. Fantauzzi, F. Sannino, I. Ritacco, G. Santoriello, M. Camellone, C. Imparato, A. Bifulco, G. Vitiello, L. Caporaso, A. Rossi, A. Aronne., Indirect daylight oxidative degradation of polyethylene microplastics by a bio-waste modified TiO2-based material, Journal of Hazardous Materials 463 (2024) 132907. https://doi.org/10.1016/j.jhazmat.2023.132907

P. Amato, M. Fantauzzi, A. Bifulco, C. Imparato, A. Rossi, A. Aronne, F. Sannino., Physical and chemical degradation of PTFE magnetic stir bars induced by TiO2-based materials, Applied Surface Science 676 (2024) 161018. https://doi.org/10.1016/j.apsusc.2024.161018